

MODELING THE FLOW OF PCL FLUID DUE TO THE MOVEMENT OF LUNG
CILIA

by

Kannanut Chamsri

BS., Mathematics, Chulalongkorn University, Thailand, 2002

M.S., Applied Mathematics, Chulalongkorn University, Thailand, 2005

A thesis submitted to the
Faculty of the Graduate School of the
University of Colorado Denver in partial fulfillment
of the requirements for the degree of
Doctor of Philosophy
Applied Mathematics
2012

©2012 by Kannanut Chamsri

All rights reserved

This thesis for the Doctor of Philosophy degree by
Kannanut Chamsri
has been approved for the
Applied Mathematics
by

Jan Mandel, Chair
Lynn S. Bennethum, Advisor
Julien Laugou
Long Lee
Russell P. Bowler

Date _____

Chamsri, Kannanut (Ph.D., Applied Mathematics)

Modeling the Flow of PCL Fluid due to the Movement of Lung Cilia

Thesis directed by Associate Professor Lynn S. Bennethum

ABSTRACT

Cilia in the human lungs are moving hairs that aid in the movement of mucus. The layer that contains the cilia is called the periciliary layer, PCL, and the liquid in that layer the PCL fluid. We consider the PCL fluid as an incompressible viscous fluid, and we consider the cilia as a periodic array of cylinders that rotate about their base with height varying as a function of the angle. We seek a three-dimensional mathematical model of the PCL fluid slowly flowing due to the movement of the cilia. We use homogenization to determine a system of equations that are then solved numerically to calculate the permeability. If r is the radius of the cilia and d is the distance between two adjacent cilia, we determine the permeability as a function of r/d and the angle θ that the cylinders make with the bottom surface. Numerical results are obtained using the mixed finite element method of Taylor-Hood type. The numerical results for the permeability are validated by comparing the results with numerical results of Rodrigo P.A. Rocha and Manuel E. Cruz with good agreement, and when the flow aligns and is perpendicular to the array of cylinders, the results are validated with experimental data. For an initial model of the fluid flow in the PCL, we consider the overall height as a constant, the portion of the PCL with cilia as a porous medium, and the PCL fluid above the cilia as undergoing Stokes flow. To calculate the fluid velocity in the PCL layer, Stokes-Brinkman equations are applied with a fixed boundary height of the PCL layer. The numerical result is compared with an analytical solution when the top boundary fluid is moving at a constant velocity in order to validate the numerical solution. The existence and uniqueness of the numerical model is also presented.

The form and content of this abstract are approved. I recommend its publication.

Approved: Lynn S. Bennethum

DEDICATION

This thesis is dedicated to my beloved parents, Mr. Wipas and Mrs. Chanapa Chamsri, who have never failed to give me moral support, cared for all my needs as I developed my education, and taught me that even the largest task can be accomplished if it is done one step at a time.

ACKNOWLEDGMENT

I would like to thank everyone who have helped and inspired me during my doctoral study.

This thesis would not have been possible without the generous support of my advisor, Prof. Lynn S. Bennethum, for her rich patience in providing endless idea, discussions, motivation, enthusiasm and encouragement with her positive energy. Her guidance delights me in the time of research and writing this thesis.

In addition to my advisor, the support of Prof. Jan Mandel allowed me to access the forceful computing resources of the mathematical department, which provided me with computer supplies and immense knowledge. I am also indebted to Prof. Long Lee, a wonderful faculty of the University of Wyoming, for his outstanding efforts in ensuring that ground-works were kept at my fingertips. I would like to thank the rest of my thesis committee -Prof. Julien Langou and Prof. Russell P. Bowler -for their perceptive comments, and questions.

Another thank you to Dr. Bedrich Sousedik who showed great interest and support in my research and was an excellent consultant in making coding a lot easier. I appreciate his patience despite my numerous and unending questions, and his helpfulness throughout my academic years.

My special thanks also go to Prof. Howard L. Schreyer for introducing us to the Defense Advanced Research Projects Agency (DARPA) group which provides an exceptional opportunity to cooperate works with the professional team and for guiding us to work on the diverse exciting project. I would also like to thank Eric Sullivan for his helps and for the stimulating discussions we were working on together before deadlines.

I greatly appreciate and wish to thank the parents of Lynn Bateman, who donated the funds that supported my study during the Fall semester of 2011, giving me the opportunity to devote myself to conducting and strengthening my research independently and proficiently.

I would like to take this opportunity to thank Dr. Christopher Harder for providing guidance in regards to the stability of finite element schemes and his assistances.

Not forgetting to thanks also to the faculties, graduate students at the University of Colorado Denver, and friends for sharing the experiences and distracting from science.

Last but not the least, I truly thank my families and my parents for always being there for me with their support throughout my life.

TABLE OF CONTENTS

LIST OF FIGURES	x
LIST OF TABLES	xiii
CHAPTER	
1. INTRODUCTION	1
2. HOMOGENIZATION	8
3. PERMEABILITY	17
3.1 Relationship between Drag Coefficient and Permeability	18
3.2 Discretization of the Model Problem	20
3.3 Validation of Numerical Results	24
3.4 Numerical Permeability Functions	30
3.5 Comparison with Kozeny-Carman Equation	33
4. MODELING THE PCL	44
4.1 General Form of the Momentum Equations using HMT	46
4.2 The Continuity Equation	50
4.3 Darcy's Law	52
4.4 Derivation of the Brinkman equation	53
4.5 Derivation of Stokes Equation	56
4.6 Well-posedness Stokes-Brinkman	57
5. NUMERICAL RESULTS FOR THE FIXED HEIGHT MODEL, TWO-DIMENSIONAL MODEL	71
5.1 Boundary Conditions	72
5.2 Model Discretization	74
5.3 Validation of the Code and Numerical Results	79
6. FREE BOUNDARY TWO-DIMENSIONAL MODEL	86
6.1 Model Problem and Boundary Conditions	87
6.2 Numerical Implementation	88
	viii

7. CONCLUSION	92
APPENDICES	
A. NOMENCLATURE	95
B. BASIS FUNCTIONS	102
REFERENCES	106

LIST OF FIGURES

Figure

1.1	Cartoon picture of a patchwork of goblet and ciliated cells at the epithelium . . .	2
1.2	The PCL and mucous layers where $\Omega = H_c \times L_c$ is our computational domain with subdomains $\Omega_1 = L_c \times H_{c1}$ and $\Omega_2 = L_c \times H_{c2}$	4
1.3	Geometry: an ideal cell of cylinders when the angle between cylinders and horizontal plane is 90 degrees; the top view of the left figure ; the angle θ between the cylinder and the horizontal plane.	4
2.1	A reference heterogeneities Y are periodic of period ϵY and their size is order of ϵ	9
2.2	Upscaling procedure where $\epsilon > 0$ is a spatial parameter.	9
3.1	Permeability being close to zero of fluid flow through a cell array of cylinders when the boundary is almost not Lipschitz	26
3.2	Permeability of fluid flow through a cell array of cylinders with increasing r/d , $\theta = 90^\circ$. Then $r/d = 1.2077$ is touching.	27
3.3	Diagonal values of the permeability tensor as a function of angle θ for r/d fixed at $1/3$	27
3.4	Off-diagonal values of the permeability tensor k_{12} and k_{23} as a function of angle θ for r/d fixed at $1/3$	28
3.5	Off-diagonal values of the permeability tensor k_{13} as a function of angle θ for r/d fixed at $1/3$	28
3.6	Permeability of fluid flow through a periodic array of cylinders for $\theta = 0$. When the flow aligns parallel to the cylinders, figures show the experimental scalar permeabilities of Sullivan for hairs and goat wool, respectively, comparing with our numerical $2 * k_{33}$ and $2 * (k_{11} + k_{22})$ results for $\theta = \pi/2$	31
3.7	Permeability of fluid flow through a cell array of cylinders. Figures are comparing the experimental data of Brown and Chen with our numerical k_{33} and $k_{11} + k_{22}$ when the flow is perpendicular to the array of cylinders.	32

3.8	The top left graph is the numerically generated permeability component k_{11} while the top right one is the fourth-order polynomial approximation of the top left graph; the pointwise absolute error are shown at the bottom.	34
3.9	The diagonal components k_{22} and k_{33} of the permeability tensor	35
3.10	The off-diagonal components k_{12} , k_{13} and k_{23} of the permeability tensor.	36
3.11	Geometry: the left figure shows the cell array of cylinders when the angle between the cylinders and horizontal plane is 75 degrees; the right one shows each cell consists of 2 ellipsoidal cylinders.	40
3.12	Figure shows the radii of an ellipse in both major and minor axes and θ is the angle between the horizontal plane and the side of the cylinder while h_θ is the height of the periodic cell which is perpendicular to the horizontal plane.	41
3.13	The green line represents the the spherical part of the permeability tensor of the numerical result while the blue and red ones are from the functions (3.62) and (3.63), respectively, where x-axis is the porosity depending on each angle.	43
4.1	The cartoon picture is showing the fixed boundary while the cilia is moving forward and backward making the angle θ with the horizontal plane in the PCL.	44
5.1	The left figures shows the PCL when $t = t_0$ where the cilia is perpendicular to the horizontal plan while the right one displays the PCL when $t = t_1$ where the cilia make an angle θ to the horizontal plan, where θ is less than 90 degrees.	71
5.2	A two dimensional Cartesian coordinate system with axis lines x_1 and x_2 and the cartoon picture of the cilia in the PCL with boundary conditions.	74
5.3	Velocity profiles in the x_2 direction or y -axis of the exact solution and our numerical result where $u_0 = 1$; $\mu = 1$; $\epsilon^l = 0.64457$; $H_c = 1$ and $H_{c2} = 0.7071$	81
5.4	Velocity profiles of the numerical and exact solutions using our permeability results with the corresponding angle θ ; $u_0 = 1$; $\mu = 1$; $H_c = 1$	82
5.5	Convergence of the velocity profiles of the numerical results to the exact solutions when the angle θ is 45°	83

5.6	Velocity profile in the x_2 direction of the cilia making angles $\theta = 26, 30, \dots, 90^\circ$ with the horizontal plane when the shear stress is zero at the free-fluid/porous-medium interface.	85
6.1	The cartoon picture is showing the free boundary having a unknown curve s while the cilia is moving forward and backward making the angle θ with the horizontal plane in the PCL.	86
6.2	A two dimensional Cartesian coordinate system with axis lines x_1 and x_2 and the cartoon picture of the moving cilia creating a free boundary curve \mathbf{s} with boundary conditions.	88
B.1	Nodal numbering for the 27-variable-number-of-nodes element where the origin is at the center of the brick.	102
B.2	Nodal numbering for the 3-variable-number-of-nodes element	103
B.3	Nodal numbering for the 4-variable-number-of-nodes tetrahedron element. . . .	105
B.4	Nodal numbering for the 10-variable-number-of-nodes quadratic tetrahedron element.	105

LIST OF TABLES

Table

3.1	Permeability through the cell array of cylinders at 90 degree of the different heights and periodic REVs providing the same permeability.	26
3.2	Permeability through the simple cubic array of spheres with solid volume fraction $\epsilon^s = 0.216$ and radius = 0.5 unit; k_s denotes the permeabilities in this research; δk is the relative error of k_s with respect to k_{RM} which is the permeability calculating Rocha and Cruz (2009).	29
3.3	Permeability through the simple cubic array of spheres with varying volume fraction of solid ϵ^s with radius 0.5 unit; k_s and k_{RM} denote the permeabilities in this research and by Rocha and Cruz (2009), respectively; δk is the relative error of k_s with respect to k_{RM}	30
3.4	The fourth-order polynomial functions: $a_1x^4 + a_2x^3y + a_3x^3 + a_4x^2y^2 + a_5x^2y + a_6x^2 + a_7xy^3 + a_8xy^2 + a_9xy + a_{10}x + a_{11}y^4 + a_{12}y^3 + a_{13}y^2 + a_{14}y + a_{15}$ approximating k_{11}, k_{22} and k_{33}	37
3.5	The fourth-order polynomial functions: $a_1x^4 + a_2x^3y + a_3x^3 + a_4x^2y^2 + a_5x^2y + a_6x^2 + a_7xy^3 + a_8xy^2 + a_9xy + a_{10}x + a_{11}y^4 + a_{12}y^3 + a_{13}y^2 + a_{14}y + a_{15}$ approximating k_{12}, k_{13} and k_{23}	38
3.6	L2-norm errors of the components of the permeability \mathbf{k}	39
4.1	Characteristic parameters	54
5.1	L_2 -norm error of the velocity for the Stokes-Brinkman equations where θ is the angle between the array of cylinders and the horizontal plane.	81
5.2	L_2 -norm errors of the numerical and exact solutions of Stokes-Brinkman equations when the numbers of elements are increasing where $\#$ dof is the number of degrees of freedom and Δx is the uniform length of each element.	84

1. INTRODUCTION

Cilia are hairlike organelles that line the surfaces of the ciliated cells and beat in rhythmic waves. They provide locomotion to liquids along the epithelium, the lining of the cavity of structures throughout the body. Cilia are essentially omnipresent in the human body and play a considerable role in a number of processes. Of particular interest to us are the movement of cilia in the lungs which aids in removing fluids, pathogens, and foreign particles out of the airway and out of the lungs.

Figure 1.1 shows a portion of mucosa in bronchuses and bronchioles in the respiratory system and in the lungs. The patchwork consists of goblet cells containing mucus granules, cilia and a mucus blanket. The function of the goblet cells is to secrete mucin, heavily glycosylated proteins, to form the mucus that traps the foreign particles and form a blanket at the tip of the cilia [101]. The cilia exist in a low-viscosity fluid and together this layer is called the periciliary layer (PCL), [95, 63]. The mucus, which is a highly viscous fluid, resides above the PCL [69]. To prevent mucus accumulation in the lungs, the cilia beat in an almost two-dimensional plane. The effective bending of cilia induces the movement of the PCL fluid which in turn, propels the mucus. They do this by beating backward and forward to generate metachronal waves that give the mucus a net flow in one direction. In the forward stroke, cilia are fully extended and penetrate the mucous layer. During the backward stroke, they bend close to the epithelium, the base, and rotate back to the starting point of the forward stroke. Gueron and Levit-Gurevich [45] stated that for a single cilia beating in water, the mechanical work load done during the backward stroke is five times less than the the amount of work done during the forward stroke. The process of producing mucus to entrap foreign particles and clearing them is called mucociliary clearance or muco-ciliary transport, [65, 70, 94, 101]. Further understanding of mucociliary clearance mechanisms of the respiratory tract can be found in [93].

Damage to the mucociliary clearance mechanism can occur with the absence of sufficient mucus or excess mucus [87]. For example, when the glands that produce mucus do not

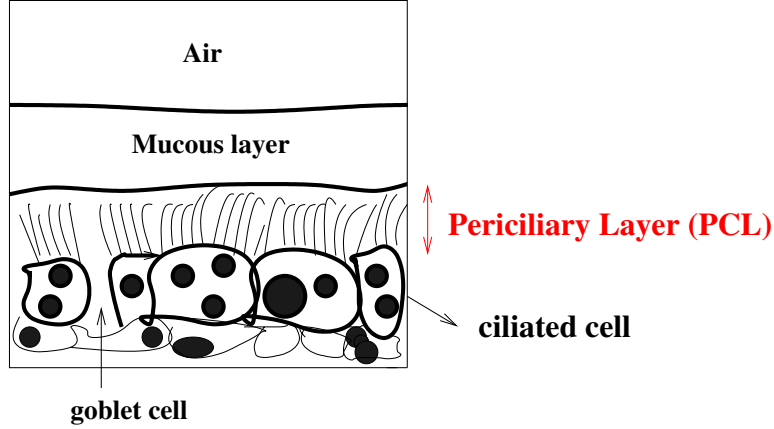


Figure 1.1: Cartoon picture of a patchwork of goblet and ciliated cells at the epithelium

function properly, thick mucus accumulates in the lungs, leading to breathing difficulties that cause airway diseases such as cystic fibrosis, asthma, emphysema, and chronic bronchitis. If the ciliated epithelium is damaged, coughing is the only mechanism for clearance [102].

There have been several models proposed for the PCL. Several papers by John Blake analytically model the movements and the velocities of a single cilium on microorganisms, [16, 17, 18, 19, 20]. In particular, Blakes 1973 and 1977 ([17] and [20]) provide a model for mucus flows in the respiratory portion and the maximum velocities of cilia in lungs, respectively. He used the Stokes equation to model the fluid and to model the cilia. He inserted a distribution of force singularities located along the center line of the cilia and calculated the velocity of a single cilium. For an array of cylinders, he assumed the average fluid velocity is equal to the spatially averaged cilia velocity in the PCL. Other analytic studies of mucous flow caused by ciliary motion include Barton and Raynor, [5], who analytically studied the mucous flow due to the movement of a single cilium and compared the results with experimental data, and Liron [64] who considered the fluid transport by cilia using Green's function for a surface distribution of point forces of the Stokes equation (Stokeslet) between two parallel plates. His analytical method was the same as Blake but he assumed the total velocity in a domain consists of a plane Poiseuille flow and the Stokeslet distribution on all cilia to have non-zero

flux where the plane Poiseuille flow was considered as disposal later on. However, the integral equations for the force distribution is not sufficient to determine the forces uniquely.

Experimentally, Rabinovitch's [83] applied a light-transmission method to study the ciliary movement but not the velocity of the PCL fluid while Frommer and Steele [42] constructed rows of hair cell cilia bundles found in the mammalian cochlea where the pressure was required to produce a given volume of flow rate through the obstacles. Note that in their experiments the cilia was motionless or not self-propelled.

In this study, we develop a model using an upscaling technique so that we do not have to consider the motion of each individual cilium but rather what all cilia do collectively, i.e. the cilia can be viewed as a porous medium with the self-propelled solid phase, cilia, composed of a periodic array of cylinders. Figure 1.2 illustrates a two-dimensional domain of interest, the PCL and mucous layers. The goal of this research is to model the PCL as a thin porous medium with a solid phase composed of a moving periodic array of cylinders and a liquid phase composed of the low viscosity PCL fluid. The left drawing in Figure 1.2 shows the cilia when they are perpendicular to the horizontal plane, and the right illustrates the cilia at an angle θ . The length and height of our computational cell domain are L_c and H_c , respectively. We define H_{c2} as the height of the cilia, which is a function of time, and $H_{c1} = H_c - H_{c2}$. We then define

$$\Omega_1 = L_c \times H_{c1} \tag{1.1}$$

as the domain containing the low viscosity fluid without cilia and

$$\Omega_2 = L_c \times H_{c2} \tag{1.2}$$

as the domain containing cilia with low viscosity fluid. Since Ω_2 contains both the fluid and solid, this domain is a porous medium. Because H_{c1} and H_{c2} change in time, Ω_1 and Ω_2 are functions of time as well. Note that Ω_1 is cannot be treated as a porous medium.

In Ω_2 we model the cilia as a periodic array of cylinders that rotate about their base where the height of Ω_2 is a function of time. Figure 1.3 shows an example of a cell array

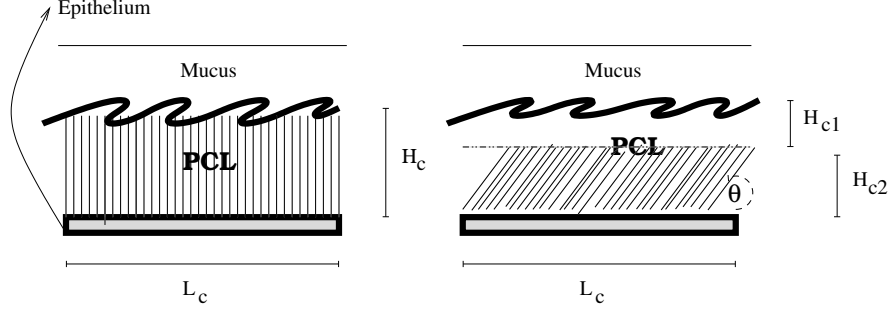


Figure 1.2: The PCL and mucous layers where $\Omega = H_c \times L_c$ is our computational domain with subdomains $\Omega_1 = L_c \times H_{c1}$ and $\Omega_2 = L_c \times H_{c2}$.

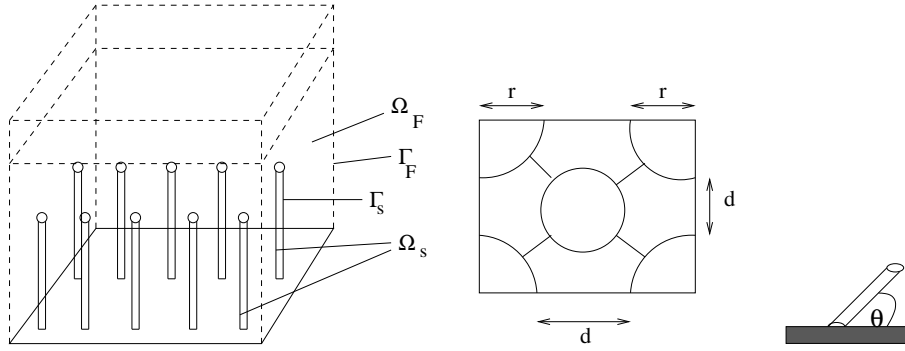


Figure 1.3: Geometry: an ideal cell of cylinders when the angle between cylinders and horizontal plane is 90 degrees; the top view of the left figure ; the angle θ between the cylinder and the horizontal plane.

of cylinders and illustrates the geometry of our model. The left cartoon displays an ideal cell of cylinders when the angle between cylinders and horizontal plane is 90 degrees. The top view of the left figure and the angle θ between the cylinder and the horizontal plane are demonstrated in the middle and right cartoons respectively. In the middle picture, r is the radius of the cylinder and d is the distance between cylinders. The relationship between d and r is $d = l_c - 2r$ where l_c is the length of the square domain. If $l_c = 0.5$, the cylinders touch when the distance d_1 in the Figure 1.3 is zero or the radius r is 0.175. To find a model of the PCL, we need to calculate the permeability, a measure of the ease with which a liquid can move through a porous material.

For an array of parallel cylinders, various experimental [105, 107, 108, 14, 26, 29, 32, 98] and analytical [48, 49, 59, 96] approaches have been performed to calculate the permeability

or drag for flow both perpendicular and parallel to an array of cylinders, as well as numerical studies, [2, 91]. Alcocer and Singh [2] investigated the movement of viscoelastic liquids passing through the periodic arrays of cylinders in a two-dimensional domain using a finite element method. Sangani and Acrivos [91] determined solutions, such as the drag on a cylinder, for the slow flow past a square and a hexagonal array of cylinders in a two-dimensional domain. In these, authors found the permeability when the cylinders are perpendicular or aligned with the horizontal plan. Most numerical works calculated the permeability for a two-dimensional domain. In this work, although the cilia rotate three-dimensionally, they beat in an almost two-dimensional plane. Therefore, the permeability is calculated as a function of only one angle, θ , and the cylinder density in three-dimensions.

In order to obtain the permeability, homogenization is applied to the periodic cell array of cylinders to obtain a system of equations which can be solved to numerically approximate the permeability tensor. A three-dimensional mixed finite element method using Taylor-Hood elements is employed to solve the system of equations. Moreover, we provide polynomial approximations of each entry of the permeability tensor as a function of a ratio r/d and the angle θ .

For a model of the fluid flow in the PCL, we consider a coupled free-fluid/porous-medium system of equations. Typically, Stokes or Navier-Stokes equations are used to determine the flow in domain Ω_1 while Darcy's Law or the Brinkman equation is employed in Ω_2 , [33, 73, 99]. Morandotti [73] employed the Brinkman equation to model the fluid phase of a porous medium for modeling the motion of a deforming body in a viscous fluid. Chen, Gunzburger and Wang [33] compared both the Stokes-Darcy and Stokes-Brinkman equations with the same boundary conditions. They concluded that Stokes-Darcy equations with the Beavers-Joseph condition are more precise than others. Because of our slow flow problem, Stokes equation is employed in domain Ω_1 . For the domain Ω_2 , since there is a transition region at the free-fluid/porous-medium interface where the porous medium and free-fluid regions are adjacent, we employ the Brinkman equation. This is because the introduction

of an effective viscosity parameter in the additional term of Darcy's Law in the Brinkman equation can better handle the force from stress at the interface so that solutions from the Stokes equation can be matched with those of Darcy's law at the interface [66]. Although the Brinkman equation is more complicated equation than Darcy's Law, appropriated boundary conditions can be applied. Moreover, it is more convenient for coding. More information about boundary conditions of the Stokes-Brinkman and Stokes-Darcy equations can be found in [3, 30, 31, 47, 56, 57, 62, 67, 68, 75, 99].

Although in practice the PCL/mucus interface is a free boundary (with the unknown height of the PCL), as a first approximation, we propose numerically modelling the PCL fluid with a fixed boundary height. The well-posedness of the Navier-Stokes equation and the Navier-Stokes/Brinkman for constant coefficients can be found in [100] and [54], respectively. The existence and uniqueness of the Stokes-Brinkman equation for the numerical problem for a tensor coefficient are shown in this work.

In Chapter 2, we discuss the permeability tensor and how it relates to a drag coefficient. We apply the homogenization method to the periodic cell array of cylinders to obtain the system of equations which is used to determine the permeability tensor. These equations are discretized in Chapter 3 and solved using a Mixed Finite Element method and where the numerical results are verified. Because the Kozeny-Carman equation is among the more popular equations to determine the permeability, we compare $1/3$ the trace of the numerical permeability tensor with the Kozeny-Carman equation in Chapter 3.

In Chapter 4, we model the PCL using the Stokes-Brinkman equation. We also show the existence and uniqueness of the discretized Stokes-Brinkman equations. The numerical results of the equations are presented in Chapter 5. In the case of a constant velocity on the top of the two-dimensional domain, we proceed to compare the numerical result with the exact solution [58]. In Chapter 6, we begin to investigate modeling the PCL with a free boundary. Finally, we summarize our results in Chapter 7.

It should be noted that to the author's knowledge this is the first time the porous media

equations are being used to model a fluid flowing due to the movement of the solid phase. Classical porous-media flow problems involve a static solid phase with a liquid-phase pressure gradient inducing fluid flow.

2. HOMOGENIZATION

In this Chapter we develop the equations that are solved to determine the permeability for the PCL where there are cilia. We choose homogenization because it is a method used to upscale governing equations e.g. Stokes equation, from the microscopic to the macroscopic scale, and has been widely used since the 1970s [13]. The strength of this method is that for a given microscopic geometry, the coefficients in the macroscopic equations can be found explicitly. In particular, by using homogenization to upscale the Stokes equation with periodicity requirement we obtain a system of equations that can be used to determine the permeability. In this Chapter, we summarize the homogenization method as following. For more details, see e.g. [13, 34, 51], and [90].

Let Ω be the periodic cell domain which consists of a fluid phase, Ω_F , a solid phase, Ω_S and a piecewise continuous liquid-solid interface $\Gamma = \Gamma_S \cup \Gamma_F$ where Γ_S and Γ_F are the boundaries of the solid and liquid phases respectively (see Figure 1.3). We assume slow fluid flow, a fixed solid and a viscous incompressible fluid, so that the Stokes equations are applicable:

$$\nabla \cdot \mathbf{v} = 0 \quad \text{in } \Omega_F \quad (2.1)$$

$$-\nabla p + \mu \Delta \mathbf{v} + \mathbf{f}^s = \mathbf{0} \quad \text{in } \Omega_F \quad (2.2)$$

where we also assume a no-slip boundary condition on Γ_S ; μ is the dynamic viscosity; \mathbf{v} is the velocity; p is the pressure and \mathbf{f}^s is a source term. Next, we assume the diameter of the cylinders, $a = 2r$, see Figure 1.3, is small compared to a macroscopic scale length L which can be the length of a bronchiole in the lungs; i.e. if $\epsilon = a/L$, then $\epsilon \ll 1$. Let \mathbf{x} be a macroscopic variable and define the microscopic variable or the stretched coordinate $\mathbf{y} = \mathbf{x}/\epsilon$. The dynamic viscosity coefficient μ is assumed fixed and independent of ϵ . Figure 2.1 shows a reference cell Y which is periodic and the period is ϵY . Figure 2.2 demonstrates the upscaling procedure where $\epsilon > 0$ is a spatial scale parameter. When ϵ tends to zero, we

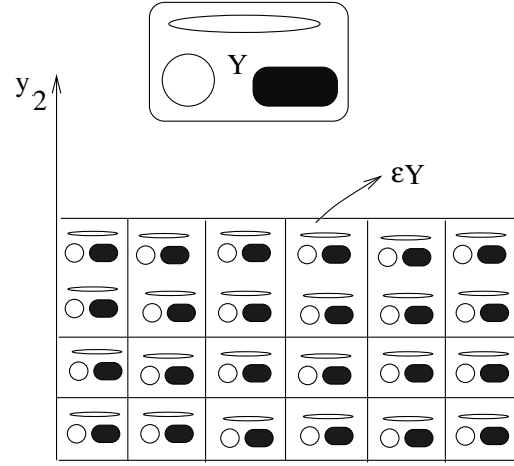


Figure 2.1: A reference heterogeneities Y are periodic of period ϵY and their size is order of ϵ .

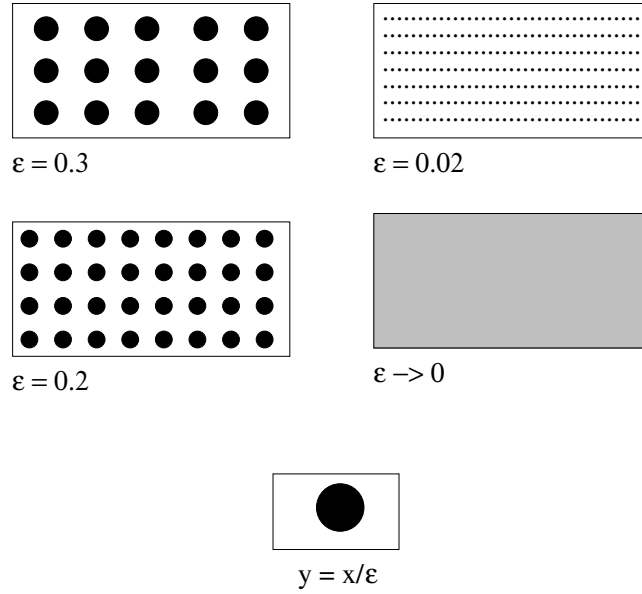


Figure 2.2: Upscaling procedure where $\epsilon > 0$ is a spatial parameter.

have the macroscopic scale.

We consider an asymptotic expansion of \mathbf{v} and p , in the form,

$$\mathbf{v} = \epsilon^\alpha(\mathbf{v}^0(\mathbf{x}, \mathbf{y}) + \epsilon \mathbf{v}^1(\mathbf{x}, \mathbf{y}) + \dots) \quad \text{and} \quad p = \epsilon^\beta(p^0(\mathbf{x}, \mathbf{y}) + \epsilon p^1(\mathbf{x}, \mathbf{y}) + \dots) \quad (2.3)$$

where \mathbf{v}^i and p^i are Ω -periodic in \mathbf{y} , and α and β are nonzero parameters that yield a physically meaningful solution. The choice of α and β yields different macroscopic models, and in this case we choose α and β to yield a nonzero macroscopic first-order pressure and a second-order velocity which can lead to obtaining Darcy's Law. It is known to be a reasonable equation for modeling slow flow through a porous medium. Recall that, for three-dimensional

$$\mathbf{x} = (x_1, x_2, x_3) \quad \text{and} \quad \mathbf{y} = (y_1, y_2, y_3) = \frac{1}{\epsilon}(x_1, x_2, x_3), \quad (2.4)$$

then we apply the chain rule to (2.4), the first and second derivatives with respect to x_j are

$$\frac{d}{dx_j} = \frac{\partial}{\partial x_j} + \frac{\partial}{\partial y_j} \frac{\partial y_j}{\partial x_j} = \frac{\partial}{\partial x_j} + \frac{1}{\epsilon} \frac{\partial}{\partial y_j} \quad (2.5)$$

and

$$\begin{aligned} \frac{d^2}{dx_j^2} &= \frac{\partial}{\partial x_j} \left(\frac{\partial}{\partial x_j} + \frac{1}{\epsilon} \frac{\partial}{\partial y_j} \right) + \frac{\partial}{\partial y_j} \left(\frac{\partial}{\partial x_j} + \frac{1}{\epsilon} \frac{\partial}{\partial y_j} \right) \frac{\partial y_j}{\partial x_j} \\ &= \frac{\partial^2}{\partial x_j^2} + \frac{1}{\epsilon} \frac{\partial^2}{\partial x_j \partial y_j} + \frac{1}{\epsilon} \left(\frac{\partial^2}{\partial y_j \partial x_j} + \frac{1}{\epsilon} \frac{\partial^2}{\partial y_j^2} \right) \\ &= \frac{1}{\epsilon^2} \frac{\partial^2}{\partial y_j^2} + \frac{1}{\epsilon} \left(\frac{\partial^2}{\partial x_j \partial y_j} + \frac{\partial^2}{\partial y_j \partial x_j} \right) + \frac{\partial^2}{\partial x_j^2}. \end{aligned} \quad (2.6)$$

Therefore, the vector Laplacian of the velocity field is

$$\begin{aligned}
\Delta \mathbf{v} &= \left(\frac{d^2 v_1}{dx_j^2}, \frac{d^2 v_2}{dx_j^2}, \frac{d^2 v_3}{dx_j^2} \right) \\
&= \left(\frac{1}{\epsilon^2} \frac{\partial^2 v_1}{\partial y_j^2} + \frac{1}{\epsilon} \left(\frac{\partial^2 v_1}{\partial x_j \partial y_j} + \frac{\partial^2 v_1}{\partial y_j \partial x_j} \right) + \frac{\partial^2 v_1}{\partial x_j^2}, \right. \\
&\quad \frac{1}{\epsilon^2} \frac{\partial^2 v_2}{\partial y_j^2} + \frac{1}{\epsilon} \left(\frac{\partial^2 v_2}{\partial x_j \partial y_j} + \frac{\partial^2 v_2}{\partial y_j \partial x_j} \right) + \frac{\partial^2 v_2}{\partial x_j^2}, \\
&\quad \left. \frac{1}{\epsilon^2} \frac{\partial^2 v_3}{\partial y_j^2} + \frac{1}{\epsilon} \left(\frac{\partial^2 v_3}{\partial x_j \partial y_j} + \frac{\partial^2 v_3}{\partial y_j \partial x_j} \right) + \frac{\partial^2 v_3}{\partial x_j^2} \right), \\
&= \frac{1}{\epsilon^2} \left[\frac{\partial^2 v_1}{\partial y_j^2}, \frac{\partial^2 v_2}{\partial y_j^2}, \frac{\partial^2 v_3}{\partial y_j^2} \right] \\
&\quad + \frac{1}{\epsilon} \left[\frac{\partial^2 v_1}{\partial x_j \partial y_j} + \frac{\partial^2 v_1}{\partial y_j \partial x_j}, \frac{\partial^2 v_2}{\partial x_j \partial y_j} + \frac{\partial^2 v_2}{\partial y_j \partial x_j}, \frac{\partial^2 v_3}{\partial x_j \partial y_j} + \frac{\partial^2 v_3}{\partial y_j \partial x_j} \right] \\
&\quad + \left[\frac{\partial^2 v_1}{\partial x_j^2}, \frac{\partial^2 v_2}{\partial x_j^2}, \frac{\partial^2 v_3}{\partial x_j^2} \right] \\
&= \frac{1}{\epsilon^2} \Delta_y \mathbf{v} + \frac{1}{\epsilon} \Delta_{xy} \mathbf{v} + \Delta_x \mathbf{v}
\end{aligned}$$

where

$$\Delta_y \mathbf{v} = \left(\frac{\partial^2 v_1}{\partial y_j^2}, \frac{\partial^2 v_2}{\partial y_j^2}, \frac{\partial^2 v_3}{\partial y_j^2} \right); \quad \Delta_x \mathbf{v} = \left(\frac{\partial^2 v_1}{\partial x_j^2}, \frac{\partial^2 v_2}{\partial x_j^2}, \frac{\partial^2 v_3}{\partial x_j^2} \right)$$

and

$$\Delta_{xy} \mathbf{v} = \left(\frac{\partial^2 v_1}{\partial x_j \partial y_j} + \frac{\partial^2 v_1}{\partial y_j \partial x_j}, \frac{\partial^2 v_2}{\partial x_j \partial y_j} + \frac{\partial^2 v_2}{\partial y_j \partial x_j}, \frac{\partial^2 v_3}{\partial x_j \partial y_j} + \frac{\partial^2 v_3}{\partial y_j \partial x_j} \right)$$

where a repeated index j within a single term indicates summation, i.e. $\frac{d^2 v_1}{dx_j^2} = v_{1,jj} =$

$$\sum_{j=1}^3 \frac{d^2 v_1}{dx_j^2}.$$

Substituting (2.5) into (2.1) yields

$$0 = \nabla \cdot \mathbf{v} = \frac{dv_j}{dx_j} = \frac{\partial v_j}{\partial x_j} + \frac{1}{\epsilon} \frac{\partial v_j}{\partial y_j} = \nabla_x \cdot \mathbf{v} + \frac{1}{\epsilon} \nabla_y \cdot \mathbf{v}, \quad (2.7)$$

where

$$\nabla_x \cdot \mathbf{v} = \frac{\partial v_j}{\partial x_j} \quad \text{and} \quad \nabla_y \cdot \mathbf{v} = \frac{\partial v_j}{\partial y_j}. \quad (2.8)$$

Similarly, substituting (2.5) and (2.6) into the Stokes equation (2.2) yields

$$-\nabla_x p - \frac{1}{\epsilon} \nabla_y p + \mu \left(\frac{1}{\epsilon^2} \Delta_y \mathbf{v} + \frac{1}{\epsilon} \Delta_{xy} \mathbf{v} + \Delta_x \mathbf{v} \right) + \mathbf{f}^s = \mathbf{0}. \quad (2.9)$$

After some trials and errors we found that in order to find a non-zero and physically meaningful solution, we let $\alpha = 2$ and $\beta = 0$ so that

$$\mathbf{v} = \epsilon^2(\mathbf{v}^0(\mathbf{x}, \mathbf{y}) + \epsilon \mathbf{v}^1(\mathbf{x}, \mathbf{y}) + \dots) \quad (2.10)$$

$$p = \epsilon^0(p^0(\mathbf{x}, \mathbf{y}) + \epsilon p^1(\mathbf{x}, \mathbf{y}) + \dots) \quad (2.11)$$

where, again, the function v^i and p^i are Ω -periodic in the microscale \mathbf{y} . Substituting (2.10) and (2.11) into (2.8) and (2.9), we have

$$\nabla_x \cdot (\epsilon^2 \mathbf{v}^0(\mathbf{x}, \mathbf{y}) + \epsilon^3 \mathbf{v}^1(\mathbf{x}, \mathbf{y}) + \dots) + \frac{1}{\epsilon} \nabla_y \cdot (\epsilon^2 \mathbf{v}^0(\mathbf{x}, \mathbf{y}) + \epsilon^3 \mathbf{v}^1(\mathbf{x}, \mathbf{y}) + \dots) = 0 \quad (2.12)$$

and

$$\begin{aligned} & -\nabla_x(p^0(\mathbf{x}, \mathbf{y}) + \epsilon p^1(\mathbf{x}, \mathbf{y}) + \dots) - \frac{1}{\epsilon} \nabla_y(p^0(\mathbf{x}, \mathbf{y}) + \epsilon p^1(\mathbf{x}, \mathbf{y}) + \dots) \\ & + \mu \frac{1}{\epsilon^2} \Delta_y \epsilon^2(\mathbf{v}^0(\mathbf{x}, \mathbf{y}) + \epsilon \mathbf{v}^1(\mathbf{x}, \mathbf{y}) + \dots) + \frac{\mu}{\epsilon} \Delta_{xy} \epsilon^2(\mathbf{v}^0(\mathbf{x}, \mathbf{y}) + \epsilon \mathbf{v}^1(\mathbf{x}, \mathbf{y}) + \dots) \\ & + \mu \Delta_x \epsilon^2(\mathbf{v}^0(\mathbf{x}, \mathbf{y}) + \epsilon \mathbf{v}^1(\mathbf{x}, \mathbf{y}) + \dots) + \mathbf{f}^s = \mathbf{0}. \end{aligned} \quad (2.13)$$

Collecting the same orders of ϵ ($O(\epsilon)$ from (2.12), and $O(\epsilon^{-1})$ and $O(\epsilon^0)$ from (2.13)), we have the differential equations

$$\nabla_y \cdot \mathbf{v}^0(\mathbf{x}, \mathbf{y}) = 0 \quad (2.14)$$

$$\nabla_y p^0(\mathbf{x}, \mathbf{y}) = 0 \quad (2.15)$$

$$-\nabla_x p^0(\mathbf{x}, \mathbf{y}) - \nabla_y p^1(\mathbf{x}, \mathbf{y}) + \mu \Delta_y \mathbf{v}^0(\mathbf{x}, \mathbf{y}) + \mathbf{f}^s = \mathbf{0}. \quad (2.16)$$

Note that, from equation (2.15),

$$\left(\frac{\partial p^0}{\partial y_1}, \frac{\partial p^0}{\partial y_2}, \frac{\partial p^0}{\partial y_3} \right) = (0, 0, 0).$$

Then p^0 depends only on x , i.e.

$$p^0 = p^0(x). \quad (2.17)$$

For the no-slip boundary condition, we have $\mathbf{v} = \mathbf{0}$, i.e.,

$$\epsilon^2(\mathbf{v}^0(\mathbf{x}, \mathbf{y}) + \epsilon \mathbf{v}^1(\mathbf{x}, \mathbf{y}) + \dots) = \mathbf{0}.$$

Hence,

$$\mathbf{v}^0 = 0 \quad \text{on } \Gamma. \quad (2.18)$$

Since the domain is assumed to be periodic, we introduce a Hilbert space of Ω -periodic functions:

$$H(\Omega) = \{\omega : \omega = (\omega_1, \omega_2, \omega_3) \in (H^1(\Omega_F))^3 : \omega \text{ is } \Omega\text{-periodic, } \omega = 0 \text{ on } \Gamma_S, \nabla_y \cdot \omega = 0\} \quad (2.19)$$

with scalar product:

$$(\mathbf{w}, \omega)_{H(\Omega)} = \int_{\Omega_F} \frac{\partial w_j}{\partial y_k} \frac{\partial \omega_j}{\partial y_k} dy \quad (2.20)$$

where again the repeat index j and k indicate summation. Note that this is a scalar product because \mathbf{w} and ω are zero on the boundary Γ . Equation (2.16) can be rewritten in the indicial notation as

$$- \int_{\Omega_F} \frac{\partial p^1}{\partial y_i} dy + \mu \int_{\Omega_F} \frac{\partial^2 v_i^o}{\partial y_j^2} dy - \int_{\Omega_F} \frac{\partial p^0}{\partial x_i} dy + \int_{\Omega_F} f_i^s dy = 0. \quad (2.21)$$

To obtain a weak form of the equation, we multiply (2.21) by a test function $\omega_i \in H(\Omega)$ and then integrate the equation, we have

$$- \int_{\Omega_F} \omega_i \frac{\partial p^1}{\partial y_i} dy + \mu \int_{\Omega_F} \omega_i \frac{\partial^2 v_i^o}{\partial y_j^2} dy - \int_{\Omega_F} \omega_i \frac{\partial p^0}{\partial x_i} dy + \int_{\Omega_F} f_i^s \omega_i dy = 0 \quad (2.22)$$

where, in this Chapter, the repeat index i refers to the number of equations while the other repeat indices indicate summation and $\mathbf{f}^s = (f_1^s, f_2^s, f_3^s)$. Integrating by parts the first two terms, using the fact that $\omega_i = 0$ on Γ , and p^o and f_i^s are functions of x only, we have

$$\int_{\Omega_F} p^1 \frac{\partial \omega_i}{\partial y_i} dy - \mu \int_{\Omega_F} \frac{\partial v_i^o}{\partial y_j} \frac{\partial \omega_i}{\partial y_j} dy - \left(\frac{\partial p^0}{\partial x_i} - f_i^s \right) \int_{\Omega_F} \omega_i dy = 0$$

Employing the divergence-free property of the test function, $\frac{\partial \omega_i}{\partial y_i} = \nabla_y \cdot \omega = 0$, the first integration is zero, and we have the simplified expression

$$\mu \int_{\Omega_F} \frac{\partial v_i^o}{\partial y_j} \frac{\partial \omega_i}{\partial y_j} dy = \left(f_i^s - \frac{\partial p^0}{\partial x_i} \right) \int_{\Omega_F} \omega_i dy,$$

where we sum on $j = 1, 2, 3$ for each $i = 1, 2, 3$. Using the definition (2.20) of the inner product yields

$$\mu(\mathbf{v}^0, \omega)_H = \left(\mathbf{f}^s - \nabla_x p^0 \right) \cdot \int_{\Omega_F} \omega dy \quad \forall \omega \in H(\Omega) \quad (2.23)$$

Consequently, the problem given by equations (2.14), (2.16), and (2.18) is equivalent to the variational problem: Find $\mathbf{v}^0 \in H(\Omega)$ satisfying equation (2.23).

To show that there exists a unique solution $\mathbf{v}^0 \in H(\Omega)$ of (2.23) using Lax-Milgram Theorem, we define $a(\mathbf{w}, \omega) = \mu(\mathbf{w}, \omega)_{H(\Omega)}$ which is bilinear. Note that

$$a(\omega, \omega) = \mu(\omega, \omega)_{H(\Omega)} = \mu \|\omega\|_{H(\Omega)}^2 \quad \forall \omega \in H(\Omega) \quad (2.24)$$

is also coercive and

$$|a(\mathbf{w}, \omega)| = |\mu| |(\mathbf{w}, \omega)_{H(\Omega)}| \leq \mu \|\mathbf{w}\|_{H(\Omega)} \|\omega\|_{H(\Omega)} \quad \forall \mathbf{w}, \omega \in H(\Omega) \quad (2.25)$$

can be shown to be continuous by applying the Cauchy-Schwarz inequality to the last inequality. Define the linear functional

$$F(\omega_i) = \left(f_i^s - \frac{\partial p^0}{\partial x_i} \right) \int_{\Omega_F} \omega_i dy \quad (2.26)$$

and note that

$$|F(\omega_i)| = \left| \left(f_i^s - \frac{\partial p^0}{\partial x_i} \right) \right| \left| \int_{\Omega_F} \omega_i dy \right| \leq \left(\|f_i^s\| + \left\| \frac{\partial p^0}{\partial x_i} \right\| \right) \|\omega_i\|_{H^1(\omega)}, \quad (2.27)$$

so it is continuous. By applying the Lax-Milgram Theorem, we know there exists a unique \mathbf{v}^0 satisfying (2.23).

The solution \mathbf{v}^0 of (2.23) can be used to derive Darcy's Law. Along the way to formulate Darcy's Law we obtain a system of equations that can be employed to calculate the permeability. Applying the linearity property, we have

$$\mathbf{v}^0 = \frac{1}{\mu} \left(f_i^s - \frac{\partial p^0}{\partial x_i} \right) \mathbf{u}^i \quad (2.28)$$

where \mathbf{u}^i is the only solution of the problem: Find $\mathbf{u}^i \in H(\Omega)$ such that

$$(\mathbf{u}^i, \omega)_{H(\Omega)} = \int_{\Omega_F} \omega_i dy \quad (2.29)$$

for all $\omega \in H(\Omega)$. Thus, \mathbf{u}^i is the weak solution of the following strong formulation

$$\nabla_y \cdot \mathbf{u}^i = 0 \quad \text{in } \Omega_F \quad (2.30)$$

$$-\nabla_y q^i + \Delta_y \mathbf{u}^i + \mathbf{e}^i = 0 \quad \text{in } \Omega_F \quad (2.31)$$

$$\mathbf{u}^i = 0 \quad \text{on } \Gamma, \quad (2.32)$$

where ∇_y and Δ_y represent the gradient and laplacian operators with respect to the microscopic scale y ; \mathbf{u}^i and q^i are Ω -periodic, and \mathbf{e}^i is the unit vector in the direction of the y_i axis, $i = 1, 2, 3$. The solution \mathbf{u}^i of the system of equations (2.30)-(2.32) can be used to compute the permeability. Note that $\mathbf{v}^0, \mathbf{v}^1, \mathbf{u}^i$ are defined on Ω_F . To obtain the Darcy's velocity, It is natural to extend them to Ω with zero values on Ω_S . Define

$$\widetilde{\mathbf{v}}^0 = \frac{1}{|\Omega|} \int_{\Omega_F} \mathbf{v}^0 dy, \quad \widetilde{\mathbf{v}}^1 = \frac{1}{|\Omega|} \int_{\Omega_F} \mathbf{v}^1 dy, \quad \text{and} \quad \widetilde{\mathbf{u}}^i = \frac{1}{|\Omega|} \int_{\Omega_F} \mathbf{u}^i dy. \quad (2.33)$$

Integrating (2.28) and then dividing by the volume of the domain Ω , we have

$$\widetilde{\mathbf{v}}^0 = \frac{1}{\mu} \left(f_i^s - \frac{\partial p^0}{\partial x_i} \right) \widetilde{\mathbf{u}}^i \quad (2.34)$$

which in the indicial notation, is

$$\widetilde{v}_j^0 = \frac{1}{\mu} \left(f_i^s - \frac{\partial p^0}{\partial x_i} \right) \widetilde{u}_j^i. \quad (2.35)$$

Equation (2.35) is Darcy's Law and \widetilde{u}_j^i is the permeability tensor which depends on the geometry of the periodic domain Ω . In general, we write equation (2.35) as

$$\mathbf{q} = -\frac{\mathbf{k}}{\mu} (\nabla p - \mathbf{f}^s) \quad (2.36)$$

where

$$k_{ij} = \widetilde{u}_j^i = \frac{1}{|\Omega|} \int_{\Omega_F} u_j^i dy \quad (2.37)$$

is the permeability.

For example, with $\rho = \text{constant}$ and the source term $\mathbf{f}^s = -\rho g \nabla z$ where z is the z -axis in the Cartesian coordinate, [7] page 134, (2.36) becomes

$$\mathbf{q} = -\frac{\rho g \mathbf{k}}{\mu} \cdot \nabla \left(\frac{p}{\rho g} + z \right) = -\mathbf{K} \cdot \nabla h. \quad (2.38)$$

In (2.38), we observe that $h = p/\rho g + z$ which is identical to the piezometric head from the Darcy's experiment and $\mathbf{K} = \rho g \mathbf{k}/\mu$ is the hydraulic conductivity ($[\mathbf{K}] = \text{L/T}$). Note that the variational form of (2.30)–(2.32) is: Find $\mathbf{u}^i \in H(\Omega)$ such that

$$\int_{\Omega_F} \nabla_y \mathbf{u}^i : \nabla_y \omega = \int_{\Omega_F} \omega_i dy \quad (2.39)$$

for all $\omega \in H(\Omega)$ and then the permeability can be determined and validated from the formula (2.39) by replacing ω_i with u_j^i and dividing by the volume of the domain Ω . An consequence of the above statement is that tensor \mathbf{k} is symmetric and positive definite matrix, meaning that the diagonal entries are all positive [90]. This also proves that the fluid moves in the direction of increasing head gradient. From equation (2.37), we observe that \mathbf{k} depends on the actual size of the microscopic scale. Thus, the non-dimensional form of the system (2.30–2.32) is important and can be derived as following. For simplicity, we drop the superscript i in (2.30–2.32) and note that both \mathbf{u} and \mathbf{e} are vectors for each i with scalar q . Let $\mathbf{y}^* = \mathbf{y}/a$, $\mathbf{u}^* = \mathbf{u}/a^2$, $q^* = q/a$ and the domain Ω is mapped to Ω^* of unit size (a cube), $a = \text{diameter of the cilia}$. Hence, the dimensionless form is

$$\nabla_{y^*} \cdot \mathbf{u}^* = 0 \quad \text{on} \quad \Omega_F^* \quad (2.40)$$

$$-\nabla_{y^*} q^* + \Delta_{y^*} \mathbf{u}^* + \mathbf{e}^* = 0 \quad \text{on} \quad \Omega_F^* \quad (2.41)$$

$$\mathbf{u}^* = 0 \quad \text{on} \quad \Gamma^* \quad (2.42)$$

Similarly, the dimensionless permeability

$$\mathbf{k}^* = \frac{1}{|\Omega^*|} \int_{\Omega_F^*} \mathbf{u}^* dy^* \quad (2.43)$$

and then the conductivity becomes

$$\mathbf{K} = \frac{\rho g a^2 \mathbf{k}^*}{\mu} \quad (2.44)$$

because $\mathbf{k} = a^2 \mathbf{k}^*$.

3. PERMEABILITY

In this Chapter, we use a mix finite element method to calculate the permeability of the system of equations obtained in Chapter 2.

In the past, H. Hasimoto [49] found theoretically periodic solutions of the Stoke's equation using the Fourier series and the drag force acting on a periodic array of spheres and circular cylinders in a two-dimensional domain. The series do not diverge because the mean pressure gradient is applied. The values of c , page 323, in the solutions which depend on the sphere volume fraction and are written as a sum of the sphere volume fraction have been calculated numerically by many authors. Once the drag force is determined, the permeability coefficients are known as well. The drag coefficient is used to quantify the resistance of an object in the fluid region, while the permeability is the measure of the ability of a porous media that permits the fluid to pass through it. Zick and Homsy [111] also began with the Stoke's equation and solved, using a different method from Hasimoto, for the drag force and then permeability of the periodic array of spheres. Although these authors had found the Stoke's solutions theoretically, numerical constants are still needed to determine the drag coefficient.

In this Chapter, we numerically calculate the solution of the system of equations (2.40)-(2.42). A mixed finite element method is applied to the system of equations and the variational formulation is formulated in Section 3.2 while the validation of the code is presented in Section 3.3. For the sphere case we compare our results with that of Rodrigo and Manuel [85] whose numerical solutions are checked with Zick and Homsy. Comparing the numerical results with experimental data leads to finding the relationship between the drag coefficient and permeability which is shown in Section 3.1. The numerical results and the polynomial approximations of the permeability tensors are demonstrated in Section 3.4. Finally, the famous Kozeny-Carman equation is also applied to find one of the closed forms of the numerical permeability, $1/3\text{tr}\mathbf{k}$, in Section 3.5.

3.1 Relationship between Drag Coefficient and Permeability

This section is written for the conversion of drag coefficient to permeability which is used in Section 3.3 comparing our numerical result with the experimental data from Sullivan, [98], who measured the drag coefficient of cylindrical fibers empirically. When dealing with porous media, we use the concept stated that the pressure gradient is the drag force. Before deriving the relationship, we present the drag coefficient of a sphere and cylinder. The drag force concept is commonly used to determine the force on a solid object due to the flow of fluid around it. By definition, the drag force \mathbf{F}^d exerted on each object by fluid is given by [111]

$$F_i^d = \int_{\Gamma_S} t_{ij}(\mathbf{x}) n_j(\mathbf{x}) d\mathbf{x} \quad (3.1)$$

where

$$t_{ij} = -p\delta_{ij} + \mu(v_{i,j} + v_{j,i}) \quad (3.2)$$

is the stress tensor; p is the pressure; δ_{ij} is the identity; $v_{i,j}$ or $v_{j,i}$ are the velocity gradients; n_j is the outward unit normal vector and Γ_S is the surface of the solid region. Zick and Homsy, [111] showed that the drag force on a single sphere in a periodic array of spheres is

$$F_i^d = 6\pi\mu r_p C_d (v_s)_i \quad (3.3)$$

where

$$v_s = \frac{1}{|\Omega|} \int_{\Omega_F} v_i(\mathbf{x}) d\mathbf{x} \quad (3.4)$$

is the superficial velocity; v_i is the velocity in the fluid region; $|\Omega|$ is a volume of the cell; r_p is the radius of the sphere and C_d is the drag coefficient. Note that the notations Ω and Ω_F are used in the same way as those in Chapter 2.

For a periodic array of cylinders, where the cylinders are perpendicular to the flow, Lamb [61] modified Oseens technique and linearized equations [78] to an array of cylinders. He

obtained the total drag force per unit length of a cylinder

$$F^d = 8\pi\mu C \quad (3.5)$$

where $C = U/[2.0(2.0 - \ln(Re))]$; $Re = aU\rho/\mu$ is the Reynolds number; U is the upstream velocity of fluid without the effect of cylinders; a is the diameter of the cylinder and ρ is the density of the fluid. When the flow aligns parallel to the cylinders, Iberall, [53] claimed that the drag coefficient of a cylinder in a cell is not the same as that of an isolated cylinder. Iberall [53] approximated the drag force on a cylinder enclosed by the other cylinders:

$$F^d = 4\pi\mu v_a \quad (3.6)$$

where $v_a = v_s/\epsilon^l$ is the average velocity of the fluid in a cell and v_s is the superficial velocity of the fluid in a cell and ϵ^l is the porosity. To be able to find a relationship between the drag coefficient and permeability, we follow a concept in the drag theory which states that the total drag force on the cylinders in a cell is the pressure drop across the cell, [32], i.e. the pressure gradient in Darcy's Law can be replaced by the drag force. Since the drag coefficient of a cylinder in a cell array and that of an isolated cylinder are different, we employ the pressure drop equation of Chen [32]. He included all of the drag forces on the cylinder in a cell as a pressure drop across the filter. His equation is:

$$\frac{\Delta p}{l} = \frac{2\epsilon^s \rho}{\pi C_v} C_d v_a^2 \frac{a_a}{a_s^2}, \quad (3.7)$$

where Δp is the pressure drop across a cell array of parallel, vertical, cylinders; l is the thickness of the cell; ϵ^s is the solid volume fraction; a_a and a_s are arithmetic average fiber and surface average fiber diameters of the cylinders in the cell respectively; C_d is the drag coefficient to be determined and C_v is a unit conversion factor, for example, $C_v = 980$ (g. mass cm.)/(g force sec.²) etc. As the fibers become more dense, the drag coefficient is modified via the volume fractions. For a periodic array of cylinder, our problem, (3.7) becomes

$$\frac{\Delta p}{l} = \frac{2\epsilon^s \rho}{\pi a} C_d v_a^2 \quad (3.8)$$

where $C_v = 1$ and $a_a = a_s^2 = 1/a$ and a is the diameter of the cylinder. Using $v_a = v_s/\epsilon^l$ as above, we have

$$\frac{\Delta p}{l} = \frac{2\epsilon^s \rho}{\pi a} C_d \frac{v_a}{\epsilon^l} v_s. \quad (3.9)$$

Applying Darcy's Law to (3.9) and, for simplicity, assuming all variables are scalars, the permeability and drag force coefficient are related by

$$k = \frac{\mu \pi a}{2\epsilon^s \rho} \frac{1}{C_d} \frac{\epsilon^l}{v_a} = \frac{\pi(1-\epsilon^s)a^2}{2\epsilon^s Re} \frac{1}{C_d} = \frac{2\pi(1-\epsilon^s)r^2}{\epsilon^s Re} \frac{1}{C_d}, \quad (3.10)$$

where $Re = \rho v_a a / \mu$ and r is the radius of the cylinder. Hence,

$$\frac{C_d}{2} Re = \frac{\pi(1-\epsilon^s)}{\epsilon^s} \frac{1}{k^*}, \quad (3.11)$$

where $k^* = k/r^2$ is the dimensionless permeability. Equation (3.11) will be used to calculate the dimensionless permeability from the drag coefficient.

3.2 Discretization of the Model Problem

In this section, we numerically approximate the solution to equations (2.40)-(2.42) using a mixed finite element method. This method is employed to obtain an approximate solution to the system of equations using a variational formulation [84]. Let

$$L_0^2(\Omega) = \{q \in L_2(\Omega) : \int_{\Omega} q \, dy = 0\}, \quad (3.12)$$

where q is a scalar periodic function and $L_2(\Omega) = W_2^0(\Omega)$ is the Sobolev space. In three-dimensions, the system of equations (2.40)-(2.41) can be rewritten as

$$\frac{\partial u_1^i}{\partial y_1} + \frac{\partial u_2^i}{\partial y_2} + \frac{\partial u_3^i}{\partial y_3} = 0 \quad (3.13)$$

$$\frac{\partial^2 u_1^i}{\partial y_1^2} + \frac{\partial^2 u_1^i}{\partial y_2^2} + \frac{\partial^2 u_1^i}{\partial y_3^2} = \frac{\partial q^i}{\partial y_1} - e_1^i \quad (3.14)$$

$$\frac{\partial^2 u_2^i}{\partial y_1^2} + \frac{\partial^2 u_2^i}{\partial y_2^2} + \frac{\partial^2 u_2^i}{\partial y_3^2} = \frac{\partial q^i}{\partial y_2} - e_2^i \quad (3.15)$$

$$\frac{\partial^2 u_3^i}{\partial y_1^2} + \frac{\partial^2 u_3^i}{\partial y_2^2} + \frac{\partial^2 u_3^i}{\partial y_3^2} = \frac{\partial q^i}{\partial y_3} - e_3^i \quad (3.16)$$

where the superscript $*$ is dropped for convenience and $e_j^i = 1$ if $j = i$ and $e_j^i = 0$ if $j \neq i$, $i = 1, 2, 3$. To preserve the symmetry of the stiffness global matrix, we multiply equation (3.13) by (-1) . After the multiplication, (3.13)–(3.16) can be rewritten in the indicial notation as

$$-\frac{\partial u_l^i}{\partial y_l} = 0, \quad (3.17)$$

$$-\frac{\partial q^i}{\partial y_j} + \frac{\partial^2 u_j^i}{\partial y_l^2} + \delta_{ij} = 0, \quad l = 1, 2, 3, \quad (3.18)$$

where again the double index l means the summation and δ_{ij} is the Kronecker delta. Note that the equation (3.18) can be rewritten as

$$-\frac{\partial}{\partial y_l} \left(q^i \delta_{jl} - \frac{\partial u_j^i}{\partial y_l} \right) + \delta_{ij} = 0, \quad l = 1, 2, 3. \quad (3.19)$$

Applying the mixed finite element method, [84], we multiply the equation (3.17) and (3.19) by test functions $(Q^i, \mathbf{w}^i) \in L_0^2(\Omega) \times H(\Omega)$, respectively,

$$-\int_{\Omega} Q^i \frac{\partial u_l^i}{\partial y_l} = 0, \quad (3.20)$$

$$\int_{\Omega} w_j^i \left(-\frac{\partial}{\partial y_l} \left(q^i \delta_{jl} - \frac{\partial u_j^i}{\partial y_l} \right) + \delta_{ij} \right) = 0, \quad l = 1, 2, 3 \quad (3.21)$$

where i indicates the number of system of equations. Employing the integration by parts [21] to (3.21),

$$-\int_{\Gamma} w_j^i \left(q^i \delta_{jl} - \frac{\partial u_j^i}{\partial y_l} \right) n_l + \int_{\Omega} \frac{\partial w_j^i}{\partial y_l} \left(q^i \delta_{jl} - \frac{\partial u_j^i}{\partial y_l} \right) = -\int_{\Omega} w_j^i \delta_{ij}, \quad l = 1, 2, 3. \quad (3.22)$$

Employing the periodic boundary condition, (3.22) becomes

$$\int_{\Omega} \frac{\partial w_j^i}{\partial y_l} \left(q^i \delta_{jl} - \frac{\partial u_j^i}{\partial y_l} \right) = -\int_{\Omega} w_j^i \delta_{ij}, \quad l = 1, 2, 3, \quad (3.23)$$

or

$$\int_{\Omega} -q^i \frac{\partial w_j^i}{\partial y_j} + \frac{\partial w_j^i}{\partial y_l} \frac{\partial u_j^i}{\partial y_l} = \int_{\Omega} w_j^i \delta_{ij}, \quad l = 1, 2, 3. \quad (3.24)$$

In the weak form, the problem becomes: Find $(\mathbf{u}^i, q^i) \in H(\Omega) \times L_0^2(\Omega)$ such that

$$-\int_{\Omega} (\nabla_y \cdot \mathbf{u}^i) Q^i dy = 0 \quad \text{for all } Q^i \in L_0^2(\Omega), \quad (3.25)$$

$$\int_{\Omega} \left(-q^i \nabla_y \cdot \mathbf{w}^i + \nabla_y \mathbf{u}^i : \nabla_y \mathbf{w}^i \right) dy = \int_{\Omega} \mathbf{e}^i \cdot \mathbf{w}^i dy, \quad \text{for all } \mathbf{w}^i \in H(\Omega), \quad (3.26)$$

where (3.25) and (3.26) come from (3.20) and (3.24), respectively. At this point, we drop the superscript i for convenience. Note that the weight functions belong to finite-dimensional subspaces of the space $H(\Omega) \times L_0^2(\Omega)$. Let $\Omega = \cup_{e=1}^J \Omega_e$, where Ω_e is a typical element [84]. In each element, u_j and q are approximated by:

$$u_j = \sum_{m=1}^M \psi_m(y) u_j^m = \begin{pmatrix} \psi_1 & \dots & \psi_M \end{pmatrix} \begin{pmatrix} u_j^1 \\ \vdots \\ u_j^M \end{pmatrix} = \mathbf{\Psi}^T \mathbf{u}_j, \quad (3.27)$$

$$q = \sum_{n=1}^N \phi_n(y) q_n = \begin{pmatrix} \phi_1 & \dots & \phi_N \end{pmatrix} \begin{pmatrix} q_1 \\ \vdots \\ q_N \end{pmatrix} = \mathbf{\Phi}^T \mathbf{Q}, \quad (3.28)$$

where $j = 1, 2, 3$; M and N are the numbers of nodes of the quadratic and linear functions, respectively, and ψ_m and ϕ_n are the interpolation functions.

Substituting both (3.27) and (3.28) into (3.20) and (3.24):

$$- \left[\int_{\Omega_e} \mathbf{\Phi} \frac{\partial \mathbf{\Psi}^T}{\partial y_l} dy \right] \mathbf{u}_l = 0, \quad (3.29)$$

$$- \left[\int_{\Omega_e} \frac{\partial \mathbf{\Psi}}{\partial y_j} \mathbf{\Phi}^T dy \right] \mathbf{Q} + \left[\int_{\Omega_e} \frac{\partial \mathbf{\Psi}}{\partial y_l} \frac{\partial \mathbf{\Psi}^T}{\partial y_l} dy \right] \mathbf{u}_j = \int_{\Omega_e} \mathbf{\Psi} \delta_{ij} dy, \quad (3.30)$$

we have j equations for each i with the summation under the repeat l . Another expression of (3.29) and (3.30) is

$$-\mathbf{D}_1 \mathbf{Q} + (\mathbf{E}_{11} + \mathbf{E}_{22} + \mathbf{E}_{33}) \mathbf{u}_1 = \mathbf{F}_{i1} \quad (3.31)$$

$$-\mathbf{D}_2 \mathbf{Q} + (\mathbf{E}_{11} + \mathbf{E}_{22} + \mathbf{E}_{33}) \mathbf{u}_2 = \mathbf{F}_{i2} \quad (3.32)$$

$$-\mathbf{D}_3 \mathbf{Q} + (\mathbf{E}_{11} + \mathbf{E}_{22} + \mathbf{E}_{33}) \mathbf{u}_3 = \mathbf{F}_{i3} \quad (3.33)$$

$$-\mathbf{D}^T_1 \mathbf{u}_1 - \mathbf{D}^T_2 \mathbf{u}_2 - \mathbf{D}^T_3 \mathbf{u}_3 = 0, \quad (3.34)$$

where superscript $(\cdot)^T$ denotes a transpose of the vector or matrix and

$$\mathbf{D}_j = \int_{\Omega_e} \frac{\partial \mathbf{\Psi}}{\partial y_j} \mathbf{\Phi}^T dy, \quad \mathbf{D}^T_j = \int_{\Omega_e} \mathbf{\Phi} \frac{\partial \mathbf{\Psi}^T}{\partial y_j} dy \quad (3.35)$$

$$\mathbf{E}_{ll} = \int_{\Omega_e} \frac{\partial \Psi}{\partial y_l} \frac{\partial \Psi^T}{\partial y_l} dy, \quad \mathbf{F}_{ij} = \int_{\Omega_e} \Psi \delta_{ij} dy, \quad (3.36)$$

where $\mathbf{F}_{ij} = \int_{\Omega_e} \Psi dy$ if $i = j$ and $\mathbf{F}_{ij} = 0$ if $i \neq j$. Rewriting (3.31)–(3.34) into an explicit matrix form

$$\begin{pmatrix} \mathbf{E} & 0 & 0 & -\mathbf{D}_1 \\ 0 & \mathbf{E} & 0 & -\mathbf{D}_2 \\ 0 & 0 & \mathbf{E} & -\mathbf{D}_3 \\ -\mathbf{D}_1^T & -\mathbf{D}_2^T & -\mathbf{D}_3^T & 0 \end{pmatrix} \begin{pmatrix} \mathbf{u}_1 \\ \mathbf{u}_2 \\ \mathbf{u}_3 \\ \mathbf{Q} \end{pmatrix} = \begin{pmatrix} \mathbf{F}_{i1} \\ \mathbf{F}_{i2} \\ \mathbf{F}_{i3} \\ 0 \end{pmatrix} \quad (3.37)$$

where $\mathbf{E} = \mathbf{E}_{11} + \mathbf{E}_{22} + \mathbf{E}_{33}$ and Ψ and Φ are defined as in (3.27) and (3.28). Another popular form of the matrix (3.37) in articles [1, 4] is

$$\begin{pmatrix} \mathbf{A} & -\mathbf{D} \\ -\mathbf{D}^T & \mathbf{0} \end{pmatrix} \begin{pmatrix} \mathbf{U} \\ \mathbf{Q} \end{pmatrix} = \begin{pmatrix} \mathbf{F} \\ \mathbf{0} \end{pmatrix} \quad (3.38)$$

where

$$\mathbf{U} = \begin{pmatrix} \mathbf{u}_1 \\ \mathbf{u}_2 \\ \mathbf{u}_3 \end{pmatrix} \quad \mathbf{D} = \begin{pmatrix} \mathbf{D}_1 \\ \mathbf{D}_2 \\ \mathbf{D}_3 \end{pmatrix} \quad \mathbf{F} = \begin{pmatrix} \mathbf{F}_{i1} \\ \mathbf{F}_{i2} \\ \mathbf{F}_{i3} \end{pmatrix} \quad \text{and} \quad \mathbf{A} = \begin{pmatrix} \mathbf{E} & 0 & 0 \\ 0 & \mathbf{E} & 0 \\ 0 & 0 & \mathbf{E} \end{pmatrix}. \quad (3.39)$$

It is well known that for Dirichlet conditions on \mathbf{u}^i the solution q is defined only up to an additive constant, which is usually fixed by imposing $\int_{\Omega} q = 0$, [[22], p.157 and [24], p.16]. Furthermore, in order to retain the symmetry of the matrix, we add one more column and row as following,

$$\begin{pmatrix} \mathbf{E} & -\mathbf{D} & \mathbf{0} \\ -\mathbf{D}^T & \mathbf{0} & \mathbf{1} \\ \mathbf{0} & \mathbf{1} & 0 \end{pmatrix} \begin{pmatrix} \mathbf{U} \\ \mathbf{Q} \\ \epsilon \end{pmatrix} = \begin{pmatrix} \mathbf{F} \\ \mathbf{0} \\ 0 \end{pmatrix} \quad (3.40)$$

where ϵ is very small after solving the matrix and the second order tensor is obtained from the formula (2.43). Moreover, the permeability can be verified by replacing ω_i in (2.39) by

\mathbf{u}^j and using the symmetric property of the permeability. Then

$$k_{ij} = \frac{1}{|\Omega|} \int_{\Omega_F} u_i^j dy = \frac{1}{|\Omega|} \int_{\Omega_F} \nabla \mathbf{u}^j : \nabla \mathbf{u}^i dy = \frac{\mu}{|\Omega|} (\mathbf{u}^j, \mathbf{u}^i)_H \quad (3.41)$$

is used as a consistency check with our numerical results k_{ij} from (2.43).

In order to ensure the Ladyzhenskaya-Babuska-Brezzi (LBB) consistency condition, we use the Taylor-Hood isoparametric 10-node tetrahedra, i.e. $M = 10$ and $N = 4$ for quadratic and linear functions, respectively. The discretization are generated by the open software Netgen [92]. A reference for three-dimensional finite element programming is Kwon and Bang [60] and other references on programming and implementing periodic boundary conditions can be found in [80] and [97].

3.3 Validation of Numerical Results

In case of a simple cubic array of spheres, Zick and Homsy [111] and H. Hasimoto [49] began with the slow flow as described by Stoke's equation, and found the periodic solutions analytically for the drag coefficient acting on a periodic array of small spheres. Thereafter, Rodrigo and Manuel [85] convert the drag coefficient to be permeability and compare their numerical results with the analytical ones. Since the permeability is calculated in this work, we compare our results with Rodrigo and Manuel [85]. In case of parallel cylinders, three-difference experimental data from previous publications [26, 98, 32] are chosen to validate our numerical results. Note that, the permeabilities from both experimental data and analytical results for each porosity were expressed as a scalar which was supposed to be given as a matrix because of the anisotropic medium. Therefore, to compare our solutions with the experimental data, we average the components of the numerical permeability tensor to compete with those facts in which the graphs are shown below.

To validate the code, the periodicity assumption is verified by calculating the permeability tensors using three different periodic cell arrays of cylinders. The smallest cell consists of 5 cylinders, see the figure in Table 3.1, with the radius $r = a/2 = 0.1$, $d = 0.3$ and the height $h = 0.5$. Then the dimension of the cell is $0.5 \times 0.5 \times 0.5$. The other two cells contain 13 and

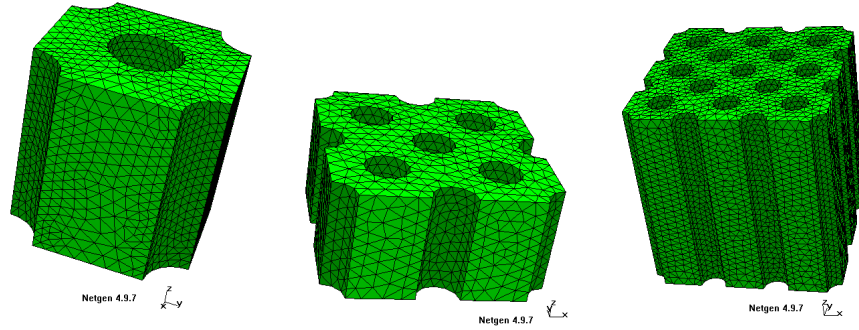
25 cylinders with the same radius r and the distance d as the smallest one. The dimension of the 13-cylinder cell is $1 \times 1 \times 1$ and that of the 25-cylinder cell is $1.5 \times 1.5 \times 1.5$. As is theoretically expected, the permeability tensors of the cells shown in Table 3.1 are the same for all of the different periodic REV's. Next we allowed the radii of the cylinders to increase almost to a point of touching so that Γ_F is almost not Lipschitz (but the domain is still a Lipschitz function). Figure 3.1 is a figure of Ω_F for this configuration and we see that the permeability:

$$\mathbf{k} = 1.0e - 04 * \begin{pmatrix} 0.0006 & 0.0000 & 0.0000 \\ 0.0000 & 0.0004 & 0.0000 \\ 0.0000 & 0.0000 & 0.1077 \end{pmatrix} \quad (3.42)$$

tends to zero for this geometry. The Figure presents a periodic cell with 5 cylinders while the radii of the cylinders at the center and corners are 0.1 and 0.249, respectively. Furthermore, if the ratio r/d (see Figure 1.3) is increased then the values of the permeability in every direction, $k_{ii}, i = 1, 2, 3$ decrease as expected, see Figure 3.2. Note that when the angle between the cylinders and horizontal plane is 90 degree, $k_{11} = k_{22}$. as we can see in3 Figure 3.2. Moreover, for each ratio r/d , the values of k_{33} are twice that of k_{11} or k_{22} . That is the resistance is doubled when the cylinders are orientated orthogonal to the flow direction. This observation was previously stated in the theoretical part of the paper by Jackson and James, [55]. This helps to avoid the numerical difficulty when the permeabilities of both geometries need to be provided. The effect of the angle of the cylinders makes with the base is provided in Figures 3.3, 3.4 and 3.5. In Figure 3.3, we show the diagonal entries of the permeability tensor for the case of distinct angles which can be used as coefficients in governing equations while Figures 3.4 and 3.5 show off-diagonal components of the tensor. Because \mathbf{k} is symmetric, only k_{12}, k_{13} and k_{23} are presented in Figures 3.4 and 3.5.

To further validate the calculation, we compare our results with those of Rocha and Cruz, 2009 [85], in which the geometry is a simple cubic array of spheres and the solutions are obtained numerically. The geometry of the periodic cubic cell Ω consists of a single

Table 3.1: Permeability through the cell array of cylinders at 90 degree of the different heights and periodic REVs providing the same permeability.



k		
0.0017	0.0000	0.0000
0.0000	0.0017	0.0000
0.0000	0.0000	0.0038

k denotes the permeability.

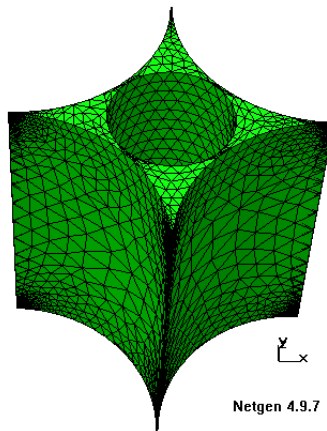


Figure 3.1: Permeability being close to zero of fluid flow through a cell array of cylinders when the boundary is almost not Lipschitz

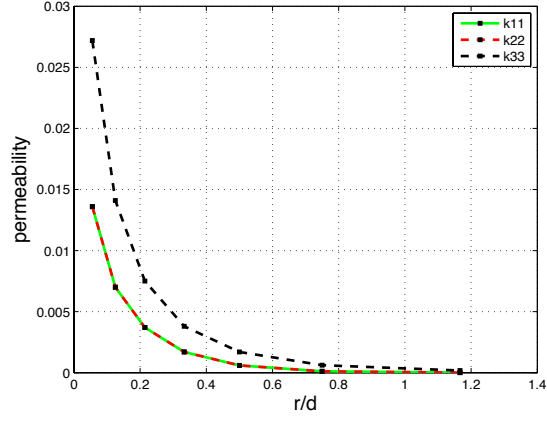


Figure 3.2: Permeability of fluid flow through a cell array of cylinders with increasing r/d , $\theta = 90^\circ$. Then $r/d = 1.2077$ is touching.

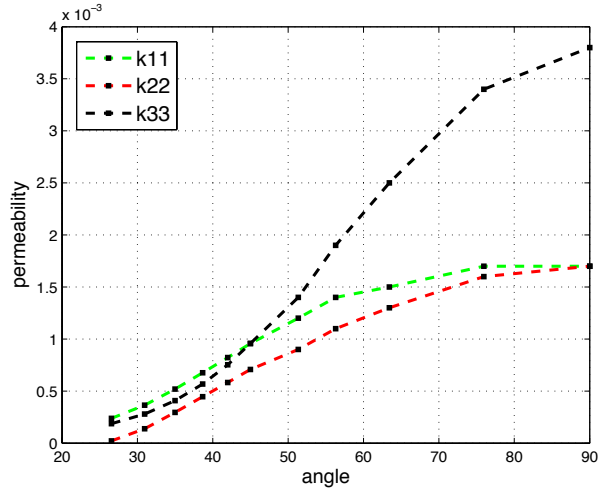


Figure 3.3: Diagonal values of the permeability tensor as a function of angle θ for r/d fixed at $1/3$.

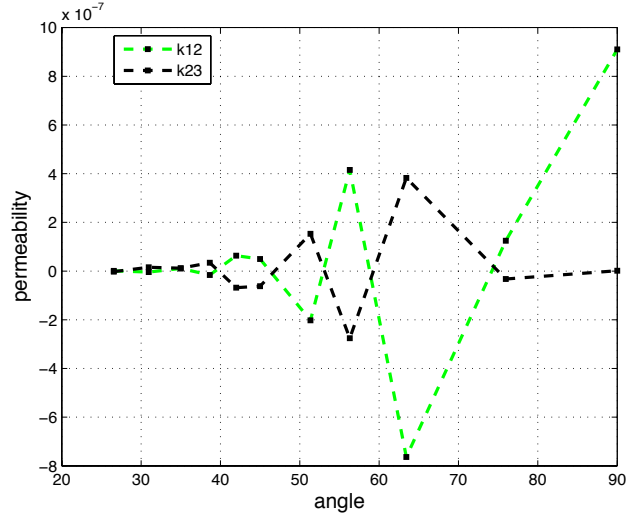


Figure 3.4: Off-diagonal values of the permeability tensor k_{12} and k_{23} as a function of angle θ for r/d fixed at $1/3$.

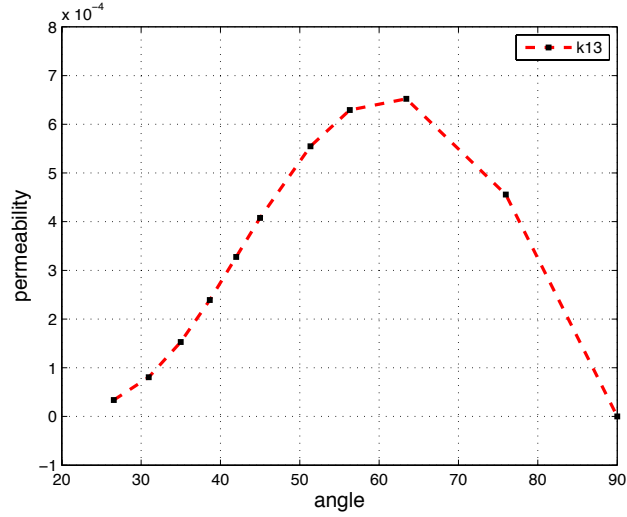
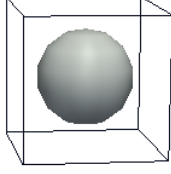


Figure 3.5: Off-diagonal values of the permeability tensor k_{13} as a function of angle θ for r/d fixed at $1/3$.

Table 3.2: Permeability through the simple cubic array of spheres with solid volume fraction $\epsilon^s = 0.216$ and radius = 0.5 unit; k_s denotes the permeabilities in this research; δk is the relative error of k_s with respect to k_{RM} which is the permeability calculating Rocha and Cruz (2009).



#dof	CPU time (sec)	k_s	$\delta k(\%)$
11,329	144.31	0.03519	1.793
81,470	16,804.78	0.03480	0.665
615,812	326,804.18	0.03463	0.173

sphere of unitary diameter at the center of Ω and has a cell length of $\{\pi/(6\epsilon^s)\}^{1/3}$, where ϵ^s is the volume fraction of the solid sphere. Because the sphere is isotropic, the permeability tensor is a scalar multiply of the identity, $k\mathbf{I}$. Table 3.2 shows the permeability for solid volume fraction $\epsilon^s = 0.216$. The variables k_s and $k_{RM} = 0.03457$ denote the permeabilities obtained in this research and by Rocha and Cruz (2009), respectively; δk is the relative error of k_s with respect to k_{RM} ; #dof is the number of degrees of freedom. Note that as the number of degrees of freedom, which in this case is the number of nodes used to calculate the velocities and pressure increases, the error decreases. With approximately 80,000 degrees of freedom, the relative error is less than 0.7% with CPU time about 4.6 hours. Although the error can be decreased to 0.173% more time is required -on the order 3.8 days. Different values of solid volume fraction are compared and the results are presented in Table 3.3. For $\epsilon^s = 0.125$, the relative error is smallest, 0.096%, but this case requires the larger number of degrees of freedom, 619,656. Although we didn't increase the number of degrees of freedom for the larger solid volume fractions, we see from Table 3.2 that the largest relative error is only 1%. The compared results are in a good agreement for a simple cubic array of spheres.

Next, we compare our results with two different sets of experimental data for an array of cylinders. One set of the data are from Sullivan [98] in which the flow is parallel to an array of cylinders and another set of data are from Brown [26] and Chen [32] in which the flow is perpendicular to the array of cylinders. Sullivan [98] presents experimental results

Table 3.3: Permeability through the simple cubic array of spheres with varying volume fraction of solid ϵ^s with radius 0.5 unit; k_s and k_{RM} denote the permeabilities in this research and by Rocha and Cruz (2009), respectively; δk is the relative error of k_s with respect to k_{RM} .

ϵ^s	k_s	k_{RM}	$\delta k(\%)$	#dof
0.125	0.1037	0.1036	0.096	619,656
0.216	0.03463	0.03457	0.173	615,812
0.343	0.01064	0.01052	1.140	81,660
0.450	0.004419	0.004398	0.477	78,740

for flow parallel to cylindrical fibers such as glass wool, blond and chinese hair, and goat wool. The data from Chen [32] are given in terms of the drag coefficient. For this reference we use (3.11) to find the permeabilities. Moreover, when the array of cylinders aligns parallel with the flow, the permeability is twice that of the perpendicular orientation, i.e. $2\mathbf{k}(\theta = \pi/2) = \mathbf{k}(\theta = \pi)$, [55]. Then, we only calculate our numerical results when the array of cylinders is perpendicular to the flow direction to avoid the mesh generation problems and compare the results with the experimental data. Figure 3.6 showing the plots of our numerical results $2k_{33}$ and $2(k_{11} + k_{22})$ and experimental data from Sullivan [98] displays the harmonization. Similarly, when $\theta = \pi/2$, the data from Brown [26] and Chen [32] are compared with our numerical results in Figure 3.7. The data compare well with k_{33} and $k_{11} + k_{22}$. Note that the data from Chen oscillate because he collected data from several publications.

3.4 Numerical Permeability Functions

In this section, we provide polynomial approximation of each entry of the permeability tensor as a function of the distance between the cylinders, the radius of the cylinder and the angle the cylinders make with the base. Figure 3.8 illustrates the idea of how the permeability varies with the geometry. The top left graph presents the numerical permeability in the

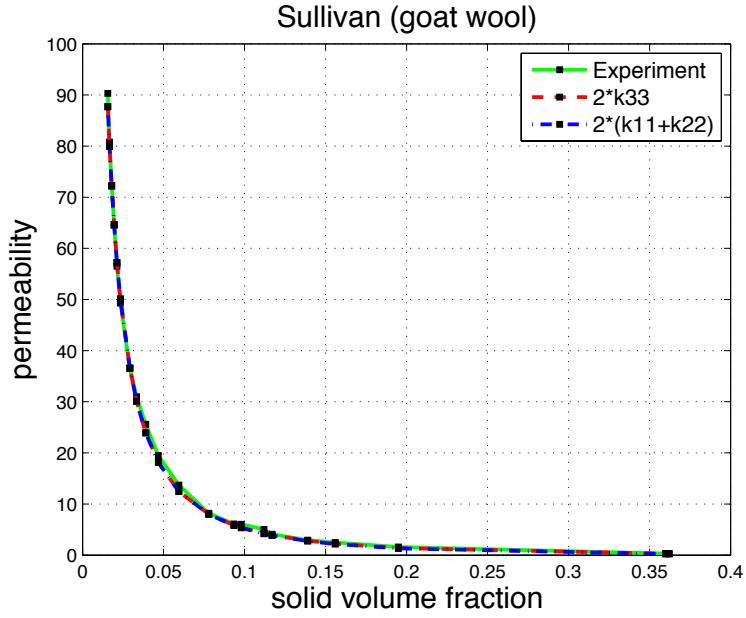
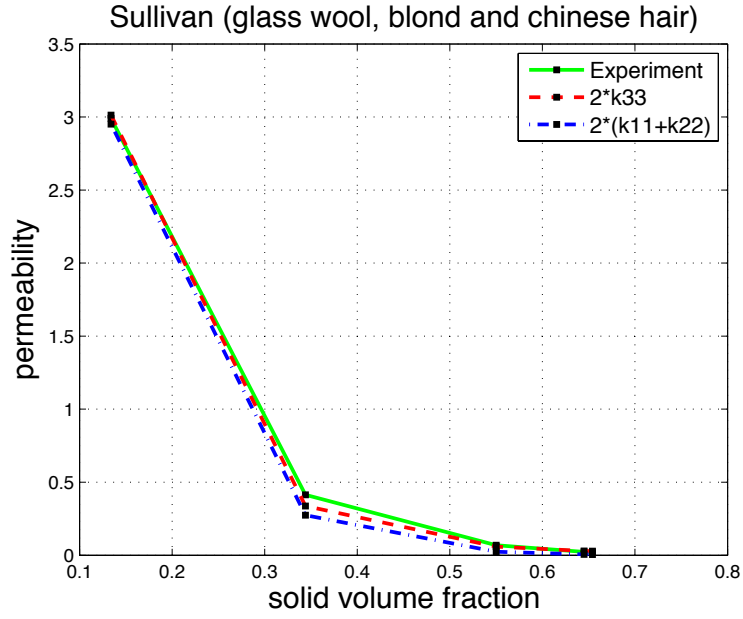


Figure 3.6: Permeability of fluid flow through a periodic array of cylinders for $\theta = 0$. When the flow aligns parallel to the cylinders, figures show the experimental scalar permeabilities of Sullivan for hairs and goat wool, respectively, comparing with our numerical $2 * k_{33}$ and $2 * (k_{11} + k_{22})$ results for $\theta = \pi/2$.

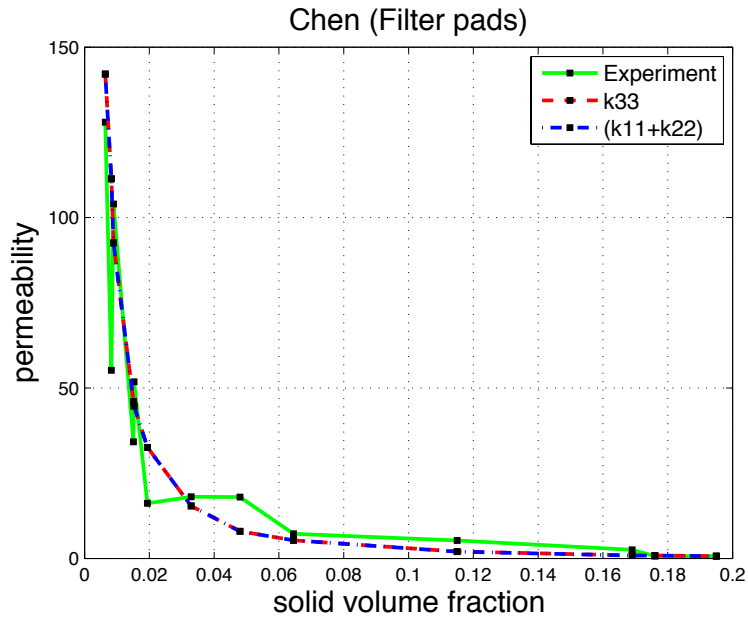
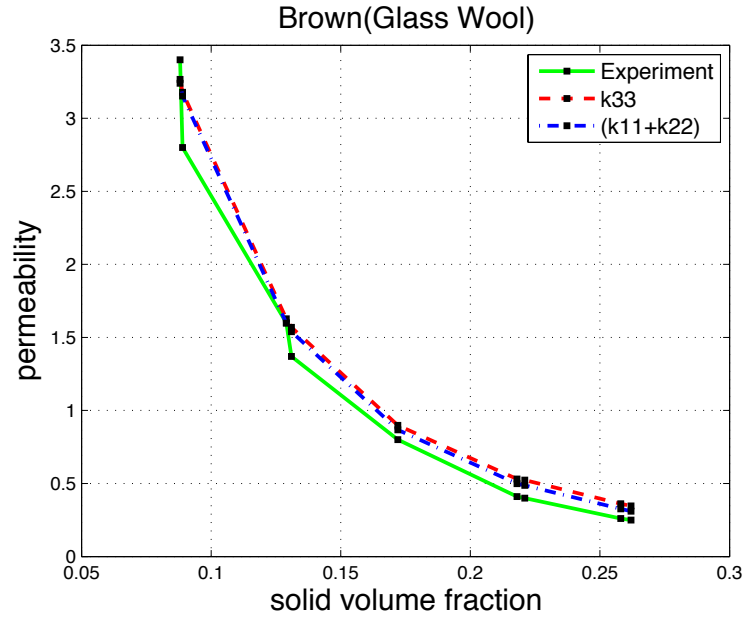


Figure 3.7: Permeability of fluid flow through a cell array of cylinders. Figures are comparing the experimental data of Brown and Chen with our numerical k_{33} and $k_{11} + k_{22}$ when the flow is perpendicular to the array of cylinders.

direction x or k_{11} as a function of the dimensionless quotient between the radius of a cylinder, r , and the distance between them, d (x -axis); and the angle θ (y -axis) between cylinders and the horizontal plane defined in Figure 1.3. The variable r takes on values between 0.025 and 0.125 and the angle θ takes on values between 26 to 90 degrees.

Next, we approximate each permeability component by a fourth-order polynomial of the form $a_1x^4 + a_2x^3y + a_3x^3 + a_4x^2y^2 + a_5x^2y + a_6x^2 + a_7xy^3 + a_8xy^2 + a_9xy + a_{10}x + a_{11}y^4 + a_{12}y^3 + a_{13}y^2 + a_{14}y + a_{15}$, where the coefficients $a_i, i = 1, 2, \dots, 15$ are provided in Tables 3.4 and 3.5. For the right top of Figure 3.8, we estimate the numerical permeability tensor using the fourth-order polynomials. The absolute errors and the two-norm are expressed on the bottom one. Similar graphs can be obtained for the other components. Figures 3.9 and 3.10 show the numerically generated graphs of the diagonal components k_{22} and k_{33} and the off-diagonal components k_{12} , k_{13} and k_{23} , respectively. The L2-norm for the difference between the numerical results and polynomial approximations for each component is presented in Table 3.6.

3.5 Comparison with Kozeny-Carman Equation

The Kozeny-Carman is a famous equation which can indicate an empirical relationship between the porosity and the isotropic, scalar, permeability [28],

$$k = \frac{(\epsilon^l)^3 g}{k_1 S^2}, \quad (3.43)$$

from the relationship between the superficial velocity and the pressure gradient

$$v_s = \frac{(\epsilon^l)^3 g}{k_1 \mu S^2} \frac{\Delta p}{l}, \quad (3.44)$$

where k_1 is a constant depending on the geometry; S is an area of particular surface per unit volume of packed space, $[S] = [1/L]$. Because this expression has been widely used [15, 27, 35], we compare our numerical results with this relationship, even though the isotropy assumption for an array of parallel cylinders is clearly not valid. For the parallel cylinders,

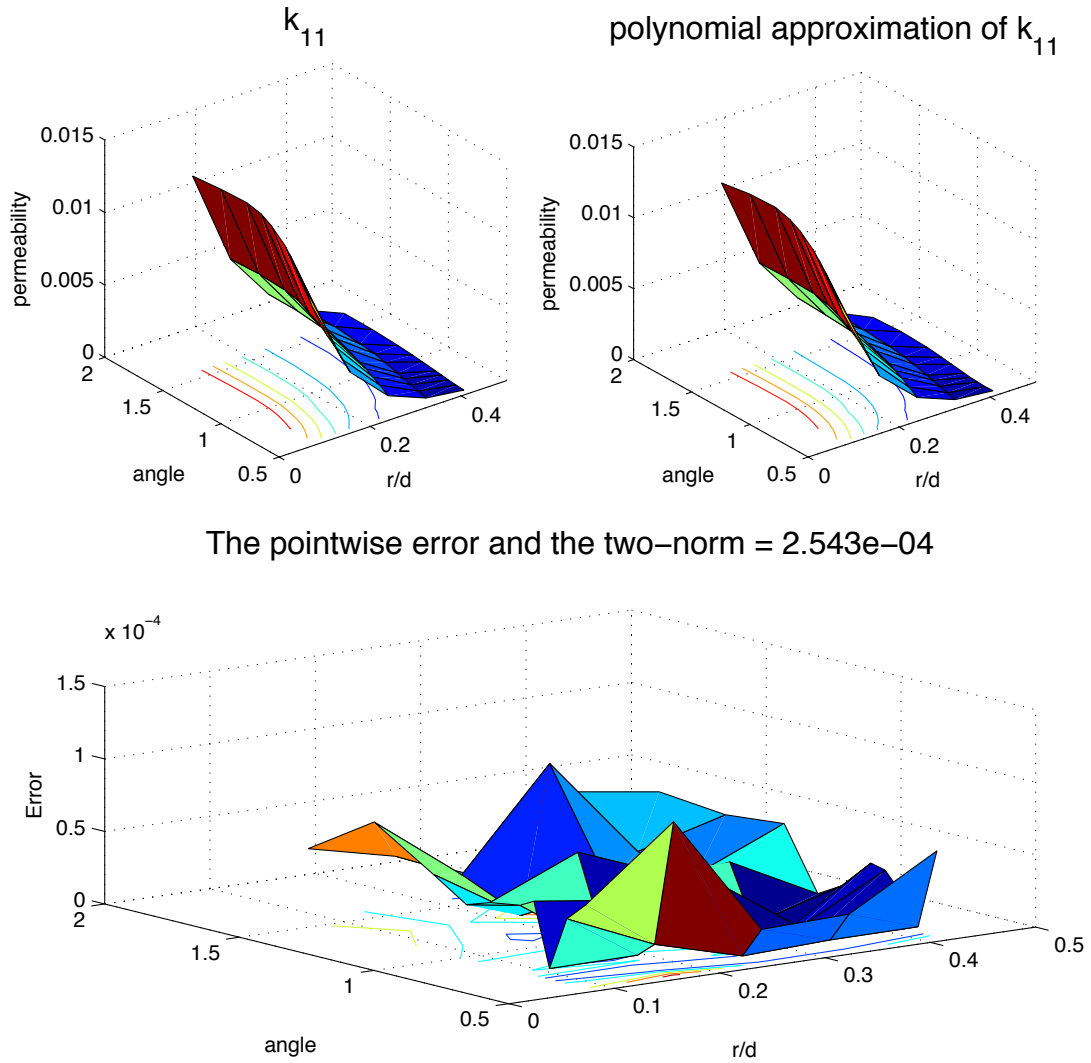


Figure 3.8: The top left graph is the numerically generated permeability component k_{11} while the top right one is the fourth-order polynomial approximation of the top left graph; the pointwise absolute error are shown at the bottom.

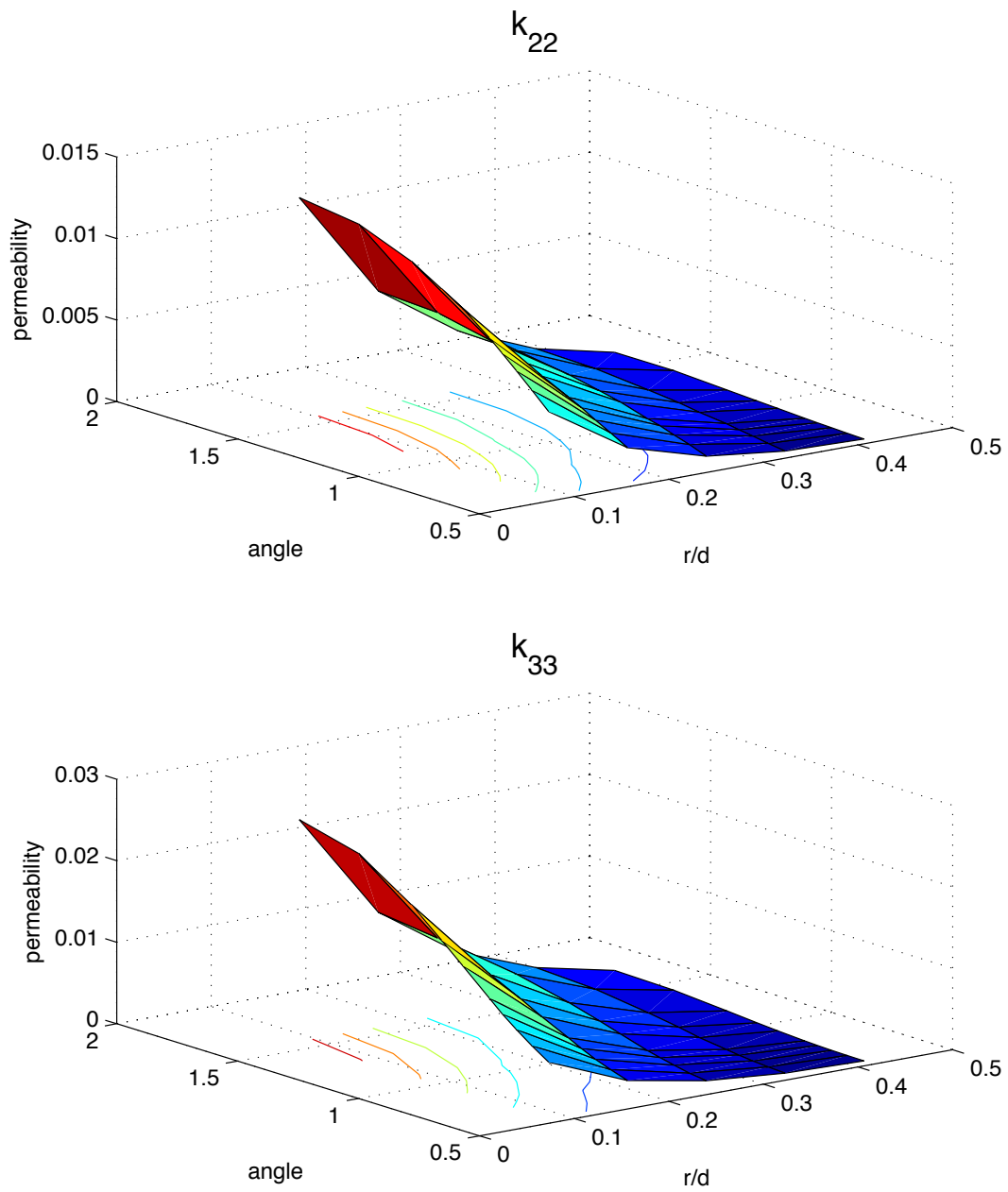


Figure 3.9: The diagonal components k_{22} and k_{33} of the permeability tensor

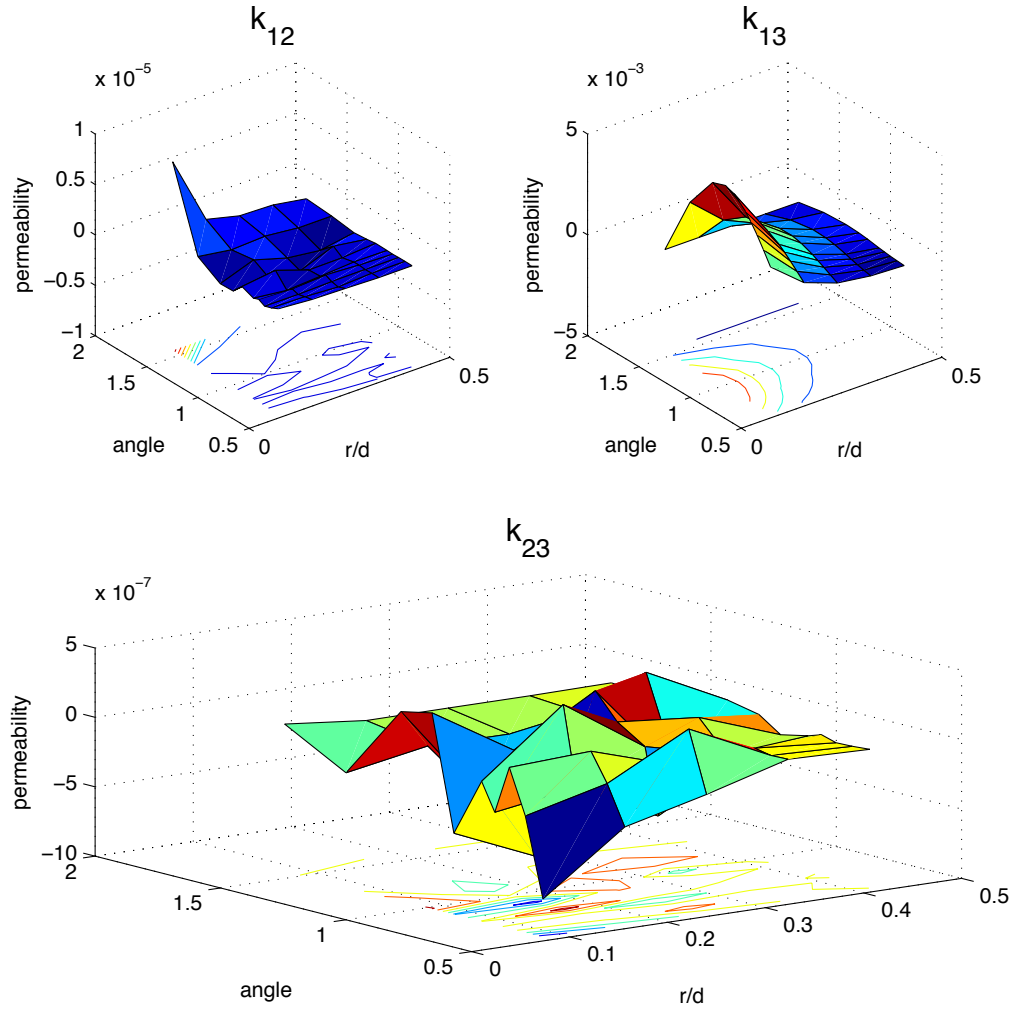


Figure 3.10: The off-diagonal components k_{12} , k_{13} and k_{23} of the permeability tensor.

Table 3.4: The fourth-order polynomial functions: $a_1x^4 + a_2x^3y + a_3x^3 + a_4x^2y^2 + a_5x^2y + a_6x^2 + a_7xy^3 + a_8xy^2 + a_9xy + a_{10}x + a_{11}y^4 + a_{12}y^3 + a_{13}y^2 + a_{14}y + a_{15}$ approximating k_{11} , k_{22} and k_{33} .

Coefficients	k_{11}	k_{22}	k_{33}
a_1	$1.0198e + 000$	$984.1116e - 003$	$1.3062e + 000$
a_2	$-255.7726e - 006$	$-2.5282e - 003$	$-8.1104e - 003$
a_3	$-1.3507e + 000$	$-1.0963e + 000$	$-1.2944e + 000$
a_4	$-18.5001e - 006$	$-12.9402e - 006$	$-24.0304e - 006$
a_5	$2.4220e - 003$	$4.4395e - 003$	$11.9560e - 003$
a_6	$671.5718e - 003$	$425.4400e - 003$	$365.6415e - 003$
a_7	$-151.3900e - 009$	$3.2985e - 009$	$279.1924e - 009$
a_8	$44.3630e - 006$	$12.5010e - 006$	$-29.5497e - 006$
a_9	$-3.8002e - 003$	$-2.8409e - 003$	$-3.4598e - 003$
a_{10}	$-112.1466e - 003$	$-50.8733e - 003$	$-34.9274e - 003$
a_{11}	$258.6547e - 012$	$-2.4185e - 012$	$176.7506e - 012$
a_{12}	$-10.3378e - 009$	$-5.9015e - 009$	$-170.4837e - 009$
a_{13}	$-8.0786e - 006$	$-2.1735e - 006$	$22.2997e - 006$
a_{14}	$905.0796e - 006$	$566.7804e - 006$	$-274.0899e - 006$
a_{15}	$804.5324e - 006$	$-2.7328e - 003$	$8.2408e - 003$

where $a_i, i = 1, 2, \dots, 15$ are the coefficients; $x = r/d$; $y = \theta$ which is defined in Figure 1.3;

$r \in [0.025, 0.125]$ and $\theta \in [\arctan(0.5), \arctan(\infty)]$, about 26 to 90 degree.

Table 3.5: The fourth-order polynomial functions: $a_1x^4 + a_2x^3y + a_3x^3 + a_4x^2y^2 + a_5x^2y + a_6x^2 + a_7xy^3 + a_8xy^2 + a_9xy + a_{10}x + a_{11}y^4 + a_{12}y^3 + a_{13}y^2 + a_{14}y + a_{15}$ approximating k_{12} , k_{13} and k_{23} .

Coefficients	k_{12}	k_{13}	k_{23}
a_1	$-499.8635e - 006$	$297.6621e - 003$	$428.9162e - 006$
a_2	$-9.2789e - 006$	$1.2256e - 003$	$-1.4217e - 006$
a_3	$933.9637e - 006$	$-459.2711e - 003$	$-371.3372e - 006$
a_4	$80.3350e - 009$	$-36.4347e - 006$	$-5.9070e - 009$
a_5	$-1.1085e - 006$	$2.9797e - 003$	$1.9071e - 006$
a_6	$-305.3777e - 006$	$167.6087e - 003$	$76.7183e - 006$
a_7	$-393.8843e - 012$	$-10.4710e - 009$	$-78.2267e - 012$
a_8	$18.3621e - 009$	$31.5771e - 006$	$17.8581e - 009$
a_9	$-251.6399e - 009$	$-3.1336e - 003$	$-1.5587e - 006$
a_{10}	$39.8263e - 006$	$11.6868e - 003$	$20.6851e - 006$
a_{11}	$754.8963e - 015$	$580.3406e - 012$	$16.5870e - 015$
a_{12}	$-33.8628e - 012$	$-140.4834e - 009$	$21.7867e - 012$
a_{13}	$-2.2598e - 009$	$5.7977e - 006$	$-4.9221e - 009$
a_{14}	$147.4440e - 009$	$251.2534e - 006$	$349.0144e - 009$
a_{15}	$-3.5492e - 006$	$-4.1563e - 003$	$-6.8813e - 006$

where $a_i, i = 1, 2, \dots, 15$ are the coefficients; $x = r/d$; $y = \theta$ which is defined in Figure 1.3;

$r \in [0.025, 0.125]$ and $\theta \in [\arctan(0.5), \arctan(\infty)]$, about 26 to 90 degree.

Table 3.6: L2-norm errors of the components of the permeability \mathbf{k}

components	L2-norm error
k_{11}	$2.54e - 04$
k_{22}	$1.32e - 04$
k_{33}	$2.48e - 04$
k_{12}	$2.25e - 06$
k_{13}	$2.11e - 04$
k_{23}	$1.10e - 06$

there is a one-to-one relationship between the angle and porosity that can be determined analytically.

Most applications are using the porosity to implement to their problems as a primary variable to find the dependent value of the permeability. Kozeny-Carman equation indicating the relationship between velocity and gradient of pressure provides a specific form of the permeability. Geoscience communities sometime use this equation to calculate the permeability for their porous media problems. Therefore, in this section, a formula of the permeability functions associated with the Kozeny-Carman equation are expressed and compared with our numerical solutions.

To derive the formula of the permeability using Kozeny-Carman equation, it is necessary to know the volume of the cylinders changed depending on the angle that the parallel array of cylinders makes with the horizontal plane in the periodic cell. Figure 3.11, on the left, shows the cell array of cylinders with each cell consisting of 2 ellipsoidal cylinders: one in the middle and another one from the sides after bonding them together. The volume is used to determine the total volume of the cell which is applied to attain the variable S in the

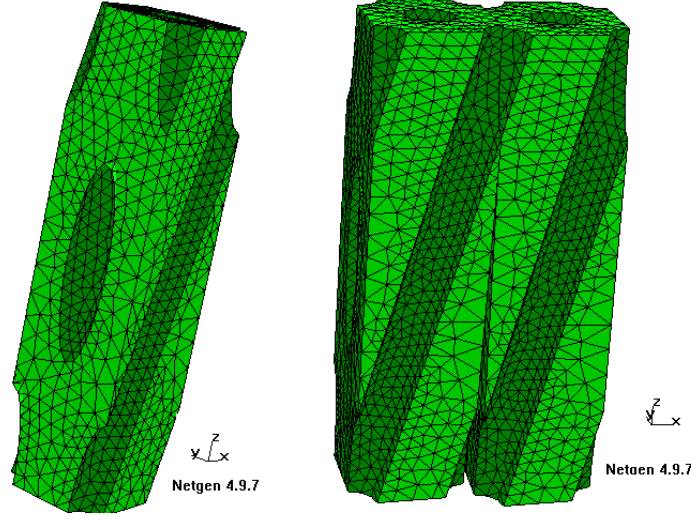


Figure 3.11: Geometry: the left figure shows the cell array of cylinders when the angle between the cylinders and horizontal plane is 75 degrees; the right one shows each cell consists of 2 ellipsoidal cylinders.

formula (3.43):

$$k = \frac{(\epsilon^l)^3 g}{k_1 S^2} = C_k \frac{(\epsilon^l)^3}{S^2}, \quad (3.45)$$

where $C_k = g/k_1$ is a constant and

$$S = \frac{\text{surface area of solid staying in fluid phase}}{\text{total volume of the cell}} = \frac{S_A}{V_t}. \quad (3.46)$$

Because the surface area of an ellipsoidal cylinder is

$$(\text{perimeter of shape A})L + 2(\text{area of shape A}), \quad (3.47)$$

where the length of the cylinder L and the cross-sectional area A are defined in Figure 3.12 and the fluid is past only on the side of the ellipsoidal cylinders.

$$S_A = 2L (\text{perimeter of shape A}), \quad (3.48)$$

where only two ellipsoidal cylinders are in the cell. For the perimeter of an ellipse, there are many formulas can be used. In this work, we employ only two different ones:

$$\pi \left[3(r + r_1) - \sqrt{(3r + r_1)(r + 3r_1)} \right], \quad (3.49)$$

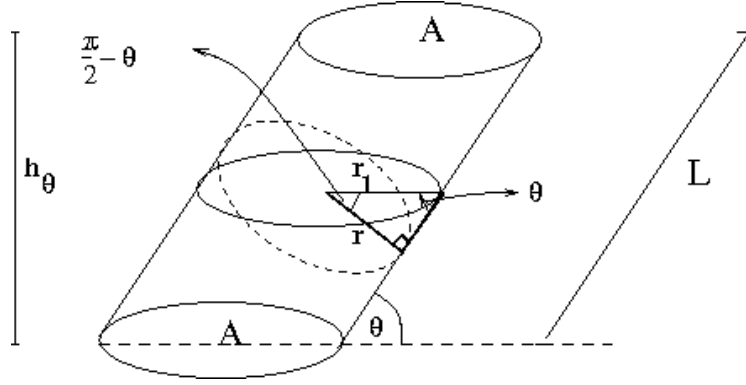


Figure 3.12: Figure shows the radii of an ellipse in both major and minor axes and θ is the angle between the horizontal plane and the side of the cylinder while h_θ is the height of the periodic cell which is perpendicular to the horizontal plane.

and

$$2\pi\sqrt{\frac{r^2 + r_1^2}{2}}, \quad (3.50)$$

where r and r_1 are the radii of the ellipse A , defined in Figure 3.12 and r also the radius of the cylinder. The equation (3.50) is simpler but r_1 should not more than three times longer than r . However, equation (3.49) presented by Indian mathematician Ramanujan provides better approximation. Substituting (3.49) into (3.48), we have

$$S_A = 2\pi L \left[3(r + r_1) - \sqrt{(3r + r_1)(r + 3r_1)} \right] \quad (3.51)$$

while the second formula gives

$$S_A = 4\pi L \sqrt{\frac{r^2 + r_1^2}{2}}. \quad (3.52)$$

From Figure 3.12, it's obvious that the radius of the ellipse

$$r_1 = \frac{r}{\sin\theta} \quad \text{and} \quad L = \frac{h_\theta}{\sin\theta}. \quad (3.53)$$

Therefore the volume of the 2 cylinders in the cell is

$$V_s = 2\pi r r_1 h_\theta = \frac{2\pi}{\sin\theta} r^2 h_\theta \quad (3.54)$$

where h_θ is the height of the cell which is a function of the angle θ , defined in Figure 3.12.

Hence, the total volume of the periodic cell

$$V_t = \frac{V_s}{V_s/V_t} = \frac{V_s}{\epsilon^s} = \frac{V_s}{1 - \epsilon^l} = \frac{2\pi}{\sin\theta(1 - \epsilon^l)} r^2 h_\theta, \quad (3.55)$$

where ϵ^l and ϵ^s are fluid and solid volume fractions, respectively. Substituting (3.51), (3.53), and (3.55) into (3.46), we have

$$S = \frac{(2\pi h_\theta / \sin\theta) \left[3(r + r_1) - \sqrt{(3r + r_1)(r + 3r_1)} \right]}{(2\pi r^2 h_\theta / \sin\theta (1 - \epsilon^l))} \quad (3.56)$$

$$= \frac{1 - \epsilon^l}{r^2} \left[3 \left(r + \frac{r}{\sin\theta} \right) - \sqrt{\left(3r + \frac{r}{\sin\theta} \right) \left(r + 3 \frac{r}{\sin\theta} \right)} \right] \quad (3.57)$$

$$= \frac{(1 - \epsilon^l)}{r \sin\theta} \left[3(\sin\theta + 1) - \sqrt{(3\sin\theta + 1)(\sin\theta + 3)} \right] \quad (3.58)$$

Substituting (3.58) into (3.45), we have

$$k = C_k \frac{(\epsilon^l)^3 r^2 \sin^2\theta}{(1 - \epsilon^l)^2 \left[3(\sin\theta + 1) - \sqrt{(3\sin\theta + 1)(\sin\theta + 3)} \right]^2}. \quad (3.59)$$

Similar process is applied to (3.52). Then

$$S = \frac{(4\pi h_\theta / \sin\theta) \sqrt{(r^2 + (\frac{r}{\sin\theta})^2)/2}}{(2\pi / \sin\theta (1 - \epsilon^l)) r^2 h_\theta} = \frac{\sqrt{2}(1 - \epsilon^l)}{r \sin\theta} \sqrt{\sin^2\theta + 1} \quad (3.60)$$

Substituting (3.60) into (3.45), we have

$$k_1 = C_{k1} \frac{(\epsilon^l)^3 r^2 \sin^2\theta}{2(\sin^2\theta + 1)(1 - \epsilon^l)^2} \quad (3.61)$$

where C_{k1} is a constant. Next, we apply the curve fitting method to fit the best curve to the numerical data. Least-squares regression is one technique to accomplish this objective.

In this work, the curve fitting method from Matlab is used to determine the constant in the linear relationship between the numerical results and the formula 3.59 or 3.61. With small adjustment in the denominator, we have the permeability

$$\frac{1}{3} \text{tr}(\mathbf{k}) = k = 1.6147 \frac{(\epsilon^l)^3 r^2 \sin^2\theta}{(1 - \epsilon^l + 0.6)^2 \left[3(\sin\theta + 1) - \sqrt{(3\sin\theta + 1)(\sin\theta + 3)} \right]^2} + 10^{-4} \quad (3.62)$$

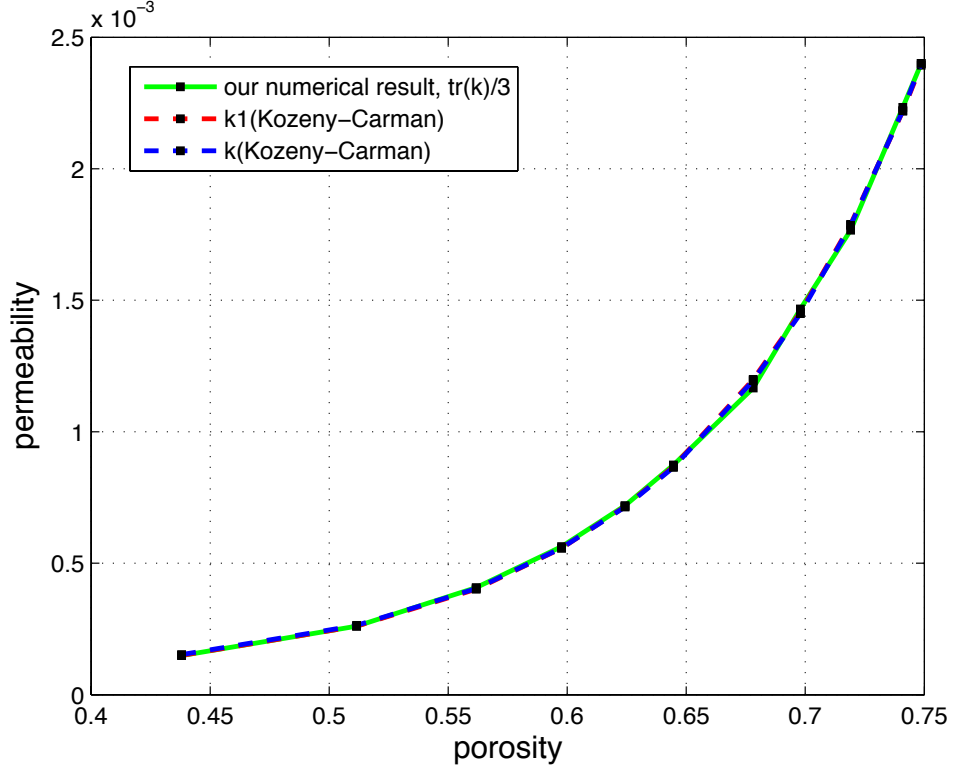


Figure 3.13: The green line represents the the spherical part of the permeability tensor of the numerical result while the blue and red ones are from the functions (3.62) and (3.63), respectively, where x-axis is the porosity depending on each angle.

and

$$\frac{1}{3}\text{tr}(\mathbf{k}) = k_1 = \frac{(\epsilon^l)^3 g}{k_1 S^2} = \text{constant} \frac{(\epsilon^l)^3}{S^2} = \frac{2.0128 (\epsilon^l)^3 r^2 \sin^2 \theta}{2(1 - \epsilon^l + 0.7)^2 (\sin^2 \theta + 1)} + 10^{-4}, \quad (3.63)$$

which are shown in Figure 3.13 when the radius r of the cylinders is 0.1. As we can see there is excellent agreement between the Kozeny-Carman expression and 1/3 trace of the permeability.

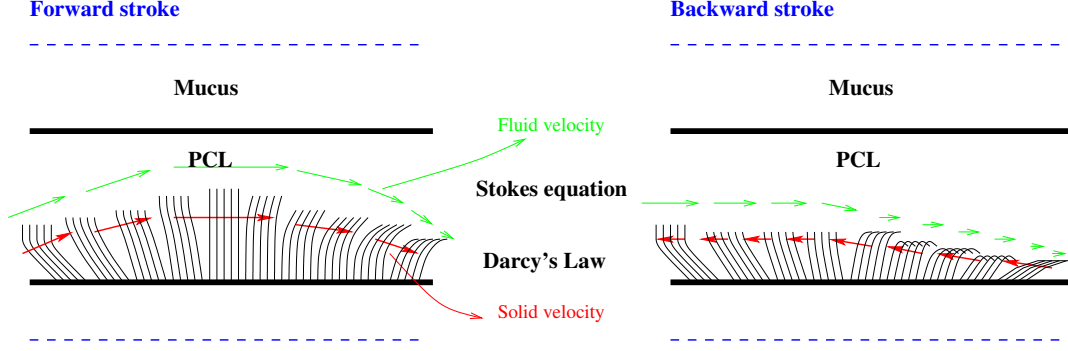


Figure 4.1: The cartoon picture is showing the fixed boundary while the cilia is moving forward and backward making the angle θ with the horizontal plane in the PCL.

4. MODELING THE PCL

The purpose of this Chapter is to develop the governing equations that will be used to model the PCL, the layer containing both cilia and a low viscosity fluid. We assume the PCL height is fixed and consider a two-dimensional domain. Figure 4.1 illustrates the fixed height PCL and mucous layer. The red arrows indicate the cilia beating backward and forward generating metachronal waves that propel the mucus out of the lung while the green arrows demonstrate the fluid flow in the PCL. For all angles except the ones close to 90° , there is a layer of PCL fluid between the tip of the cilia and the mucous layer.

Note that the densities of the PCL fluid and the mucus are different. If the difference in densities of the contiguous fluids is large, the free boundary, an interface whose location is a priori unknown, occurs at the PCL/mucus interface and modeling this will be discussed in Chapter 6. At present we assume that the PCL height is fixed.

In this model, we decompose the PCL into two domains, Ω_1 and Ω_2 . The domain Ω_1 is defined to be the region that has no cilia while Ω_2 consists of cilia, see Figure 1.2. Because Ω_1 is not a porous medium, there is no permeability tensor in this region. In Ω_2 , the permeability has a finite value. Typically, the Stokes or Navier-Stokes equations are used in Ω_1 and Darcy's Law with the Beavers-Joseph condition in Ω_2 , [3, 47, 62]. In this study, we

use the Stokes-Brinkman equations which are employed by several authors, [57, 67, 68, 75].

Next, we briefly clarify the difference between Darcy's Law and the Brinkman equation and why the Brinkman equation is employed for this problem. Darcy's law is typically employed where viscosity and inertial effects are negligible, and where the fluid flowing through the porous media is considered slow. Darcy's Law [37] is

$$\mathbf{v}_D = -\frac{\mathbf{k}}{\mu} [\nabla p - \rho \mathbf{g}], \quad (4.1)$$

where \mathbf{v}_D is Darcy's velocity; ρ is the fluid density and \mathbf{g} is the gravity. Brinkman [25] claimed that in some cases the viscous shearing stresses acting on the fluid in Darcy's law are not negligible so that an additional term should be included. To rigorously determine the form of Darcy's Law incorporating viscous sheering stress, we use Hybrid Mixture Theory (HMT), [10, 12, 36, 103], and nondimensionalization to obtain form of the Brinkman equation, see Section 4.4:

$$\mu \mathbf{k}^{-1} \cdot (\epsilon^l \mathbf{v}^l - \epsilon^l \mathbf{v}^s) + \nabla p - \frac{\mu}{\epsilon^l} \nabla \cdot (2\epsilon^l \mathbf{d}^l) = \rho \mathbf{g}, \quad (4.2)$$

which is the equation used in domain Ω_2 . For the divergent-free continuity equation, (4.2) is consistent with equation (61) in [106] except that (4.2) includes the term, $\epsilon^l \mathbf{v}^s$, on the left-hand side whereas in [106] it is assumed the velocity of the solid phase is zero. The term $(\mu/\epsilon^l) \nabla \cdot (2\epsilon^l \mathbf{d}^l)$ comes from the liquid phase stress tensor and with this term the generalized Darcy's Law is called the Brinkman equation. This extra term helps to match the tangential stress acting on the fluid at the free-fluid/porous-medium interface.

To see the connection with the Stokes equation, if we let \mathbf{k}^{-1} go to zero in domain Ω_1 , (4.2) can be rewritten as

$$\nabla p - \frac{\mu}{\epsilon^l} \nabla \cdot (2\epsilon^l \mathbf{d}^l) = \rho \mathbf{g}. \quad (4.3)$$

If ϵ^l is a constant in space, we have

$$\nabla \cdot (2\epsilon^l \mathbf{d}^l) = \epsilon^l (v_{i,j}^l + v_{j,i}^l)_{,j} = \epsilon^l (v_{i,jj}^l + v_{j,ij}^l) = \Delta(\epsilon^l \mathbf{v}^l) + \epsilon^l \nabla(\nabla \cdot \mathbf{v}^l). \quad (4.4)$$

Since we assume that the fluid is incompressible,

$$\nabla \cdot \mathbf{v}^l = 0 \quad (4.5)$$

in domain Ω_1 . Therefore (4.3) becomes

$$\nabla p - \rho \mathbf{g} = \frac{\mu}{\epsilon^l} \Delta(\epsilon^l \mathbf{v}^l), \quad (4.6)$$

which is the Stokes equation. The typical derivation of the Stokes equation is shown in Section 4.5 by beginning with the Navier-Stokes equation with the porosity $\epsilon^l = 1$.

Coupling the Brinkman equation (4.2) with the continuity equation gives [104]

$$\dot{\epsilon}^l + (1 - \epsilon^l) \nabla \cdot (\epsilon^l (\mathbf{v}^l - \mathbf{v}^s)) = 0, \quad (4.7)$$

and we now have the system of equations in the porous medium domain Ω_2 , while (4.5) and (4.6) are the equations in Ω_1 . Equation (4.7) is derived in Section 4.2, where $\dot{\epsilon}^l$ is the material time derivative of the porosity with respect to the solid phase, $\dot{\epsilon}^l = \partial \epsilon^l / \partial t + \mathbf{v}^s \cdot \nabla \epsilon^l$. In Section 4.1, we derive the general form of the macroscale momentum equation by averaging. The continuity equation (4.7) is derived in Section 4.2. Darcy's Law and the Brinkman equation which are specific forms of the momentum equation, are derived in Sections 4.3 and 4.4, respectively. The Stokes equation is developed in Section 4.5. Finally, the well-posedness of the Stokes-Brinkman system of equations is shown in Section 4.6 for a second-order permeability tensor. Previously this had been shown only for a scalar coefficient.

4.1 General Form of the Momentum Equations using HMT

Hybrid Mixture Theory (HMT) uses averaging theorem to derive macroscopic field equations and then exploits the entropy inequality to derive constitutive equations. To transfer a microscale variable to a macroscale variable is defined in term of the intrinsic phase average. That is the average of the microscale variable weighted by the volume of the phase. In this section, we briefly describe the derivation of the macroscale conservation of mass and momentum balances for each phase using HMT [9, 12, 74, 103]. We start with the conservation

of mass at the microscale,

$$\frac{\partial \rho}{\partial t} + \nabla \cdot \rho \mathbf{v} = 0. \quad (4.8)$$

Define the indicator function

$$\gamma_\alpha(\mathbf{r}, t) = \begin{cases} 1 & \text{if } \mathbf{r} \in \delta V_\alpha \\ 0 & \text{if } \mathbf{r} \in \delta V_\beta, \beta \neq \alpha, \end{cases} \quad (4.9)$$

and δV as the representative elementary volume (REV) [6], and δV_α denotes the portion of δV in the α -phase and δV_β is the portion of δV in the β -phase. Multiplying (4.8) by γ_α , integrating (4.8) with respect to δV and dividing by the volume $|\delta V|$, we have

$$\frac{1}{|\delta V|} \int_{\delta V} \frac{\partial \rho}{\partial t} \gamma_\alpha dv + \frac{1}{|\delta V|} \int_{\delta V} \nabla \cdot (\rho \mathbf{v}) \gamma_\alpha dv = 0, \quad (4.10)$$

The averaging theorem [12, 38] tells us how to interchange the partial derivatives and the integral,

$$\frac{1}{|\delta V|} \int_{\delta V} \frac{\partial f}{\partial t} \gamma_\alpha dv(\xi) = \frac{\partial}{\partial t} \left[\frac{1}{|\delta V|} \int_{\delta V} f \gamma_\alpha dv(\xi) \right] - \sum_{\beta \neq \alpha} \frac{1}{|\delta V|} \int_{\delta A_{\alpha\beta}} f \mathbf{w}_{\alpha\beta} \cdot \mathbf{n}_\alpha da(\xi) \quad (4.11)$$

$$\frac{1}{|\delta V|} \int_{\delta V} \nabla_{\mathbf{x}} f \gamma_\alpha dv(\xi) = \nabla_{\mathbf{x}} \left[\frac{1}{|\delta V|} \int_{\delta V} f \gamma_\alpha dv(\xi) \right] + \sum_{\beta \neq \alpha} \frac{1}{|\delta V|} \int_{\delta A_{\alpha\beta}} f \mathbf{n}_\alpha da(\xi), \quad (4.12)$$

where f is the quantities in the field equations, and $\delta A_{\alpha\beta}$, $\mathbf{w}_{\alpha\beta}$ and \mathbf{n}_α are the portion of the $\alpha\beta$ interface within δV , the microscopic velocity of interface $\alpha\beta$, and the outward unit normal vector to δV_α , respectively. Applying the theorem to each term in (4.10) gives

$$\frac{1}{|\delta V|} \int_{\delta V} \frac{\partial \rho}{\partial t} \gamma_\alpha dv = \frac{\partial}{\partial t} \left[\frac{1}{|\delta V|} \int_{\delta V} \rho \gamma_\alpha dv \right] - \sum_{\beta \neq \alpha} \frac{1}{|\delta V|} \int_{\delta A_{\alpha\beta}} \rho \mathbf{w}_{\alpha\beta} \cdot \mathbf{n}_\alpha da, \quad (4.13)$$

$$\frac{1}{|\delta V|} \int_{\delta V} \nabla \cdot (\rho \mathbf{v}) \gamma_\alpha dv = \nabla \cdot \left[\frac{1}{|\delta V|} \int_{\delta V} \rho \mathbf{v} \gamma_\alpha dv \right] + \sum_{\beta \neq \alpha} \frac{1}{|\delta V|} \int_{\delta A_{\alpha\beta}} \rho \mathbf{v} \cdot \mathbf{n}_\alpha da. \quad (4.14)$$

Therefore (4.10) becomes

$$\begin{aligned} & \frac{\partial}{\partial t} \left[\frac{1}{|\delta V|} \int_{\delta V} \rho \gamma_\alpha dv \right] + \nabla \cdot \left[\frac{1}{|\delta V|} \int_{\delta V} \rho \mathbf{v} \gamma_\alpha dv \right] \\ &= \sum_{\beta \neq \alpha} \frac{1}{|\delta V|} \int_{\delta A_{\alpha\beta}} \rho \mathbf{w}_{\alpha\beta} \cdot \mathbf{n}_\alpha da - \sum_{\beta \neq \alpha} \frac{1}{|\delta V|} \int_{\delta A_{\alpha\beta}} \rho \mathbf{v} \cdot \mathbf{n}_\alpha da. \end{aligned} \quad (4.15)$$

Define

$$\epsilon^\alpha = \frac{|\delta V_\alpha|}{|\delta V|} \quad \text{and} \quad \sum_\alpha \epsilon^\alpha = 1, \quad (4.16)$$

$$\rho^\alpha = \frac{1}{|\delta V_\alpha|} \int_{\delta V} \rho \gamma_\alpha dv, \quad (4.17)$$

$$\mathbf{v}^\alpha = \frac{1}{\rho^\alpha |\delta V_\alpha|} \int_{\delta V} \rho \mathbf{v} \gamma_\alpha dv \quad (4.18)$$

$$\hat{e}_\beta^\alpha = \frac{1}{\rho^\alpha |\delta V_\alpha|} \int_{\delta A_{\alpha\beta}} [\rho(\mathbf{w}_{\alpha\beta} - \mathbf{v})] \cdot \mathbf{n}_\alpha da, \quad (4.19)$$

so that the macroscale equation of the conservation of mass (4.15) can be rewritten as

$$\frac{\partial(\epsilon^\alpha \rho^\alpha)}{\partial t} + \nabla \cdot (\epsilon^\alpha \rho^\alpha \mathbf{v}^\alpha) = \sum_{\beta \neq \alpha} \epsilon^\alpha \rho^\alpha \hat{e}_\beta^\alpha. \quad (4.20)$$

Next, we apply the same process to the conservation of momentum at the microscale,

$$\frac{\partial(\rho \mathbf{v})}{\partial t} + \nabla \cdot (\rho \mathbf{v} \mathbf{v}) - \nabla \cdot \mathbf{t} - \rho \mathbf{g} = \mathbf{0}, \quad (4.21)$$

where \mathbf{t} is the Cauchy stress tensor. Multiplying (4.21) by γ_α , integrating (4.21) with respect to δV and dividing by the volume $|\delta V|$, we have

$$\begin{aligned} & \frac{1}{|\delta V|} \int_{\delta V} \frac{\partial(\rho \mathbf{v})}{\partial t} \gamma_\alpha dv - \frac{1}{|\delta V|} \int_{\delta V} \nabla \cdot \mathbf{t} \gamma_\alpha dv + \frac{1}{|\delta V|} \int_{\delta V} \nabla \cdot (\rho \mathbf{v} \mathbf{v}) \gamma_\alpha dv \\ & - \frac{1}{|\delta V|} \int_{\delta V} \rho \mathbf{g} \gamma_\alpha dv = 0. \end{aligned} \quad (4.22)$$

Applying the averaging theorem to each term in (4.22), we have

$$\frac{1}{|\delta V|} \int_{\delta V} \frac{\partial(\rho \mathbf{v})}{\partial t} \gamma_\alpha dv = \frac{\partial}{\partial t} \left[\frac{1}{|\delta V|} \int_{\delta V} \rho \mathbf{v} \gamma_\alpha dv \right] - \sum_{\beta \neq \alpha} \frac{1}{|\delta V|} \int_{\delta A_{\alpha\beta}} \rho \mathbf{v} \mathbf{w}_{\alpha\beta} \cdot \mathbf{n}_\alpha da, \quad (4.23)$$

$$\frac{1}{|\delta V|} \int_{\delta V} \nabla \cdot \mathbf{t} \gamma_\alpha dv = \nabla \cdot \left[\frac{1}{|\delta V|} \int_{\delta V} \mathbf{t} \gamma_\alpha dv \right] + \sum_{\beta \neq \alpha} \frac{1}{|\delta V|} \int_{\delta A_{\alpha\beta}} \mathbf{t} \mathbf{n}_\alpha da, \quad (4.24)$$

$$\frac{1}{|\delta V|} \int_{\delta V} \nabla \cdot (\rho \mathbf{v} \mathbf{v}) \gamma_\alpha dv = \nabla \cdot \left[\frac{1}{|\delta V|} \int_{\delta V} \rho \mathbf{v} \mathbf{v} \gamma_\alpha dv \right] + \sum_{\beta \neq \alpha} \frac{1}{|\delta V|} \int_{\delta A_{\alpha\beta}} \rho \mathbf{v} \mathbf{v} \mathbf{n}_\alpha da. \quad (4.25)$$

Therefore (4.22) becomes

$$\frac{\partial}{\partial t} \left[\frac{1}{|\delta V|} \int_{\delta V} \rho \mathbf{v} \gamma_\alpha dv \right] - \nabla \cdot \left[\frac{1}{|\delta V|} \int_{\delta V} \mathbf{t} \gamma_\alpha dv \right] + \nabla \cdot \left[\frac{1}{|\delta V|} \int_{\delta V} \rho \mathbf{v} \mathbf{v} \gamma_\alpha dv \right]$$

$$\begin{aligned}
-\frac{1}{|\delta V|} \int_{\delta V} \rho \mathbf{g} \gamma_\alpha dv &= \sum_{\beta \neq \alpha} \frac{1}{|\delta V|} \int_{\delta A_{\alpha\beta}} \rho \mathbf{v} \mathbf{w}_{\alpha\beta} \cdot \mathbf{n}_\alpha da + \sum_{\beta \neq \alpha} \frac{1}{|\delta V|} \int_{\delta A_{\alpha\beta}} \mathbf{t} \mathbf{n}_\alpha da \\
&\quad - \sum_{\beta \neq \alpha} \frac{1}{|\delta V|} \int_{\delta A_{\alpha\beta}} \rho \mathbf{v} \mathbf{v} \mathbf{n}_\alpha da. \tag{4.26}
\end{aligned}$$

Defining

$$\frac{D^\alpha}{Dt} = \frac{\partial}{\partial t} + \mathbf{v}^\alpha \cdot \nabla \tag{4.27}$$

$$\mathbf{g}^\alpha = \frac{1}{\rho^\alpha |\delta V_\alpha|} \int_{\delta V} \rho \mathbf{g} \gamma_\alpha dv, \tag{4.28}$$

$$\mathbf{t}^\alpha = \frac{1}{|\delta V_\alpha|} \int_{\delta V} \mathbf{t} \gamma_\alpha dv - \frac{1}{|\delta V_\alpha|} \int_{\delta V} \rho \mathbf{v} \mathbf{v} \gamma_\alpha dv + \rho^\alpha \mathbf{v}^\alpha \mathbf{v}^\alpha \tag{4.29}$$

$$\hat{\mathbf{T}}_\beta^\alpha = \frac{1}{\rho^\alpha |\delta V_\alpha|} \int_{\delta A_{\alpha\beta}} [\mathbf{t} + \rho \mathbf{v} (\mathbf{w}_{\alpha\beta} - \mathbf{v})] \cdot \mathbf{n}_\alpha da - \mathbf{v}^\alpha \hat{e}_\beta^\alpha, \tag{4.30}$$

equation (4.26) can be rewritten as

$$\frac{\partial}{\partial t} (\epsilon^\alpha \rho^\alpha \mathbf{v}^\alpha) + \nabla \cdot (\epsilon^\alpha \rho^\alpha \mathbf{v}^\alpha \mathbf{v}^\alpha) - \nabla \cdot (\epsilon^\alpha \mathbf{t}^\alpha) - \epsilon^\alpha \rho^\alpha \mathbf{g}^\alpha = \sum_{\beta \neq \alpha} \epsilon^\alpha \rho^\alpha (\hat{\mathbf{T}}_\beta^\alpha + \hat{e}_\beta^\alpha \mathbf{v}^\alpha), \tag{4.31}$$

where

$$\sum_{\beta \neq \alpha} \epsilon^\alpha \rho^\alpha (\hat{\mathbf{T}}_\beta^\alpha + \hat{e}_\beta^\alpha \mathbf{v}^\alpha) = \sum_{\beta \neq \alpha} \frac{1}{|\delta V|} \int_{\delta A_{\alpha\beta}} [\mathbf{t} + \rho \mathbf{v} (\mathbf{w}_{\alpha\beta} - \mathbf{v})] \cdot \mathbf{n}_\alpha da. \tag{4.32}$$

To simplify the macroscopic scale of the linear momentum equation (4.31), we begin by applying the chain rule to the first two term of (4.31) and then employing the macroscale continuity equation (4.20) to replace the time derivative and advection terms, $\partial(\epsilon^\alpha \rho^\alpha)/\partial t + \nabla \cdot (\epsilon^\alpha \rho^\alpha \mathbf{v}^\alpha)$, by the interactive quantity at the interface $\alpha\beta$, $\sum_{\beta \neq \alpha} \epsilon^\alpha \rho^\alpha \hat{e}_\beta^\alpha$, as follows.

$$\begin{aligned}
\sum_{\beta \neq \alpha} \epsilon^\alpha \rho^\alpha (\hat{\mathbf{T}}_\beta^\alpha + \hat{e}_\beta^\alpha \mathbf{v}^\alpha) &= \frac{\partial}{\partial t} (\epsilon^\alpha \rho^\alpha \mathbf{v}^\alpha) + \nabla \cdot (\epsilon^\alpha \rho^\alpha \mathbf{v}^\alpha \mathbf{v}^\alpha) - \nabla \cdot (\epsilon^\alpha \mathbf{t}^\alpha) - \epsilon^\alpha \rho^\alpha \mathbf{g}^\alpha \\
&= \frac{\partial(\epsilon^\alpha \rho^\alpha)}{\partial t} \mathbf{v}^\alpha + (\epsilon^\alpha \rho^\alpha) \frac{\partial}{\partial t} \mathbf{v}^\alpha + \nabla \cdot (\epsilon^\alpha \rho^\alpha \mathbf{v}^\alpha) \mathbf{v}^\alpha + \epsilon^\alpha \rho^\alpha \mathbf{v}^\alpha \cdot \nabla \mathbf{v}^\alpha - \nabla \cdot (\epsilon^\alpha \mathbf{t}^\alpha) - \epsilon^\alpha \rho^\alpha \mathbf{g}^\alpha \\
&= \left[\frac{\partial(\epsilon^\alpha \rho^\alpha)}{\partial t} + \nabla \cdot (\epsilon^\alpha \rho^\alpha \mathbf{v}^\alpha) \right] \mathbf{v}^\alpha + (\epsilon^\alpha \rho^\alpha) \frac{\partial}{\partial t} \mathbf{v}^\alpha + \epsilon^\alpha \rho^\alpha \mathbf{v}^\alpha \cdot \nabla \mathbf{v}^\alpha - \nabla \cdot (\epsilon^\alpha \mathbf{t}^\alpha) - \epsilon^\alpha \rho^\alpha \mathbf{g}^\alpha \\
&= \sum_{\beta \neq \alpha} \epsilon^\alpha \rho^\alpha \hat{e}_\beta^\alpha \mathbf{v}^\alpha + (\epsilon^\alpha \rho^\alpha) \frac{\partial}{\partial t} \mathbf{v}^\alpha + \epsilon^\alpha \rho^\alpha \mathbf{v}^\alpha \cdot \nabla \mathbf{v}^\alpha - \nabla \cdot (\epsilon^\alpha \mathbf{t}^\alpha) - \epsilon^\alpha \rho^\alpha \mathbf{g}^\alpha. \tag{4.33}
\end{aligned}$$

Canceling $\sum_{\beta \neq \alpha} \epsilon^\alpha \rho^\alpha \hat{e}_\beta^\alpha \mathbf{v}^\alpha$ from both sides of (4.33) and applying the material time derivative definition (4.27), yields

$$\epsilon^\alpha \rho^\alpha \frac{D^\alpha \mathbf{v}^\alpha}{Dt} - \nabla \cdot (\epsilon^\alpha \mathbf{t}^\alpha) - \epsilon^\alpha \rho^\alpha \mathbf{g}^\alpha = \sum_{\alpha \neq \beta} \epsilon^\alpha \rho^\alpha \hat{\mathbf{T}}_\beta^\alpha \tag{4.34}$$

which is the general form of the macroscopic scale of the momentum equation.

4.2 The Continuity Equation

The continuity equation is the conservation of mass, and the goal of this section is to derive equation (4.7) by using simplifying assumptions. We first begin with the macroscale continuity equation

$$\frac{\partial(\epsilon^\alpha \rho^\alpha)}{\partial t} + \nabla \cdot (\epsilon^\alpha \rho^\alpha \mathbf{v}^\alpha) = \sum_{\beta \neq \alpha} \epsilon^\alpha \rho^\alpha \hat{e}_\beta^\alpha. \quad (4.35)$$

Applying the chain rule to the second term of (4.35), we obtain

$$\frac{\partial(\epsilon^\alpha \rho^\alpha)}{\partial t} + \mathbf{v}^\alpha \nabla \cdot \epsilon^\alpha \rho^\alpha + \epsilon^\alpha \rho^\alpha \nabla \cdot \mathbf{v}^\alpha = \sum_{\beta \neq \alpha} \epsilon^\alpha \rho^\alpha \hat{e}_\beta^\alpha. \quad (4.36)$$

Using the material time derivative definition (4.27) to (4.36), we have

$$\frac{D^\alpha(\epsilon^\alpha \rho^\alpha)}{\partial t} + \epsilon^\alpha \rho^\alpha \nabla \cdot \mathbf{v}^\alpha = \sum_{\beta \neq \alpha} \epsilon^\alpha \rho^\alpha \hat{e}_\beta^\alpha. \quad (4.37)$$

Our first assumption is that there is no chemical reaction between the liquid and solid phases, so that the right-hand side of (4.37) is zero and it becomes

$$\frac{D^\alpha(\epsilon^\alpha \rho^\alpha)}{\partial t} + \epsilon^\alpha \rho^\alpha \nabla \cdot \mathbf{v}^\alpha = 0. \quad (4.38)$$

We next assume both the liquid and solid phases are incompressible so that $D^\alpha \rho^\alpha / \partial t = 0$.

Then (4.38) written for both liquid and solid phases becomes

$$\frac{D^l \epsilon^l}{Dt} + \epsilon^l \nabla \cdot \mathbf{v}^l = 0, \quad (4.39)$$

$$\frac{D^s \epsilon^s}{Dt} + \epsilon^s \nabla \cdot \mathbf{v}^s = 0. \quad (4.40)$$

Since the volume of the solid can be written in terms of the liquid volume fraction, $\epsilon^s = 1 - \epsilon^l$, we can eliminate ϵ^s from (4.40)

$$-\frac{D^s \epsilon^l}{Dt} + (1 - \epsilon^l) \nabla \cdot \mathbf{v}^s = 0. \quad (4.41)$$

Adding (4.39) and (4.41), we obtain

$$\frac{D^l \epsilon^l}{Dt} - \frac{D^s \epsilon^l}{\partial t} + \epsilon^l (\nabla \cdot \mathbf{v}^l - \nabla \cdot \mathbf{v}^s) + \nabla \cdot \mathbf{v}^s = 0. \quad (4.42)$$

From the definition of the material time derivative:

$$\frac{D^l}{Dt} = \frac{\partial}{\partial t} + \mathbf{v}^l \cdot \nabla \quad \text{and} \quad -\frac{D^s}{Dt} = -\frac{\partial}{\partial t} - \mathbf{v}^s \cdot \nabla, \quad (4.43)$$

we have

$$\frac{D^l \epsilon^l}{Dt} = \frac{\partial \epsilon^l}{\partial t} + \mathbf{v}^l \cdot \nabla \epsilon^l \quad \text{and} \quad -\frac{D^s \epsilon^l}{Dt} = -\frac{\partial \epsilon^l}{\partial t} - \mathbf{v}^s \cdot \nabla \epsilon^l. \quad (4.44)$$

Adding the two equations of (4.44), we get

$$\frac{D^l \epsilon^l}{Dt} - \frac{D^s \epsilon^l}{Dt} = (\mathbf{v}^l - \mathbf{v}^s) \cdot \nabla \epsilon^l. \quad (4.45)$$

Eliminating the term $\frac{D^l \epsilon^l}{Dt} - \frac{D^s \epsilon^l}{Dt}$ by combining (4.45) and (4.42) together gives

$$(\mathbf{v}^l - \mathbf{v}^s) \cdot \nabla \epsilon^l + \epsilon^l \nabla \cdot (\mathbf{v}^l - \mathbf{v}^s) + \nabla \cdot \mathbf{v}^s = 0, \quad (4.46)$$

or

$$\nabla \cdot \epsilon^l (\mathbf{v}^l - \mathbf{v}^s) + \nabla \cdot \mathbf{v}^s = 0. \quad (4.47)$$

So we have

$$\nabla \cdot \mathbf{v}^s = -\nabla \cdot \epsilon^l (\mathbf{v}^l - \mathbf{v}^s), \quad (4.48)$$

and substituting (4.48) into (4.41), we get

$$\frac{D^s \epsilon^l}{Dt} + (1 - \epsilon^l) \nabla \cdot \epsilon^l (\mathbf{v}^l - \mathbf{v}^s) = 0, \quad (4.49)$$

which is the form of the continuity equation for an incompressible solid and liquid phases that we will use.

4.3 Darcy's Law

Darcy's Law is a widely used concept used to model flow through a porous medium. In this section, we derive a generalized form of Darcy's Law using HMT. We assume we have only two phases, solid and liquid. Thus equation (4.34) can be written as

$$\epsilon^l \rho^l \frac{D^l \mathbf{v}^l}{Dt} - \nabla \cdot (\epsilon^l \mathbf{t}^l) - \epsilon^l \rho^l \mathbf{g}^l = \epsilon^l \rho^l \hat{\mathbf{T}}_s^l, \quad (4.50)$$

where $\hat{\mathbf{T}}_s^l$ is the rate at which momentum is exchanged from the solid phase to the liquid phase. Note that at this point we haven't incorporated any constitutive equations. By exploiting the entropy inequality and linearizing $\hat{\mathbf{T}}_s^l$ about the variable $\mathbf{v}^l - \mathbf{v}^s$ where l and s stand for liquid and solid phases [103, 109], we obtain

$$\epsilon^l \rho^l \hat{\mathbf{T}}_s^l = p \nabla \epsilon^l - \epsilon^l \mathbf{R} \cdot (\mathbf{v}^l - \mathbf{v}^s). \quad (4.51)$$

where \mathbf{R} is second-order tensor resulting from linearization. Now, we consider the macroscale Cauchy stress tensor on the left-hand side of (4.50). The equation for the stress tensor (4.29) involves microscale variables. Darcy's Law is a macroscale equation so we cannot use (4.29) to obtain Darcy's Law. By exploiting the entropy equation we obtain that the constitutive equation for the liquid stress tensor is given by

$$\mathbf{t}^l = -p \mathbf{I} + 2\mu \mathbf{d}^l, \quad (4.52)$$

where p and \mathbf{d}^l are the pressure and the rate of deformation for the liquid phase. Substituting (4.51) and (4.52) into (4.50), we have

$$\epsilon^l \rho^l \frac{D^l \mathbf{v}^l}{Dt} - \nabla \cdot (-\epsilon^l p \mathbf{I} + \epsilon^l 2\mu \mathbf{d}^l) - \epsilon^l \rho^l \mathbf{g}^l = p \nabla \epsilon^l - \epsilon^l \mathbf{R} \cdot (\mathbf{v}^l - \mathbf{v}^s). \quad (4.53)$$

Note that

$$\nabla \cdot (\epsilon^l p \mathbf{I}) = \epsilon^l \nabla \cdot (p \mathbf{I}) + p \mathbf{I} \cdot (\nabla \epsilon^l) = \epsilon^l \nabla p + p \nabla \epsilon^l. \quad (4.54)$$

Thus, (4.53) can be rewritten as

$$\epsilon^l \rho^l \frac{D^l \mathbf{v}^l}{Dt} + \epsilon^l \nabla p + p \nabla \epsilon^l - \nabla \cdot (\epsilon^l 2\mu \mathbf{d}^l) - \epsilon^l \rho^l \mathbf{g}^l = p \nabla \epsilon^l - \epsilon^l \mathbf{R} \cdot (\mathbf{v}^l - \mathbf{v}^s). \quad (4.55)$$

Canceling $p \nabla \epsilon^l$ from both sides and neglecting the inertial and viscosity terms, we have

$$\epsilon^l \nabla p - \epsilon^l \rho^l \mathbf{g}^l = -\epsilon^l \mathbf{R} \cdot (\mathbf{v}^l - \mathbf{v}^s), \quad (4.56)$$

where \mathbf{g}^l is the gravity vector $\mathbf{g} = (0, 0, -g)$. Dividing both sides by ϵ^l and letting $\mathbf{R} = \mu \epsilon^l \mathbf{k}^{-1}$, we have Darcy's law:

$$\epsilon^l (\mathbf{v}^l - \mathbf{v}^s) = -\frac{\mathbf{k}}{\mu} \cdot (\nabla p - \rho \mathbf{g}), \quad (4.57)$$

where the superscript l is dropped from the gravity term in order to be consistent with the notation in the previous sections.

By employing the general form of the macroscopic scale of the momentum equation (4.34) and linearizing the rate, $\hat{\mathbf{T}}_s^l$, at which momentum is exchanged from the solid phase to the liquid phase, we now have the widely used model, Darcy's Law. Next, we show that Darcy's law can be extended to the Brinkman equation.

4.4 Derivation of the Brinkman equation

In this section, we derive the Brinkman equation by using HMT and nondimensionalization. We begin with the version of Darcy's Law given by (4.55):

$$\epsilon^l \rho^l \frac{D^l \mathbf{v}^l}{Dt} + \epsilon^l \nabla p + p \nabla \epsilon^l - \nabla \cdot (\epsilon^l 2\mu \mathbf{d}^l) - \epsilon^l \rho^l \mathbf{g}^l = p \nabla \epsilon^l - \epsilon^l \mathbf{R} \cdot (\mathbf{v}^l - \mathbf{v}^s). \quad (4.58)$$

Subtracting $p \nabla \epsilon^l$ from both sides, dividing both sides by ϵ^l and letting $\mu \epsilon^l \mathbf{k}^{-1} = \mathbf{R}$, we have

$$\rho \frac{D^l \mathbf{v}^l}{Dt} + \nabla p - \frac{\mu}{\epsilon^l} \nabla \cdot (2\epsilon^l \mathbf{d}^l) - \rho \mathbf{g} = -\mu \epsilon^l \mathbf{k}^{-1} \cdot (\mathbf{v}^l - \mathbf{v}^s), \quad (4.59)$$

or by rearranging the terms,

$$\rho \left(\frac{\partial \mathbf{v}^l}{\partial t} + \mathbf{v}^l \cdot \nabla \mathbf{v}^l \right) + \mu \mathbf{k}^{-1} \cdot (\epsilon^l \mathbf{v}^l - \epsilon^l \mathbf{v}^s) + \nabla p - \frac{\mu}{\epsilon^l} \nabla \cdot (2\epsilon^l \mathbf{d}^l) = \rho \mathbf{g} \quad (4.60)$$

Scaling Parameter	Description	Primary Dimensions
L	characteristic length	$[L]$
f	characteristic frequency	$[1/t]$
v_0	characteristic speed	$[L/t]$
p_0	reference pressure	$[M/(Lt^2)]$
g_0	gravitational acceleration	$[L/t^2]$

Table 4.1: Characteristic parameters

where $\frac{D^l}{Dt} = \frac{\partial}{\partial t} + \mathbf{v}^l \cdot \nabla$ is the material time derivative. Next, we normalize equation (4.60) and show that some terms in the equation can be neglected with respect to our problem. To normalize (4.60), we choose scaling parameters defined in Table 4.1. Define the following dimensionless variables:

$$\tilde{\mathbf{v}}^l = \frac{\mathbf{v}^l}{v_0}, \quad \tilde{\mathbf{v}}^s = \frac{\mathbf{v}^s}{v_0}, \quad \tilde{p} = \frac{p}{p_0}, \quad \tilde{\mathbf{g}} = \frac{\mathbf{g}}{g_0}, \quad (4.61)$$

$$\tilde{\nabla} = L\nabla, \quad \tilde{t} = ft, \quad \tilde{\Delta} = L^2\Delta. \quad (4.62)$$

Substituting (4.61)–(4.62) into (4.60), we get

$$\begin{aligned} \rho f v_0 \frac{\partial \tilde{\mathbf{v}}^l}{\partial \tilde{t}} + \frac{\rho v_0^2}{L} \tilde{\mathbf{v}}^l \cdot \tilde{\nabla} \tilde{\mathbf{v}}^l + v_0 \mu \mathbf{k}^{-1} (\epsilon^l \tilde{\mathbf{v}}^l - \epsilon^l \tilde{\mathbf{v}}^s) + \frac{p_0}{L} \tilde{\nabla} \tilde{p} \\ - \frac{1}{\epsilon^l} \frac{\mu v_0}{L^2} \tilde{\nabla} \cdot (2\epsilon^l \tilde{\mathbf{d}}^l) = \rho g_0 \tilde{\mathbf{g}}. \end{aligned} \quad (4.63)$$

where $\tilde{\mathbf{d}}^l = \frac{1}{2} ((\tilde{\nabla} \tilde{\mathbf{v}})^T + (\tilde{\nabla} \tilde{\mathbf{v}}))$. Multiplying (4.63) by $\mathbf{k}/\mu v_0$, we have

$$\epsilon^l \tilde{\mathbf{v}}^l - \epsilon^l \tilde{\mathbf{v}}^s = -\frac{\mathbf{k}}{\mu} \left[\rho f \frac{\partial \tilde{\mathbf{v}}^l}{\partial \tilde{t}} + \frac{\rho v_0}{L} \tilde{\mathbf{v}}^l \cdot \tilde{\nabla} \tilde{\mathbf{v}}^l + \frac{p_0}{L v_0} \tilde{\nabla} \tilde{p} - \frac{\rho g_0}{v_0} \tilde{\mathbf{g}} - \frac{1}{\epsilon^l} \frac{\mu}{L^2} \tilde{\nabla} \cdot (2\epsilon^l \tilde{\mathbf{d}}^l) \right]. \quad (4.64)$$

For our slow flow problem, we choose the reference time t to be the time it takes the cilia to go through one cycle, L to be the height of the cilia, ρ and μ to be the density and dynamic viscosity of water at temperature 40 °C and g_0 to be the Earth's gravity. Then

$$t \approx 1.029 \text{ s}, \quad L \approx 7 \times 10^{-6} \text{ m}, \quad \rho \approx 992.2 \text{ kg/m}^3, \quad g_0 = 9.81 \text{ m/s}^2, \quad (4.65)$$

$$\mu \approx 0.653 \times 10^{-3} \text{ kg}/(\text{m} \cdot \text{s}), \quad p_0 = 10^{-1} \text{ kg}/(\text{m} \cdot \text{s}^2), \quad (4.66)$$

where the units are in International System of Units, SI. The values of time t and length L are from [77] and [20], respectively. Then the characteristic speed at the tip of the cilia is

$$v_0 = \frac{L\theta}{t} = (7 \times 10^{-6})(\pi/4)/1.029 \approx 5.34 \times 10^{-6} \text{ m/s}, \quad (4.67)$$

where θ is the angle between the cilia and the horizontal plane. For the permeability and porosity, we employ the maximum values from our numerical results. Therefore the scalar permeability and porosity are

$$k = 10^{-14} \text{ m}^2, \quad \epsilon^l = 1, \quad (4.68)$$

respectively. For our convenience to determine the values of each coefficient, we rewrite (4.64) as

$$C_1(\epsilon^l \tilde{\mathbf{v}}^l - \epsilon^l \tilde{\mathbf{v}}^s) = -C_2 \frac{\partial \tilde{\mathbf{v}}^l}{\partial \tilde{t}} - C_3 \tilde{\mathbf{v}}^l \cdot \tilde{\nabla} \tilde{\mathbf{v}}^l - C_4 \tilde{\nabla} \tilde{p} + C_5 \tilde{\mathbf{g}} + C_6 \tilde{\nabla} \cdot (2\epsilon^l \tilde{\mathbf{d}}^l), \quad (4.69)$$

where the coefficients after substituted by the values from (4.65), (4.66), (4.67) and (4.68) are

$$C_1 = 1 \quad (4.70)$$

$$C_2 = \frac{k\rho f}{\mu} = 1.47 \times 10^{-8} \quad (4.71)$$

$$C_3 = \frac{k\rho v_0}{\mu L} = 1.15 \times 10^{-8} \quad (4.72)$$

$$C_4 = \frac{k p_0}{\mu v_0 L} = 4.09 \times 10^{-2} \quad (4.73)$$

$$C_5 = \frac{k\rho g_0}{\mu v_0} = 2.79 \times 10^{-2} \quad (4.74)$$

$$C_6 = \frac{k}{\epsilon^l L^2} = 2.04 \times 10^{-4}. \quad (4.75)$$

The coefficients C_2 and C_3 are relatively small in comparison with the others. Neglecting these terms, (4.60) becomes

$$\mu \mathbf{k}^{-1} \cdot (\epsilon^l \mathbf{v}^l - \epsilon^l \mathbf{v}^s) + \nabla p - \frac{\mu}{\epsilon^l} \nabla \cdot (2\epsilon^l \mathbf{d}^l) = \rho \mathbf{g}. \quad (4.76)$$

which is the Brinkman equation.

4.5 Derivation of Stokes Equation

In this section, we nondimensionalize the Navier-Stokes equation to show that some terms in this equation are negligible for our problem in domain Ω_1 . We begin with the Navier-Stokes equation which is the differential equation for conservation of momentum for a fluid with stress given by a constitutive equation for a Newtonian fluid. For incompressible flow, it can be written in the form

$$\rho \left(\frac{\partial \mathbf{v}}{\partial t} + \mathbf{v} \cdot \nabla \mathbf{v} \right) = -\nabla p + \rho \mathbf{g} + \mu \Delta \mathbf{v} \quad (4.77)$$

Using the same characteristic parameters as given in Table 4.1, the nondimensional variables are defined to be

$$\tilde{\mathbf{v}} = \frac{\mathbf{v}}{v_0}, \quad \tilde{p} = \frac{p}{p_0}, \quad \tilde{\mathbf{g}} = \frac{\mathbf{g}}{g_0}, \quad (4.78)$$

$$\tilde{\nabla} = L \nabla, \quad \tilde{t} = ft, \quad \tilde{\Delta} = L^2 \Delta. \quad (4.79)$$

Substituting (4.78)–(4.79) into (4.77), we have

$$\rho f v_0 \left(\frac{\partial \tilde{\mathbf{v}}}{\partial \tilde{t}} \right) + \frac{\rho v_0^2}{L} (\tilde{\mathbf{v}} \cdot \tilde{\nabla} \tilde{\mathbf{v}}) = -\frac{p_0}{L} \tilde{\nabla} \tilde{p} + \rho g_0 \tilde{\mathbf{g}} + \frac{\mu v_0}{L^2} \tilde{\Delta} \tilde{\mathbf{v}}. \quad (4.80)$$

Multiplying (4.80) by $L^2/\mu v_0$, we obtain

$$\frac{\rho f L^2}{\mu} \left(\frac{\partial \tilde{\mathbf{v}}}{\partial \tilde{t}} \right) + \frac{\rho L v_0}{\mu} (\tilde{\mathbf{v}} \cdot \tilde{\nabla} \tilde{\mathbf{v}}) = -\frac{p_0 L}{\mu v_0} \tilde{\nabla} \tilde{p} + \frac{\rho g_0 L^2}{\mu v_0} \tilde{\mathbf{g}} + \tilde{\Delta} \tilde{\mathbf{v}}. \quad (4.81)$$

Note that the coefficient in front of $\tilde{\mathbf{v}} \cdot \tilde{\nabla} \tilde{\mathbf{v}}$ is the Reynolds number. Using the values from (4.65)–(4.67), we obtain the coefficients:

$$\frac{\rho f L^2}{\mu} = 7.23 \times 10^{-5}, \quad (4.82)$$

$$\frac{\rho L v_0}{\mu} = 5.67 \times 10^{-5}, \quad (4.83)$$

$$\frac{p_0 L}{\mu v_0} = 2.00 \times 10^2, \quad (4.84)$$

$$\frac{\rho g_0 L^2}{\mu v_0} = 1.36 \times 10^2. \quad (4.85)$$

Neglecting the terms associated with coefficients (4.82)-(4.83), equation (4.77) becomes

$$\nabla p - \rho \mathbf{g} = \mu \Delta \mathbf{v}, \quad (4.86)$$

which is the Stokes equation.

4.6 Well-posedness Stokes-Brinkman

Ingram [54] proved the well-posedness of the Stokes-Brinkman system of equations for a positive constant permeability. Here we show the existence and uniqueness for a permeability tensor \mathbf{k} . Recall the Brinkman and continuity equations are

$$\mu \mathbf{k}^{-1} \cdot (\epsilon^l \mathbf{v}^l - \epsilon^l \mathbf{v}^s) + \nabla p - \frac{\mu}{\epsilon^l} \nabla \cdot (2\epsilon^l \mathbf{d}^l) = \rho \mathbf{g}, \quad \text{in } \Omega \quad (4.87a)$$

$$\epsilon^l + (1 - \epsilon^l) \nabla \cdot (\epsilon^l (\mathbf{v}^l - \mathbf{v}^s)) = 0 \quad \text{in } \Omega \quad (4.87b)$$

where $\mathbf{d}^l = 1/2(\nabla \mathbf{v}^l + (\nabla \mathbf{v}^l)^T)$ is the rate of deformation and the superscript T is the transpose. The velocity of the liquid \mathbf{v}^l and the pressure p are unknown. Since the solid velocity \mathbf{v}^s , dynamic viscosity μ , porosity ϵ^l and inverse of the permeability \mathbf{k}^{-1} are known, we move $\mu \mathbf{k}^{-1} \cdot \epsilon^l \mathbf{v}^s$ to the right-hand side and equation (4.87a) becomes

$$\mu \mathbf{k}^{-1} \cdot \epsilon^l \mathbf{v}^l + \nabla p - \frac{\mu}{\epsilon^l} \nabla \cdot (2\epsilon^l \mathbf{d}^l) = \rho \mathbf{g} + \mu \mathbf{k}^{-1} \cdot \epsilon^l \mathbf{v}^s, \quad (4.88)$$

which is the Stokes equation when \mathbf{k}^{-1} is zero. Define the spaces

$$L_0^2(\Omega) = \{q \in L^2(\Omega) : \int_{\Omega} q d\Omega = 0\} \quad (4.89)$$

$$H_0^1(\Omega) = \{\mathbf{w} \in H^1(\Omega) : \mathbf{w}|_{\partial\Omega} = 0\} \quad (4.90)$$

$$H_s^1(\Omega) = \{\mathbf{w} \in H^1(\Omega) : \mathbf{w}|_{\partial\Omega} = \mathbf{s}\} \quad (4.91)$$

$$H^{-1}(\Omega) = (H_0^1(\Omega))', \text{ the dual of } H_0^1(\Omega) \quad (4.92)$$

$$V = \{\mathbf{w} \in H^1(\Omega) : \mathbf{w}|_{\partial\Omega} = 0 \text{ and } \nabla \cdot \mathbf{w} = 0\} \quad (4.93)$$

$$V^\perp = \{\mathbf{w}^\perp \in H_0^1(\Omega) : \int_{\Omega} \mathbf{w}^\perp \cdot \mathbf{w} = 0 \quad \forall \mathbf{w} \in V\} \quad (4.94)$$

$$V^0 = \{\mathbf{w}' \in H^{-1}(\Omega) : \langle \mathbf{w}', \mathbf{w} \rangle_{H^{-1}(\Omega) \times H_0^1(\Omega)} = 0 \quad \forall \mathbf{w} \in V\} \quad (4.95)$$

where V^\perp denotes the orthogonal of V in $H_0^1(\Omega)$ associated with the $H^1(\Omega)$ seminorm $|\cdot|_{H^1(\Omega)}$; V^0 is the polar set of V ; $\langle \cdot, \cdot \rangle_{H^{-1}(\Omega) \times H_0^1(\Omega)}$ represents the duality pairing between $H^{-1}(\Omega)$ and $H_0^1(\Omega)$, and the trace theorem 4.5, below, ensures the existence of the function $\mathbf{s} \in H^{1/2}(\partial\Omega)$ used in the definition of seminorm. Note that for a three-dimensional domain, $\mathbf{w} \in H^1(\Omega)^3$ and $\nabla \mathbf{w} \in H^1(\Omega)^{3 \times 3}$. However, for simplicity, we write $\mathbf{w} \in H^1(\Omega)$ in any case and the meaning follows from the context. Let the vector $\mathbf{f}_1 = \rho \mathbf{g} + \mu \mathbf{k}^{-1} \cdot \epsilon^l \mathbf{v}^s$, where \mathbf{v}^s is a bounded continuous function. Let $\mathbf{f}_1 \in H^{-1}(\Omega)$ with the following norm:

$$\|\mathbf{f}_1\|_{H^{-1}(\Omega)} = \sup_{\mathbf{w} \in H_0^1(\Omega), \mathbf{w} \neq 0} \frac{\langle \mathbf{f}_1, \mathbf{w} \rangle_{H^{-1}(\Omega) \times H_0^1(\Omega)}}{\|\mathbf{w}\|_{H^1(\Omega)}} \quad (4.96)$$

where $\|\cdot\|_{H^1(\Omega)}$ represents the standard norm for $H^1(\Omega)$. Note that

$$\nabla \cdot (2\epsilon^l \mathbf{d}^l) = \Delta(\epsilon^l \mathbf{v}^l) + \nabla(\nabla \cdot \epsilon^l \mathbf{v}^l). \quad (4.97)$$

Assume ϵ^l is fixed in space and define

$$\mathbf{v} = \epsilon^l \mathbf{v}^l. \quad (4.98)$$

Then equations (4.88) and (4.87b) can be rewritten as

$$\mu \mathbf{k}^{-1} \cdot \mathbf{v} + \nabla p - \frac{\mu}{\epsilon^l} \Delta \mathbf{v} = \mathbf{f}_1 + \frac{\mu}{\epsilon^l} \nabla(\nabla \cdot \mathbf{v}), \quad (4.99a)$$

$$\nabla \cdot \mathbf{v} = -\frac{\dot{\epsilon}^l}{(1 - \epsilon^l)} + \nabla \cdot \epsilon^l \mathbf{v}^s, \quad (4.99b)$$

where the right-hand side of (4.99b) is known. Using (4.99b) to eliminate the last term in (4.99a) and letting $f = -\dot{\epsilon}^l/(1 - \epsilon^l) + \nabla \cdot \epsilon^l \mathbf{v}^s$ and $\mathbf{f} = \mathbf{f}_1 + \mu/\epsilon^l \nabla f$, we get the Stokes-Brinkman equations in the following form

$$\mu \mathbf{k}^{-1} \cdot \mathbf{v} + \nabla p - \frac{\mu}{\epsilon^l} \Delta \mathbf{v} = \mathbf{f} \quad (4.100a)$$

$$\nabla \cdot \mathbf{v} = f. \quad (4.100b)$$

Define the linear and bilinear functionals

$$a(\mathbf{v}, \mathbf{w}) = \int_{\Omega} \frac{\mu}{\epsilon^l} \nabla \mathbf{v} : \nabla \mathbf{w} + \int_{\Omega} \mu (\mathbf{k}^{-1} \cdot \mathbf{v}) \cdot \mathbf{w}, \quad (4.101)$$

$$b(\mathbf{v}, q) = - \int_{\Omega} q \nabla \cdot \mathbf{v}, \quad (4.102)$$

$$c_1(\mathbf{w}) = \langle \mathbf{f}_1, \mathbf{w} \rangle_{H^{-1}(\Omega) \times H_0^1(\Omega)} - \int_{\Omega} \frac{\mu}{\epsilon^l} f \nabla \cdot \mathbf{w}, \quad (4.103)$$

$$c_2(q) = - \int_{\Omega} f q. \quad (4.104)$$

Then, the weak formulation of (4.100) can be expressed as

Problem 4.1 (*Weak Stokes-Brinkman*) Find $\mathbf{v} \in H_s^1(\Omega)$ and $p \in L_0^2(\Omega)$ such that

$$\forall \mathbf{w} \in H_0^1(\Omega), \quad a(\mathbf{v}, \mathbf{w}) + b(\mathbf{w}, p) = c_1(\mathbf{w}), \quad (4.105a)$$

$$\forall q \in L_0^2(\Omega), \quad b(\mathbf{v}, q) = c_2(q). \quad (4.105b)$$

Before we prove the existence and uniqueness of the Stokes-Brinkman equation, we first introduce the following norms, seminorms and theorems, [23].

Definition 4.2 (*Weak derivative*) We say that a given function $v \in L_{loc}^1(\Omega)$ has a **weak derivative**, $D_w^\alpha v$, provided there exists a function $w \in L_{loc}^1(\Omega)$ such that

$$\int_{\Omega} w(x) \phi(x) dx = (-1)^{|\alpha|} \int_{\Omega} v(x) \phi^{(\alpha)}(x) dx \quad \forall \phi \in C_0^\infty(\Omega) \quad (4.106)$$

where $C_0^\infty(\Omega)$ is the set of functions with compact support in Ω ; $L_{loc}^1(\Omega) = \{v : v \in L^1(K) \ \forall \text{ compact } K \subset \text{interior } \Omega\}$. If such a w exists, we define $D_w^\alpha v = w$.

Definition 4.3 (*Sobolev norm*) Let k be a non-negative integer, and let $f \in L_{loc}^1(\Omega)$. Suppose that the weak derivatives $D_w^\alpha f$ exists for all $|\alpha| \leq k$. Define the **Sobolev norm**

$$\|f\|_{W_p^k(\Omega)} := \left(\sum_{|\alpha| \leq k} \|D_w^\alpha f\|_{L^p(\Omega)}^p \right)^{1/p} \quad (4.107)$$

in the case $1 \leq p < \infty$, and in the case $p = \infty$

$$\|f\|_{W_\infty^k(\Omega)} := \max_{|\alpha| \leq k} \|D_w^\alpha f\|_{L^\infty(\Omega)}. \quad (4.108)$$

In either case, we define the **Sobolev spaces** via

$$W_p^k(\Omega) := \left\{ f \in L_{loc}^1(\Omega) : \|f\|_{W_p^k(\Omega)} < \infty \right\}. \quad (4.109)$$

Definition 4.4 (Seminorm) For k a non-negative integer and $f \in W_p^k(\Omega)$, let

$$|f|_{W_p^k(\Omega)} = \left(\sum_{|\alpha|=k} \|D_w^\alpha f\|_{L^p(\Omega)}^p \right)^{1/p} \quad (4.110)$$

in the case $1 \leq p < \infty$, and in the case $p = \infty$

$$|f|_{W_\infty^k(\Omega)} = \max_{|\alpha|=k} \|D_w^\alpha f\|_{L^\infty(\Omega)}. \quad (4.111)$$

The space $W_2^m(\partial\Omega) = H^m(\partial\Omega)$ can be introduced for the boundary $\partial\Omega$. In case of $m = 1/2$, the space $H^m(\partial\Omega)$ is equipped with a norm [40]

$$\|\mathbf{s}\|_{H^{1/2}(\partial\Omega)}^2 = \|\mathbf{s}\|_{L^2(\partial\Omega)}^2 + |\mathbf{s}|_{1/2, \partial\Omega}^2 \quad (4.112)$$

where

$$|\mathbf{s}|_{1/2, \partial\Omega}^2 = \int_{\partial\Omega} |x - y|^{-(n+1)} |\mathbf{s}(x) - \mathbf{s}(y)|^2 dx dy \quad (4.113)$$

and n is the dimensional number.

The following theorems are important to prove the existence and uniqueness of the weak solutions. The proofs are in the citations referred below. The first theorem is referred to as the inverse trace theorem and it ensures that if $s \in H^{1/2}(\partial\Omega)$, then there exists $\mathbf{v}_s \in H^1(\Omega)$ such that the trace of \mathbf{v}_s on $\partial\Omega$ is \mathbf{s} , [40].

Theorem 4.5 (Direct and Inverse Trace Theorem for $H^1(\Omega)$) There exist positive constants K and K' such that, for each $\mathbf{w} \in H^1(\Omega)$, its trace on $\partial\Omega$ belongs to $H^{1/2}(\partial\Omega)$ and $\|\mathbf{w}\|_{H^{1/2}(\partial\Omega)} \leq K \|\mathbf{w}\|_{H^1(\Omega)}$. Conversely, for each given function $\mathbf{s} \in H^{1/2}(\partial\Omega)$, there exists a function $\mathbf{v}_s \in H^1(\Omega)$ such that its trace on $\partial\Omega$ coincides with \mathbf{s} and

$$\|\mathbf{v}_s\|_{H^1(\Omega)} \leq K' \|\mathbf{s}\|_{H^{1/2}(\partial\Omega)}. \quad (4.114)$$

The next theorem states that the divergence operator is an isomorphism between $L_0^2(\Omega)$ and V^\perp [44], and the Ladyzhenskaya-Babuška-Brezzi, LBB, condition, which is needed for the stability of the mixed finite element method, is mentioned [24].

Theorem 4.6 *Let Ω be connected. Then*

1) *the operator **grad** is an isomorphism of $L_0^2(\Omega)$ onto V^0*

2) *the operator **div** is an isomorphism of V^\perp onto $L_0^2(\Omega)$*

Moreover, there exists $\beta > 0$ such that

$$\inf_{q \in L_0^2(\Omega)} \sup_{\mathbf{w} \in H_0^1(\Omega)} \frac{b(\mathbf{w}, q)}{\|\mathbf{w}\|_{H^1(\Omega)} \|q\|_{L^2(\Omega)}} \geq \beta > 0 \quad (4.115)$$

and for any $q \in L_0^2(\Omega)$, there exists a unique $\mathbf{v} \in V^\perp \subset H_0^1(\Omega)$ satisfying

$$\|\mathbf{v}\|_{H^1(\Omega)} \leq \beta^{-1} \|q\|_{L^2(\Omega)}. \quad (4.116)$$

To prove the existence and uniqueness, Lax-Milgram is the main theorem used in the proof. We begin with some definitions [23].

Definition 4.7 *A bilinear form $a(\cdot, \cdot)$ on a normed linear space H is said to be **bounded** (or **continuous**) if $\exists C < \infty$ such that*

$$|a(v, w)| \leq C \|v\|_H \|w\|_H \quad \forall v, w \in H \quad (4.117)$$

*and **coercive** on $E \subset H$ if $\exists \alpha > 0$ such that*

$$a(v, v) \geq \alpha \|v\|_H^2 \quad \forall v \in E. \quad (4.118)$$

In order to prove the existence and uniqueness of Problem (4.1), we require operator notations. Recall that $(L_0^2(\Omega))' = L_0^2(\Omega)$ and $(H_0^1(\Omega))' = H^{-1}(\Omega)$ where $(L_0^2(\Omega))'$ and $(H_0^1(\Omega))'$ are the dual spaces of $L_0^2(\Omega)$ and $H^{-1}(\Omega)$, respectively.

Definition 4.8 *Let $\mathbf{v}, \mathbf{w} \in H^1(\Omega)$ and $q \in L_0^2(\Omega)$. Define linear operators $A : H_0^1(\Omega) \rightarrow H^{-1}(\Omega)$ or $A \in \mathcal{L}(H_0^1(\Omega); H^{-1}(\Omega))$ and $B \in \mathcal{L}(H_0^1(\Omega); L_0^2(\Omega))$ by*

$$\langle A\mathbf{v}, \mathbf{w} \rangle_{H_0^1(\Omega) \times H^{-1}(\Omega)} := a(\mathbf{v}, \mathbf{w}) \quad \forall \mathbf{v}, \mathbf{w} \in H_0^1(\Omega) \quad (4.119)$$

$$\langle B\mathbf{v}, q \rangle_{H_0^1(\Omega) \times L_0^2(\Omega)} := b(\mathbf{v}, q) \quad \forall \mathbf{v} \in H_0^1(\Omega), \forall q \in L_0^2(\Omega) \quad (4.120)$$

Let $B' \in \mathcal{L}(L_0^2(\Omega); H^{-1}(\Omega))$ be the dual operator of B , i.e.

$$\langle B'q, \mathbf{v} \rangle = \langle q, B\mathbf{v} \rangle := b(\mathbf{v}, q) \quad \forall \mathbf{v} \in H_0^1(\Omega), \forall q \in L_0^2(\Omega). \quad (4.121)$$

With these operators, Problem (4.1) is equivalently written in the form:

Problem 4.9 Find $\mathbf{v} \in H_s^1(\Omega), p \in L_0^2(\Omega)$ such that

$$A\mathbf{v} + B'p = \mathbf{f} \quad \text{in } H^{-1}(\Omega) \quad (4.122a)$$

$$B\mathbf{v} = f \quad \text{in } L_0^2(\Omega). \quad (4.122b)$$

Next, we introduce Lax-Milgram theorem which is one of the most important theorems used to prove the existence and uniqueness of the weak solution.

Theorem 4.10 (*Lax-Milgram*) Given a Hilbert space $(H, (\cdot, \cdot))$ a continuous, coercive bilinear form $a(\cdot, \cdot)$ and a continuous linear functional $F \in H'$, there exists a unique $v \in H$ such that

$$a(v, w) = F(w) \quad \forall w \in H. \quad (4.123)$$

The following inequalities are applied in the proof of continuities and coercivity, [44, 23]

Theorem 4.11 (*Poincaré inequality*) If Ω is connected and bounded at least in one direction, then for each integer $m \geq 0$, there exists a constant $K = K(m, \Omega) > 0$ such that

$$\|w\|_{H^m(\Omega)} \leq K|w|_{H^m(\Omega)} \quad \forall w \in H_0^m(\Omega), \quad (4.124)$$

or for space $H_0^1(\Omega)$

$$\|w\|_{L^2(\Omega)} \leq K\|\nabla w\|_{L^2(\Omega)} \quad \forall w \in H_0^1(\Omega). \quad (4.125)$$

Theorem 4.12 (*Hölder's Inequality*) For $1 \leq p, q \leq \infty$ such that $1 = 1/p + 1/q$, if $f \in L^p(\Omega)$ and $g \in L^q(\Omega)$, then $fg \in L^1(\Omega)$ and

$$\|fg\|_{L^1(\Omega)} \leq \|f\|_{L^p(\Omega)} \|g\|_{L^q(\Omega)}. \quad (4.126)$$

Theorem 4.13 (*Cauchy-Schwarz's Inequality*) This is simply Hölder's inequality in the special case $p = q = 2$. If $f, g \in L^2(\Omega)$, then $fg \in L^1(\Omega)$ and

$$\int_{\Omega} |f(x)g(x)| dx \leq \|f\|_{L^2(\Omega)} \|g\|_{L^2(\Omega)}. \quad (4.127)$$

for vectors $\mathbf{v}, \mathbf{w} \in L^2(\Omega)$, we also have

$$\int_{\Omega} |\mathbf{v} \cdot \mathbf{w}| \leq \|\mathbf{v}\|_{L^2(\Omega)} \|\mathbf{w}\|_{L^2(\Omega)}. \quad (4.128)$$

We next show that the $L^2(\Omega)$ -norm of divergence of a function in $H^1(\Omega)$ is less than or equal to a multiplication of a constant and the $H^1(\Omega)$ -seminorm of the function and also provide the proof. This theorem will be used to prove Theorem 4.15.

Theorem 4.14 Let $\Omega \subset \mathbb{R}^n$ and $\mathbf{w} \in H^1(\Omega)$. Then

$$\|\nabla \cdot \mathbf{w}\|_{L^2(\Omega)} \leq \sqrt{n} |\mathbf{w}|_{H^1(\Omega)}. \quad (4.129)$$

Proof: Let $u_i = \partial w_i / \partial x_i$ where $\mathbf{w} = (w_1, w_2, \dots, w_n)$. Since $|u_1 + u_2 + \dots, u_n|^2 \leq n(u_1^2 + u_2^2 + \dots + u_n^2)$, integrating and taking square root both sides, we have

$$\sqrt{\int_{\Omega} |u_1 + u_2 + \dots + u_n|^2} \leq \sqrt{n} \sqrt{\int_{\Omega} (u_1^2 + u_2^2 + \dots + u_n^2)}. \quad (4.130)$$

Then $\|\nabla \cdot \mathbf{w}\|_{L^2(\Omega)} \leq \sqrt{n} |\mathbf{w}|_{H^1(\Omega)}$. ■

The following theorems show that the linear functionals $c_1(\mathbf{w})$, $c_2(q)$ and bilinear functionals $a(\cdot, \cdot)$, $b(\cdot, \cdot)$ are continuous and $a(\cdot, \cdot)$ is coercive.

Theorem 4.15 The linear functionals $c_1(\mathbf{w})$, $c_2(q)$ and bilinear functionals $a(\cdot, \cdot)$, $b(\cdot, \cdot)$ are continuous and $a(\cdot, \cdot)$ is coercive, i.e.,

$$a(\mathbf{w}, \mathbf{w}) \geq C_c \|\mathbf{w}\|_{H^1(\Omega)}^2 \quad (4.131)$$

where $C_c = \min\{\mu/\epsilon, \mu C_k\}$; C_k is a positive number. In particular,

$$c_1(\mathbf{w}) \leq (\|\mathbf{f}_1\|_{H^{-1}(\Omega)} + \sqrt{n} \frac{\mu}{\epsilon} \|f\|_{L^2(\Omega)}) \|\mathbf{w}\|_{H^1(\Omega)}, \quad \forall \mathbf{w} \in H^1(\Omega), \quad (4.132)$$

$$c_2(q) \leq \|f\|_{L^2(\Omega)} \|q\|_{L^2(\Omega)}, \quad \forall q \in L^2(\Omega) \quad (4.133)$$

$$b(\mathbf{v}, q) \leq \sqrt{n} |\mathbf{v}|_{H^1(\Omega)} \|q\|_{L^2(\Omega)}, \quad \forall \mathbf{v} \in H^1(\Omega), \quad \forall q \in L^2(\Omega) \quad (4.134)$$

$$a(\mathbf{v}, \mathbf{w}) \leq C_a \|\mathbf{v}\|_{H^1(\Omega)} \|\mathbf{w}\|_{H^1(\Omega)}, \quad \forall \mathbf{v} \in H^1(\Omega), \quad \forall \mathbf{w} \in H^1(\Omega), \quad (4.135)$$

where n is the dimensional number; $C_a = \max\{\mu/\epsilon^l, \sqrt{6}\mu \max_{1 \leq i, j \leq 2} |k_{ij}^{-1}|\}$.

Proof: The linearity of $c_1(\mathbf{w})$ and $c_2(q)$ and bilinearity of $a(\mathbf{v}, \mathbf{w})$ and $b(\mathbf{v}, q)$ are obvious.

Next we show they are continuous. Let $\mathbf{v}, \mathbf{w} \in H^1(\Omega)$ and $q \in L^2(\Omega)$, then

$$|c_1(\mathbf{w})| = |\langle \mathbf{f}_1, \mathbf{w} \rangle_{H^{-1}(\Omega) \times H_0^1(\Omega)} - \int_{\Omega} \frac{\mu}{\epsilon^l} f \nabla \cdot \mathbf{w}| \quad (4.136)$$

$$\leq |\langle \mathbf{f}_1, \mathbf{w} \rangle_{H^{-1}(\Omega) \times H_0^1(\Omega)}| + \left| \int_{\Omega} \frac{\mu}{\epsilon^l} f \nabla \cdot \mathbf{w} \right| \quad (4.137)$$

$$= \left| \frac{\langle \mathbf{f}_1, \mathbf{w} \rangle_{H^{-1}(\Omega) \times H_0^1(\Omega)}}{\|\mathbf{w}\|_{H^1(\Omega)}} \|\mathbf{w}\|_{H^1(\Omega)} \right| + \frac{\mu}{\epsilon^l} \left| \int_{\Omega} f \nabla \cdot \mathbf{w} \right| \quad (4.138)$$

$$\leq \|\mathbf{f}_1\|_{H^{-1}(\Omega)} \|\mathbf{w}\|_{H^1(\Omega)} + \frac{\mu}{\epsilon^l} \|f\|_{L^2(\Omega)} \|\nabla \cdot \mathbf{w}\|_{L^2(\Omega)} \quad (4.139)$$

$$\leq \|\mathbf{f}_1\|_{H^{-1}(\Omega)} \|\mathbf{w}\|_{H^1(\Omega)} + \sqrt{n} \frac{\mu}{\epsilon^l} \|f\|_{L^2(\Omega)} |\mathbf{w}|_{H^1(\Omega)} \quad (4.140)$$

$$\leq (\|\mathbf{f}_1\|_{H^{-1}(\Omega)} + \sqrt{n} \frac{\mu}{\epsilon^l} \|f\|_{L^2(\Omega)}) \|\mathbf{w}\|_{H^1(\Omega)}, \quad (4.141)$$

where we apply the definition of $H^{-1}(\Omega)$ -norm, (4.96), and Cauchy-Schwarz's inequality, Theorem 4.13, for the third inequality. For the fourth inequality we use the fact that $\|\nabla \cdot \mathbf{w}\|_{L^2(\Omega)} \leq \sqrt{n} |\mathbf{w}|_{H^1(\Omega)}$ where $|\cdot|$ is the seminorm and n is the dimensional number. For the continuity of $c_2(q)$, it is obvious that

$$|c_2(q)| = \left| \int_{\Omega} f q \right| \leq \|f\|_{L^2(\Omega)} \|q\|_{L^2(\Omega)}, \quad (4.142)$$

where Cauchy-Schwarz's inequality has been applied. To show continuity of $b(\mathbf{v}, q)$, we have

$$|b(\mathbf{v}, q)| = \left| \int_{\Omega} q \nabla \cdot \mathbf{v} \right| \leq \|q\|_{L^2(\Omega)} \|\nabla \cdot \mathbf{v}\|_{L^2(\Omega)} \leq \sqrt{n} |\mathbf{v}|_{H^1(\Omega)} \|q\|_{L^2(\Omega)}, \quad (4.143)$$

where Cauchy-Schwarz's inequality and the fact that $\|\nabla \cdot \mathbf{w}\|_{L^2(\Omega)} \leq \sqrt{n} |\mathbf{w}|_{H^1(\Omega)}$ are applied for the last two inequalities; n denotes the dimensional number. To prove the continuity of $a(\mathbf{v}, \mathbf{w})$ for a two-dimensional domain, let $\mathbf{v} = (v_1, v_2)$. We first consider

$$\|\mathbf{k}^{-1} \cdot \mathbf{v}\|_{L^2(\Omega)}^2 = \int_{\Omega} (k_{11}^{-1} v_1 + k_{12}^{-1} v_2)^2 + \int_{\Omega} (k_{21}^{-1} v_1 + k_{22}^{-1} v_2)^2$$

$$\begin{aligned}
&\leq \int_{\Omega} (k_{11}^{-1}v_1)^2 + (k_{12}^{-1}v_2)^2 + (k_{21}^{-1}v_1)^2 + (k_{22}^{-1}v_2)^2 \\
&\quad + |2k_{11}^{-1}k_{12}^{-1}v_1v_2| + |2k_{21}^{-1}k_{22}^{-1}v_1v_2| d\Omega \\
&\leq 2 \max_{1 \leq i, j \leq 2} |k_{ij}^{-1}|^2 \int_{\Omega} (2v_1^2 + 2v_2^2 + 2|v_1v_2|) \\
&\leq 4 \max_{1 \leq i, j \leq 2} |k_{ij}^{-1}|^2 \int_{\Omega} \left(v_1^2 + v_2^2 + \frac{|v_1|^2}{2} + \frac{|v_2|^2}{2} \right) \\
&= 2 \max_{1 \leq i, j \leq 2} |k_{ij}^{-1}|^2 \int_{\Omega} (3v_1^2 + 3v_2^2) \\
&= 6 \max_{1 \leq i, j \leq 2} |k_{ij}^{-1}|^2 \int_{\Omega} (v_1^2 + v_2^2) \\
&= 6 \max_{1 \leq i, j \leq 2} |k_{ij}^{-1}|^2 \|\mathbf{v}\|_{L^2(\Omega)}^2, \tag{4.144}
\end{aligned}$$

where Young's inequality $ab \leq a^p/p + b^q/q$ where $a, b \geq 0$, $p, q > 0$ and $1/p + 1/q = 1$ is applied at the third inequality. The proof that $a(\mathbf{v}, \mathbf{w})$ is continuous is completed with the following:

$$|a(\mathbf{v}, \mathbf{w})| = \left| \int_{\Omega} \frac{\mu}{\epsilon^l} \nabla \mathbf{v} : \nabla \mathbf{w} + \int_{\Omega} \mu (\mathbf{k}^{-1} \cdot \mathbf{v}) \cdot \mathbf{w} \right| \tag{4.145}$$

$$\leq \left| \int_{\Omega} \frac{\mu}{\epsilon^l} \nabla \mathbf{v} : \nabla \mathbf{w} \right| + \left| \int_{\Omega} \mu (\mathbf{k}^{-1} \cdot \mathbf{v}) \cdot \mathbf{w} \right| \tag{4.146}$$

$$\leq \frac{\mu}{\epsilon^l} \|\nabla \mathbf{v}\|_{L^2(\Omega)} \|\nabla \mathbf{w}\|_{L^2(\Omega)} + \mu \|\mathbf{k}^{-1} \cdot \mathbf{v}\|_{L^2(\Omega)} \|\mathbf{w}\|_{L^2(\Omega)} \tag{4.147}$$

$$\leq \frac{\mu}{\epsilon^l} \|\nabla \mathbf{v}\|_{L^2(\Omega)} \|\nabla \mathbf{w}\|_{L^2(\Omega)} + \sqrt{6}\mu \max_{1 \leq i, j \leq 2} |k_{ij}^{-1}| \|\mathbf{v}\|_{L^2(\Omega)} \|\mathbf{w}\|_{L^2(\Omega)} \tag{4.148}$$

$$\leq C_a \|\mathbf{v}\|_{H^1(\Omega)} \|\mathbf{w}\|_{H^1(\Omega)} \tag{4.149}$$

where $C_a = \max\{\mu/\epsilon^l, \sqrt{6}\mu \max_{1 \leq i, j \leq 2} |k_{ij}^{-1}|\}$ and (4.144) is employed to the third inequality.

Before proving the coercivity of the bilinear form $a(\mathbf{w}, \mathbf{w})$, we consider, for two-dimensions,

$$(\mathbf{k}^{-1} \cdot \mathbf{w}) \cdot \mathbf{w} = k_{11}^{-1}w_1^2 + k_{22}^{-1}w_2^2 + 2k_{12}^{-1}w_1w_2 \tag{4.150}$$

where $\mathbf{w} = (w_1, w_2)$ and \mathbf{k}^{-1} is symmetric. Note that $(\mathbf{k}^{-1} \cdot \mathbf{w}) \cdot \mathbf{w} = \mathbf{w}^T \mathbf{k}^{-1} \mathbf{w}$ as matrix multiplication where T is the transpose. For our problem \mathbf{k}^{-1} is a positive definite matrix and its diagonal entries are positive numbers. Then $k_{11}^{-1}w_1^2 + k_{22}^{-1}w_2^2 > 0$ when $\mathbf{w} > \mathbf{0}$. We next need to focus on $2k_{12}^{-1}w_1w_2$. If $2k_{12}^{-1}w_1w_2 \geq 0$, it's easy to see that $(\mathbf{k}^{-1} \cdot \mathbf{w}) \cdot \mathbf{w} \geq k_{11}^{-1}w_1^2 + k_{22}^{-1}w_2^2 \geq \min\{k_{11}^{-1}, k_{22}^{-1}\}(w_1^2 + w_2^2) = C_k(w_1^2 + w_2^2)$ where $C_k > 0$. If $2k_{12}^{-1}w_1w_2 < 0$,

we have two cases:

Case 1: $k_{12}^{-1} > 0$ and $w_1 w_2 < 0$.

$$\text{Thus, } (\mathbf{k}^{-1} \cdot \mathbf{w}) \cdot \mathbf{w} = k_{11}^{-1} w_1^2 + k_{22}^{-1} w_2^2 - 2k_{12}^{-1} |w_1 w_2|.$$

We now apply Young's inequality: $ab < a^2/2 + b^2/2$ where $a, b > 0$.

$$\text{Then } |w_1 w_2| = |w_1| |w_2| < |w_1|^2/2 + |w_2|^2/2.$$

$$\begin{aligned} \text{Thus, } k_{11}^{-1} w_1^2 + k_{22}^{-1} w_2^2 - 2k_{12}^{-1} |w_1 w_2| & \\ & > k_{11}^{-1} w_1^2 + k_{22}^{-1} w_2^2 - 2k_{12}^{-1} (|w_1|^2/2 + |w_2|^2/2) \\ & = k_{11}^{-1} w_1^2 + k_{22}^{-1} w_2^2 - k_{12}^{-1} (|w_1|^2 + |w_2|^2) \\ & = (k_{11}^{-1} - k_{12}^{-1}) w_1^2 + (k_{22}^{-1} - k_{12}^{-1}) w_2^2. \end{aligned}$$

For our problem, \mathbf{k}^{-1} is diagonally dominant.

$$\text{Then, } C_k = \min\{(k_{11}^{-1} - k_{12}^{-1}), (k_{22}^{-1} - k_{12}^{-1})\} > 0.$$

$$\text{Therefore, } (\mathbf{k}^{-1} \cdot \mathbf{w}) \cdot \mathbf{w} > C_k (w_1^2 + w_2^2).$$

Case 2: $k_{12}^{-1} < 0$ and $w_1 w_2 > 0$.

Since \mathbf{k}^{-1} is bounded, $\exists C_b$ such that $k_{12}^{-1} = -C_b$ where $C_b > 0$.

$$\begin{aligned} \text{Thus, } (\mathbf{k}^{-1} \cdot \mathbf{w}) \cdot \mathbf{w} & = k_{11}^{-1} w_1^2 + k_{22}^{-1} w_2^2 - 2C_b w_1 w_2 \\ & = k_{11}^{-1} w_1^2 + k_{22}^{-1} w_2^2 - 2C_b |w_1 w_2| = k_{11}^{-1} w_1^2 + k_{22}^{-1} w_2^2 - 2C_b |w_1| |w_2| \end{aligned}$$

We now apply Young's inequality: $|w_1| |w_2| < |w_1|^2/2 + |w_2|^2/2$

$$\begin{aligned} \text{Therefore, } k_{11}^{-1} w_1^2 + k_{22}^{-1} w_2^2 - 2C_b |w_1| |w_2| & \\ & > k_{11}^{-1} w_1^2 + k_{22}^{-1} w_2^2 - 2C_b (|w_1|^2/2 + |w_2|^2/2) \\ & = k_{11}^{-1} w_1^2 + k_{22}^{-1} w_2^2 - C_b (|w_1|^2 + |w_2|^2) \\ & = (k_{11}^{-1} - C_b) w_1^2 + (k_{22}^{-1} - C_b) w_2^2 \\ & \geq \min\{(k_{11}^{-1} - C_b), (k_{22}^{-1} - C_b)\} (w_1^2 + w_2^2) \end{aligned}$$

For our problem, C_b is less than the diagonal entries of \mathbf{k}^{-1} .

$$\text{Thus, } C_k = \min\{(k_{11}^{-1} - C_b), (k_{22}^{-1} - C_b)\} > 0$$

$$\text{Hence, } \exists C_k > 0, (\mathbf{k}^{-1} \cdot \mathbf{w}) \cdot \mathbf{w} > C_k (w_1^2 + w_2^2)$$

From all of the cases above, we have

$$\exists C_k > 0, (\mathbf{k}^{-1} \cdot \mathbf{w}) \cdot \mathbf{w} \geq C_k (w_1^2 + w_2^2) \tag{4.151}$$

Hence,

$$\int_{\Omega} (\mathbf{k}^{-1} \cdot \mathbf{w}) \cdot \mathbf{w} \geq C_k \int_{\Omega} (w_1^2 + w_2^2) = C_k \|\mathbf{w}\|_{L^2(\Omega)}^2. \quad (4.152)$$

We are now ready to show coercivity. We begin with the formula (4.101). Then

$$a(\mathbf{w}, \mathbf{w}) = \int_{\Omega} \frac{\mu}{\epsilon^l} \nabla \mathbf{w} : \nabla \mathbf{w} + \int_{\Omega} \mu (\mathbf{k}^{-1} \cdot \mathbf{w}) \cdot \mathbf{w} \quad (4.153)$$

$$\geq \frac{\mu}{\epsilon^l} \|\nabla \mathbf{w}\|_{L^2(\Omega)}^2 + \mu C_k \|\mathbf{w}\|_{L^2(\Omega)}^2 \quad (4.154)$$

$$\geq C_c \|\mathbf{w}\|_{H^1(\Omega)}^2, \quad (4.155)$$

where $C_c = \min\{\mu/\epsilon, \mu C_k\}$. ■

Next it is necessary to know the following formulation so that it will be used in the proof of the next theorem. Assume that $\mathbf{f}_1 \in H^{-1}(\Omega)$, $\mathbf{s} \in H^{1/2}(\partial\Omega)$ and $f \in L^2(\Omega)$. By the inverse trace theorem 4.5, we have

$$\exists \mathbf{v}_s \in H^1(\Omega) \text{ such that } \mathbf{v}_s|_{\partial\Omega} = \mathbf{s}, \quad (4.156)$$

and

$$\exists K_s > 0 \text{ such that } \|\mathbf{v}_s\|_{H^1(\Omega)} \leq K_s \|\mathbf{s}\|_{H^{1/2}(\partial\Omega)}. \quad (4.157)$$

Therefore, we have the following equalities,

$$\int_{\Omega} f = \int_{\Omega} \nabla \cdot \mathbf{v} = \int_{\partial\Omega} \mathbf{v} \cdot \mathbf{n} = \int_{\partial\Omega} \mathbf{s} \cdot \mathbf{n} = \int_{\partial\Omega} \mathbf{v}_s \cdot \mathbf{n} = \int_{\Omega} \nabla \cdot \mathbf{v}_s, \quad (4.158)$$

where we applied the divergence theorem to the second and last equalities and \mathbf{n} is the unit outward pointing normal of the boundary $\partial\Omega$. The equalities show that

$$\int_{\Omega} (f - \nabla \cdot \mathbf{v}_s) = 0 \quad (4.159)$$

which implies that $f - \nabla \cdot \mathbf{v}_s \in L_0^2(\Omega)$. From Theorem 4.6, then

$$\exists! \mathbf{v}_0 \in V^{\perp} \subset H_0^1(\Omega) \text{ such that } \nabla \cdot \mathbf{v}_0 = f - \nabla \cdot \mathbf{v}_s. \quad (4.160)$$

We now can prove the existence and uniqueness of the Stokes-Brinkman equations.

Theorem 4.16 (*Well-posedness of the Stokes-Brinkman equations*) Assume that $\mathbf{f}_1 \in H^{-1}(\Omega)$, $\mathbf{f}, f \in L^2(\Omega)$ and $\mathbf{s} \in H^{1/2}(\partial\Omega)$. There exists a unique $\mathbf{v} \in H_s^1(\Omega)$, $p \in L_0^2(\Omega)$ satisfying Problem 4.1, equations (4.105). Moreover,

$$\|\mathbf{v}\|_{H^1(\Omega)} \leq \frac{1}{C_c} \left(\|\mathbf{f}_1\|_{H^{-1}(\Omega)} + \sqrt{n} \frac{\mu}{\epsilon} \|f\|_{L^2(\Omega)} \right) + \left(\frac{C_a}{C_c} + 1 \right) \|\hat{\mathbf{v}}\|_{H^1(\Omega)} \quad (4.161)$$

where $\hat{\mathbf{v}} = \mathbf{v}_s + \mathbf{v}_0$ and

$$\|p\|_{L^2(\Omega)} \leq \frac{1}{\beta} \left(\|\mathbf{f}_1\|_{H^{-1}(\Omega)} + \sqrt{n} \frac{\mu}{\epsilon^l} \|f\|_{L^2(\Omega)} \right) + \frac{1}{\beta} C_a \|\mathbf{v}\|_{H^1(\Omega)}. \quad (4.162)$$

where β is the constant in (4.115).

Proof: Let $\mathbf{f}_1 \in H^{-1}(\Omega)$, $\mathbf{f}, f \in L^2(\Omega)$ and $\mathbf{s} \in H^{1/2}(\partial\Omega)$. Let $\hat{\mathbf{v}} = \mathbf{v}_s + \mathbf{v}_0$. For any $\mathbf{w} \in V$, let $F(\mathbf{w}) = c_1(\mathbf{w}) - a(\hat{\mathbf{v}}, \mathbf{w})$. From Theorem 4.15, $c_1(\cdot)$ and $a(\cdot, \cdot)$ are linear and bilinear respectively. Then $F(\cdot)$ is linear. Moreover, the continuities of $c_1(\cdot)$ and $a(\cdot, \cdot)$ implies that $F(\cdot)$ is continuous. By applying the Lax-Milgram Theorem, there exists a unique $\tilde{\mathbf{v}} \in V \subset H_0^1(\Omega)$ such that $a(\tilde{\mathbf{v}}, \mathbf{w}) = F(\mathbf{w})$. Let $\mathbf{v} = \tilde{\mathbf{v}} + \hat{\mathbf{v}} = \tilde{\mathbf{v}} + \mathbf{v}_s + \mathbf{v}_0$. Therefore, $\mathbf{v}|_{\partial\Omega} = \tilde{\mathbf{v}}|_{\partial\Omega} + \mathbf{v}_s|_{\partial\Omega} + \mathbf{v}_0|_{\partial\Omega} = 0 + \mathbf{s} + 0 = \mathbf{s}$ because $\mathbf{v}_0 \in V^\perp \subset H_0^1(\Omega)$, and $\tilde{\mathbf{v}} \in V \subset H_0^1(\Omega)$. Moreover, $\nabla \cdot \mathbf{v} = \nabla \cdot \tilde{\mathbf{v}} + \nabla \cdot \mathbf{v}_s + \nabla \cdot \mathbf{v}_0 = 0 + \nabla \cdot \mathbf{v}_s + f - \nabla \cdot \mathbf{v}_s = f$ since $\tilde{\mathbf{v}} \in V$ and $\nabla \cdot \mathbf{v}_0 = f - \nabla \cdot \mathbf{v}_s$, (4.160). Therefore, \mathbf{v} is in $H_s^1(\Omega)$ and satisfies the continuity equation. To show that \mathbf{v} is unique, we apply the coercivity of $a(\cdot, \cdot)$. Since $a(\tilde{\mathbf{v}}, \mathbf{w}) = F(\mathbf{w}) = c_1(\mathbf{w}) - a(\hat{\mathbf{v}}, \mathbf{w})$ and $\mathbf{v} = \tilde{\mathbf{v}} + \hat{\mathbf{v}}$, $a(\mathbf{v}, \mathbf{w}) = c_1(\mathbf{w})$. Let \mathbf{v}_1 and \mathbf{v}_2 satisfy $a(\mathbf{v}_1, \mathbf{w}) = c_1(\mathbf{w})$ and $a(\mathbf{v}_2, \mathbf{w}) = c_1(\mathbf{w})$. Then $a(\mathbf{v}_1 - \mathbf{v}_2, \mathbf{w}) = 0$ for any $\mathbf{w} \in V$. Thus, $a(\mathbf{v}_1 - \mathbf{v}_2, \mathbf{v}_1 - \mathbf{v}_2) = 0$. Therefore, $0 = a(\mathbf{v}_1 - \mathbf{v}_2, \mathbf{v}_1 - \mathbf{v}_2) \geq C_c \|\mathbf{v}_1 - \mathbf{v}_2\|_{H^1(\Omega)}^2 \geq 0$. Since, $C_c > 0$, $\|\mathbf{v}_1 - \mathbf{v}_2\|_{H^1(\Omega)} = 0$. Then $\mathbf{v}_1 = \mathbf{v}_2$ in the $H^1(\Omega)$ -norm. Hence, there exists a unique \mathbf{v} such that $a(\mathbf{v}, \mathbf{w}) = c_1(\mathbf{w})$ for all $\mathbf{w} \in V$.

Next, we show that there exists $p \in L_0^2(\Omega)$ satisfying Problem 4.1 or 4.9. Let $\langle F_1, \mathbf{w} \rangle = c_1(\mathbf{w})$. Since $a(\tilde{\mathbf{v}}, \mathbf{w}) = c_1(\mathbf{w}) - a(\hat{\mathbf{v}}, \mathbf{w})$, $c_1(\mathbf{w}) - a(\tilde{\mathbf{v}}, \mathbf{w}) - a(\hat{\mathbf{v}}, \mathbf{w}) = 0$ or in operator notation $F_1 - A\tilde{\mathbf{v}} - A\hat{\mathbf{v}} = 0$, by Definition 4.8. Then $F_1 - A\tilde{\mathbf{v}} - A\hat{\mathbf{v}} \in V^0$. Let $B' = \nabla : L_0^2(\Omega) \rightarrow V^0$. From Theorem (4.6) and the isomorphic property, there exists a unique $p \in L_0^2(\Omega)$ such that

$B'p = F_1 - A\tilde{\mathbf{v}} - A\hat{\mathbf{v}} = F_1 - A\mathbf{v}$ or $A\mathbf{v} + B'p = F_1$. Hence, there exists a unique $\mathbf{v} \in H_s^1(\Omega)$ and $p \in L_0^2(\Omega)$ satisfying Problem 4.1.

In order to prove (4.161), we first consider $\|\mathbf{v}_0\|_{H^1(\Omega)}$. Using $f - \nabla \cdot \mathbf{v}_s \in L_0^2(\Omega)$ and applying equations (4.160) and (4.116), we have

$$\begin{aligned} \|\mathbf{v}_0\|_{H^1(\Omega)} &\leq \beta^{-1} \|f - \nabla \cdot \mathbf{v}_s\|_{L^2(\Omega)} \\ &\leq \beta^{-1} (\|f\|_{L^2(\Omega)} + \|\nabla \cdot \mathbf{v}_s\|_{L^2(\Omega)}) \\ &\leq \beta^{-1} (\|f\|_{L^2(\Omega)} + \sqrt{n} \|\mathbf{v}_s\|_{H^1(\Omega)}) \\ &\leq \beta^{-1} (\|f\|_{L^2(\Omega)} + \sqrt{n} C_s \|\mathbf{s}\|_{H^{1/2}(\partial\Omega)}), \end{aligned} \quad (4.163)$$

where Theorem 4.14 is applied to the third inequality and Theorem 4.5 is applied to the fourth inequality. Then

$$\begin{aligned} \|\hat{\mathbf{v}}\|_{H^1(\Omega)} &= \|\mathbf{v}_s + \mathbf{v}_0\|_{H^1(\Omega)} \\ &\leq C_s \|\mathbf{s}\|_{H^{1/2}(\partial\Omega)} + \beta^{-1} (\|f\|_{L^2(\Omega)} + \sqrt{n} C_s \|\mathbf{s}\|_{H^{1/2}(\partial\Omega)}) \\ &= \beta^{-1} \|f\|_{L^2(\Omega)} + (1 + \sqrt{n} \beta^{-1}) C_s \|\mathbf{s}\|_{H^{1/2}(\partial\Omega)}. \end{aligned} \quad (4.164)$$

Next, we apply the coercivity of $a(\cdot, \cdot)$ to obtain a bound for $\tilde{\mathbf{v}}$:

$$\begin{aligned} C_c \|\tilde{\mathbf{v}}\|_{H^1(\Omega)}^2 &\leq a(\tilde{\mathbf{v}}, \tilde{\mathbf{v}}) = c_1(\tilde{\mathbf{v}}) - a(\hat{\mathbf{v}}, \tilde{\mathbf{v}}) \\ &\leq (\|\mathbf{f}_1\|_{H^{-1}(\Omega)} + \sqrt{n} \frac{\mu}{\epsilon} \|f\|_{L^2(\Omega)}) \|\tilde{\mathbf{v}}\|_{H^1(\Omega)} + C_a \|\hat{\mathbf{v}}\|_{H^1(\Omega)} \|\tilde{\mathbf{v}}\|_{H^1(\Omega)}, \end{aligned} \quad (4.165)$$

where Theorem 4.15 is applied to the second inequality. Dividing both sides by $C_c \|\tilde{\mathbf{v}}\|_{H^1(\Omega)}$, we have

$$\|\tilde{\mathbf{v}}\|_{H^1(\Omega)} \leq \frac{1}{C_c} \left(\|\mathbf{f}_1\|_{H^{-1}(\Omega)} + \sqrt{n} \frac{\mu}{\epsilon} \|f\|_{L^2(\Omega)} \right) + \frac{C_a}{C_c} \|\hat{\mathbf{v}}\|_{H^1(\Omega)}.$$

Using (4.165), we have

$$\begin{aligned} \|\mathbf{v}\|_{H^1(\Omega)} &= \|\tilde{\mathbf{v}} + \hat{\mathbf{v}}\|_{H^1(\Omega)} \\ &\leq \frac{1}{C_c} \left(\|\mathbf{f}_1\|_{H^{-1}(\Omega)} + \sqrt{n} \frac{\mu}{\epsilon} \|f\|_{L^2(\Omega)} \right) + \frac{C_a}{C_c} \|\hat{\mathbf{v}}\|_{H^1(\Omega)} + \|\hat{\mathbf{v}}\|_{H^1(\Omega)} \end{aligned}$$

$$= \frac{1}{C_c} \left(\|\mathbf{f}_1\|_{H^{-1}(\Omega)} + \sqrt{n} \frac{\mu}{\epsilon} \|f\|_{L^2(\Omega)} \right) + \left(\frac{C_a}{C_c} + 1 \right) \|\hat{\mathbf{v}}\|_{H^1(\Omega)}. \quad (4.166)$$

Next, we employ condition (4.115) to obtain a bound for pressure p :

$$\|p\|_{L^2(\Omega)}^{-1} \sup_{\mathbf{w} \in H_0^1(\Omega)} \frac{b(\mathbf{w}, p)}{\|\mathbf{w}\|_{H^1(\Omega)}} = \sup_{\mathbf{w} \in H_0^1(\Omega)} \frac{b(\mathbf{w}, p)}{\|\mathbf{w}\|_{H^1(\Omega)} \|p\|_{L^2(\Omega)}} \geq \beta > 0. \quad (4.167)$$

Rearranging we have

$$\|p\|_{L^2(\Omega)} \leq \beta^{-1} \sup_{\mathbf{w} \in H_0^1(\Omega)} \frac{b(\mathbf{w}, p)}{\|\mathbf{w}\|_{H^1(\Omega)}}. \quad (4.168)$$

Note that

$$\begin{aligned} b(\mathbf{w}, p) &= c_1(\mathbf{w}) - a(\mathbf{v}, \mathbf{w}) \\ &\leq \left(\|\mathbf{f}_1\|_{H^{-1}(\Omega)} + \sqrt{n} \frac{\mu}{\epsilon} \|f\|_{L^2(\Omega)} \right) \|\mathbf{w}\|_{H^1(\Omega)} + C_a \|\mathbf{v}\|_{H^1(\Omega)} \|\mathbf{w}\|_{H^1(\Omega)}. \end{aligned} \quad (4.169)$$

Substituting (4.169) into (4.168), we obtain

$$\begin{aligned} \|p\|_{L^2(\Omega)} &\leq \beta^{-1} \sup_{\mathbf{w} \in H_0^1(\Omega)} \left(\|\mathbf{f}_1\|_{H^{-1}(\Omega)} + \sqrt{n} \frac{\mu}{\epsilon} \|f\|_{L^2(\Omega)} + C_a \|\mathbf{v}\|_{H^1(\Omega)} \right) \|\mathbf{w}\|_{H^1(\Omega)} \\ &= \beta^{-1} \left(\|\mathbf{f}_1\|_{H^{-1}(\Omega)} + \sqrt{n} \frac{\mu}{\epsilon} \|f\|_{L^2(\Omega)} \right) + C_a \beta^{-1} \|\mathbf{v}\|_{H^1(\Omega)}, \end{aligned} \quad (4.170)$$

and we have complete the proof of the well-posedness of the Stokes-Brinkman equations, Theorem 4.16. ■

We now have a system of equations:

$$\mu \mathbf{k}^{-1} \cdot (\epsilon^l \mathbf{v}^l - \epsilon^l \mathbf{v}^s) + \nabla p - \frac{\mu}{\epsilon^l} \nabla \cdot (2\epsilon^l \mathbf{d}^l) = \rho \mathbf{g}, \quad \text{in } \Omega \quad (4.171)$$

$$\epsilon^l + (1 - \epsilon^l) \nabla \cdot (\epsilon^l (\mathbf{v}^l - \mathbf{v}^s)) = 0 \quad \text{in } \Omega \quad (4.172)$$

$$\mathbf{v}^l = \mathbf{s} \quad \text{on } \partial\Omega, \quad (4.173)$$

which are well-posed for a fixed numerical domain Ω and boundary conditions defined by the function $\mathbf{s} \in H^{1/2}(\partial\Omega)$.

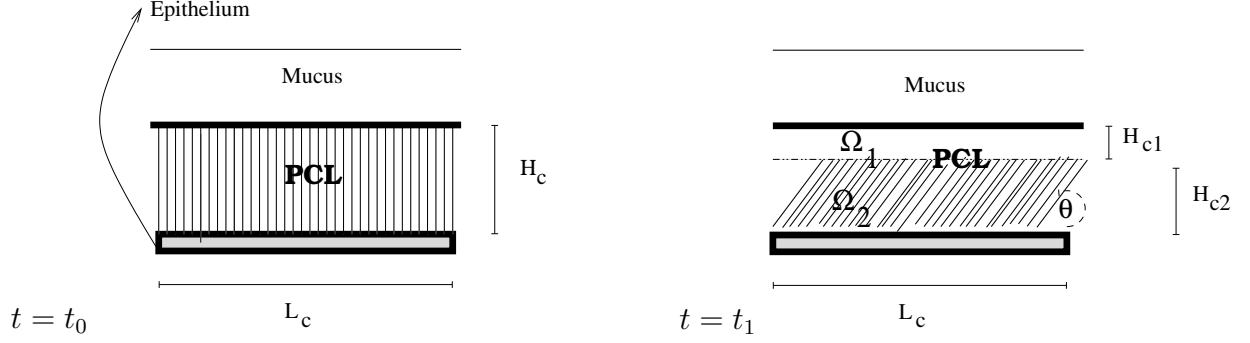


Figure 5.1: The left figures shows the PCL when $t = t_0$ where the cilia is perpendicular to the horizontal plan while the right one displays the PCL when $t = t_1$ where the cilia make an angle θ to the horizontal plan, where θ is less than 90 degrees.

5. NUMERICAL RESULTS FOR THE FIXED HEIGHT MODEL, TWO-DIMENSIONAL MODEL

In this Chapter, we apply a mixed finite element method to the system of the Stokes-Brinkman equations and the continuity equation:

$$\mu \mathbf{k}^{-1} \cdot (\epsilon^l \mathbf{v}^l - \epsilon^l \mathbf{v}^s) + \nabla p - \frac{\mu}{\epsilon^l} \nabla \cdot (2\epsilon^l \mathbf{d}^l) = \rho \mathbf{g}, \quad \text{in } \Omega_1 \cup \Omega_2 \quad (5.1)$$

$$\dot{\epsilon}^l + (1 - \epsilon^l) \nabla \cdot (\epsilon^l (\mathbf{v}^l - \mathbf{v}^s)) = 0. \quad \text{in } \Omega_1 \cup \Omega_2 \quad (5.2)$$

where the Stokes equation is applied in domain $\Omega_1(t)$ while the Brinkman equation is employed in $\Omega_2(t)$. Figure 5.1 shows the domains. The left one represents the domain when the cilia are perpendicular to the horizontal plane at time $t = t_0$. In this case, we have only porous medium, Ω_2 , in the PCL so only the Brinkman equation is applied. The right figure shows the PCL when the cilia make an angle θ to the horizontal plane at time $t = t_1$. In this study the angle θ is between $\arctan(0.5)$ to $\arctan(\infty)$ or about 26 to 90 degrees. Whenever the angle θ is less than 90° , both subdomains, Ω_1 and Ω_2 , have nonzero areas and the Stokes-Brinkman equations are applied. The boundary conditions for the domains are discussed in Section 5.1. The variational formulation and the model discretization are presented in Section 5.2, while the numerical results and the validation are provided in Section 5.3.

5.1 Boundary Conditions

In this section, appropriately physically meaningful boundary conditions that also guarantee the existence of a unique solution are discussed. To be well-posed either velocity or the traction vector $(\mathbf{t} \cdot \mathbf{n})$ must be prescribed everywhere on the boundary. Furthermore, for a two-dimensional domain, we need two scalar equations at each boundary for the velocity [11]. For the pressure, we consider the bilinear functional (4.102):

$$b(\mathbf{w}, p) = - \int_{\Omega} p \nabla \cdot \mathbf{w} \quad (5.3)$$

$$\begin{aligned} &= \int_{\Omega} \mathbf{w} \cdot \text{grad } p \, d\Omega - \int_{\Gamma} \mathbf{w} p \cdot \mathbf{n} d\Gamma \\ &= \int_{\Omega} \mathbf{w} \cdot \text{grad } p \, d\Omega \end{aligned} \quad (5.4)$$

where we use Green's first identity to get the second equality and \mathbf{w} is in $H_0^1(\Omega)$ so it is zero on the boundary. This implies that $b(\mathbf{w}, p)$ does not change if we add a constant function to p . Note that (5.1) only determines pressure up to an additive constant. This constant is usually fixed by enforcing the normalization [21]

$$\int_{\Omega} p \, d\Omega = 0. \quad (5.5)$$

We divide the boundary into five pieces: the free-fluid/porous-medium interface, $\overline{\Omega}_1 \cap \overline{\Omega}_2$, the free-fluid/fluid interface between the PCL and mucous layer at the top of $\Omega_1 \cup \Omega_2$, the left and right sides of $\Omega_1 \cup \Omega_2$ and the bottom of the PCL, to be able to solve the systems of equations numerically. On the sides, we assume periodicity for both velocities and pressure. The velocities are assumed zero at the bottom.

Let us first consider the boundary conditions at the free-fluid/porous-medium interface. Many authors [3, 47, 62] who use the Darcy equation in Ω_2 and the Stokes equation in Ω_1 apply the Beavers-Joseph condition [8] which states that the velocity component parallels to the interface can slip according to

$$\frac{du^v}{dx_2} = \frac{\alpha_m}{\sqrt{k}} (u_{slip}^v - u^p), \quad (5.6)$$

where α_m is a material dependent, dimensionless, parameter; k is the permeability; u^v and u^p are the velocities of the viscous and porous flows, respectively and u_{slip}^v is the slip velocity depending on the structure of permeable material within the boundary region, height of the domain and fluid viscosity. The difference of the tangential components of the velocities in (5.6) is the jump due to a nominal boundary layer at the interface. Recall that in Darcy's law there is no viscous term, $2\mu\mathbf{d}^l = 0$, which is the deviatoric part of the stress tensor. As a result there is not a natural way to balance the shear stresses. The Beavers-Joseph boundary condition provides a transition model from the viscous to the porous flows [43, 46, 75, 88]. If the porosity is closed to one at the interface, the viscous stress in the viscous flow is completely transferred to the fluid in the porous media.

Alternately, if one uses the Brinkman equation in Ω_2 and the Stokes equation in Ω_1 , the deviatoric part of the stress tensors can be considered. For this case, both continuous and discontinuous shear stress boundary conditions have been considered [39, 68]. We first assume continuity of the normal component of stress, i.e.

$$\mathbf{t}^l \cdot \mathbf{n}|_1 = \mathbf{t}^l \cdot \mathbf{n}|_2, \quad (5.7)$$

where $\mathbf{t}^l = -p\mathbf{I} + 2\mu\mathbf{d}^l$. We also need to conserve mass across the interface (mass flux must be equal) [11]:

$$\rho\mathbf{v}^l \cdot \mathbf{n}|_1 = \rho\mathbf{v}^l \cdot \mathbf{n}|_2 \quad (5.8)$$

where the subscripts 1 and 2 refer to the domain Ω_1 and Ω_2 , respectively and \mathbf{n} is the unit normal vector pointing outward of the boundary. If the normal component of the velocity is continuous across the interface, we automatically have (5.8).

For the top boundary condition we first consider the shear stress. Instead of mucus, air is first assumed at the top of PCL. Therefore the boundary condition on the top of Ω_1 is

$$t_{12} = t_{21} = 2\mu\mathbf{d}^l = \mu\left(\frac{\partial v_1^l}{\partial x_2} + \frac{\partial v_2^l}{\partial x_1}\right) = 0 \quad (5.9)$$

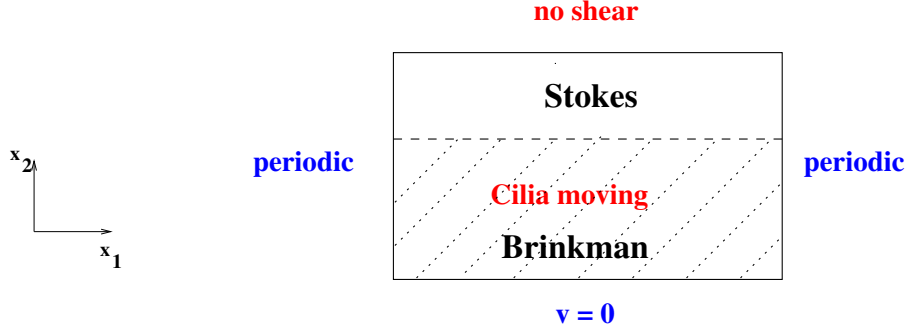


Figure 5.2: A two dimensional Cartesian coordinate system with axis lines x_1 and x_2 and the cartoon picture of the cilia in the PCL with boundary conditions.

where $\mathbf{v}^l = (v_1^l, v_2^l)$. The equation (5.9) can be rewritten as

$$\frac{\partial v_1^l}{\partial x_2} = -\frac{\partial v_2^l}{\partial x_1}. \quad (5.10)$$

Since we assume that the vertical velocity is zero at this interface,

$$\frac{\partial v_1^l}{\partial x_2} = \frac{\partial v_2^l}{\partial x_1} = 0. \quad (5.11)$$

Hence, our initial model as shown in Figure 6.2 is

$$\mu \mathbf{k}^{-1} \cdot (\epsilon^l \mathbf{v}^l - \epsilon^l \mathbf{v}^s) + \nabla p - \frac{\mu}{\epsilon^l} \nabla \cdot (2\epsilon^l \mathbf{d}^l) = \rho \mathbf{g}, \quad \text{in } \Omega_1 \cup \Omega_2 \quad (5.12)$$

$$\epsilon^l + (1 - \epsilon^l) \nabla \cdot (\epsilon^l (\mathbf{v}^l - \mathbf{v}^s)) = 0. \quad \text{in } \Omega_1 \cup \Omega_2 \quad (5.13)$$

$$\mathbf{v}^l = 0 \quad \text{at the bottom of } \Omega_2 \quad (5.14)$$

$$\mathbf{v}^l \text{ and } p \text{ are periodic} \quad \text{on the sides} \quad (5.15)$$

$$\mathbf{v}^l \text{ is continuous} \quad \text{at } \overline{\Omega_1} \cap \overline{\Omega_2} \quad (5.16)$$

$$\frac{dv_1^l}{dx_2} = \frac{dv_2^l}{dx_1} = 0 \quad \text{on the top of } \Omega_1. \quad (5.17)$$

5.2 Model Discretization

The appropriate discretization of the governing equations is the first step to obtain a numerical solution using the mixed finite element method. We begin by deriving the weak formulation of the Stokes-Brinkman equations (5.12)-(5.13) which are equivalent to (5.1)

and (5.2): Find $(\mathbf{v}, p) \in H^1(\Omega) \times L_0^2(\Omega)$ such that

$$\mu \mathbf{k}^{-1} \cdot \mathbf{v} + \nabla p - \frac{\mu}{\epsilon^l} \Delta \mathbf{v} = \rho \mathbf{g} + \mu \mathbf{k}^{-1} \cdot \epsilon^l \mathbf{v}^s + \frac{\mu}{\epsilon^l} \nabla f \quad (5.18)$$

$$\nabla \cdot \mathbf{v} = f, \quad (5.19)$$

with the boundary conditions (5.14)-(5.17) where $f = -\epsilon^l/(1 - \epsilon^l) + \nabla \cdot \epsilon^l \mathbf{v}^s$ and Ω is a computational domain. Note that every term on the right hand side of (5.18) is given since the velocity of the cilia or solid phase is known, see e.g. [20]. Writing (5.18) as scalar equations in two-dimensions gives:

$$\mu [k_{11}^{-1} v_1 + k_{12}^{-1} v_2] - \frac{\mu}{\epsilon^l} \left[\frac{\partial^2 v_1}{\partial x_1^2} + \frac{\partial^2 v_1}{\partial x_2^2} \right] + \frac{\partial p}{\partial x_1} = \mu \epsilon^l [k_{11}^{-1} v_1^s + k_{12}^{-1} v_2^s] + \frac{\mu}{\epsilon^l} \frac{\partial f}{\partial x_1}, \quad (5.20)$$

$$\mu [k_{21}^{-1} v_1 + k_{22}^{-1} v_2] - \frac{\mu}{\epsilon^l} \left[\frac{\partial^2 v_2}{\partial x_1^2} + \frac{\partial^2 v_2}{\partial x_2^2} \right] + \frac{\partial p}{\partial x_2} = -\rho g + \mu \epsilon^l [k_{21}^{-1} v_1^s + k_{22}^{-1} v_2^s] + \frac{\mu}{\epsilon^l} \frac{\partial f}{\partial x_2}, \quad (5.21)$$

where gravity is given by $\mathbf{g} = (0, -g)$. To find the weak formulation, we multiply (5.20)-(5.21) by test functions $w_i \in H_0^1(\Omega)$, $i = 1, 2$ and integrate over the domain $\Omega = \Omega_1 \cup \Omega_2$.

This yields

$$\begin{aligned} & \int_{\Omega} \left(\mu [k_{11}^{-1} v_1 + k_{12}^{-1} v_2] - \frac{\mu}{\epsilon^l} \left[\frac{\partial^2 v_1}{\partial x_1^2} + \frac{\partial^2 v_1}{\partial x_2^2} \right] + \frac{\partial p}{\partial x_1} \right) w_1 d\Omega \\ &= \int_{\Omega} \left(\mu \epsilon^l [k_{11}^{-1} v_1^s + k_{12}^{-1} v_2^s] + \frac{\mu}{\epsilon^l} \frac{\partial f}{\partial x_1} \right) w_1 d\Omega. \end{aligned} \quad (5.22)$$

$$\begin{aligned} & \int_{\Omega} \left(\mu [k_{21}^{-1} v_1 + k_{22}^{-1} v_2] - \frac{\mu}{\epsilon^l} \left[\frac{\partial^2 v_2}{\partial x_1^2} + \frac{\partial^2 v_2}{\partial x_2^2} \right] + \frac{\partial p}{\partial x_2} \right) w_2 d\Omega \\ &= \int_{\Omega} \left(-\rho g + \mu \epsilon^l [k_{21}^{-1} v_1^s + k_{22}^{-1} v_2^s] + \frac{\mu}{\epsilon^l} \frac{\partial f}{\partial x_2} \right) w_2 d\Omega. \end{aligned} \quad (5.23)$$

Integrating by parts the pressure term, the second-order term and the source term f , we have the weak formulation: Find $(\mathbf{v}, p) \in H^1(\Omega) \times L_0^2(\Omega)$ such that

$$\begin{aligned} & \int_{\Omega} \mu [k_{11}^{-1} v_1 + k_{12}^{-1} v_2] w_1 d\Omega + \frac{\mu}{\epsilon^l} \int_{\Omega} \left[\frac{\partial v_1}{\partial x_1} \frac{\partial w_1}{\partial x_1} + \frac{\partial v_1}{\partial x_2} \frac{\partial w_1}{\partial x_2} \right] d\Omega \\ & - \int_{\Omega} p \frac{\partial w_1}{\partial x_1} d\Omega = \int_{\Omega} \mu \epsilon^l [k_{11}^{-1} v_1^s + k_{12}^{-1} v_2^s] w_1 d\Omega - \frac{\mu}{\epsilon^l} \int_{\Omega} f \frac{\partial w_1}{\partial x_1} d\Omega \\ & - \int_{\Gamma} p w_1 n_1 d\Gamma + \frac{\mu}{\epsilon^l} \int_{\Gamma} \left[\frac{\partial v_1}{\partial x_1} n_1 + \frac{\partial v_1}{\partial x_2} n_2 \right] w_1 d\Gamma + \frac{\mu}{\epsilon^l} \int_{\Gamma} f w_1 n_1 d\Gamma, \quad \forall w_1 \in H_0^1(\Omega) \end{aligned} \quad (5.24)$$

$$\begin{aligned}
& \int_{\Omega} \mu \left[k_{21}^{-1} v_1 + k_{22}^{-1} v_2 \right] w_2 d\Omega + \frac{\mu}{\epsilon^l} \int_{\Omega} \left[\frac{\partial v_2}{\partial x_1} \frac{\partial w_2}{\partial x_1} + \frac{\partial v_2}{\partial x_2} \frac{\partial w_2}{\partial x_2} \right] d\Omega \\
& - \int_{\Omega} p \frac{\partial w_2}{\partial x_2} d\Omega = \int_{\Omega} \left(-\rho g + \mu \epsilon^l \left[k_{21}^{-1} v_1^s + k_{22}^{-1} v_2^s \right] \right) w_2 d\Omega - \frac{\mu}{\epsilon^l} \int_{\Omega} f \frac{\partial w_2}{\partial x_2} d\Omega \\
& - \int_{\Gamma} p w_2 n_2 d\Gamma + \frac{\mu}{\epsilon^l} \int_{\Gamma} \left[\frac{\partial v_2}{\partial x_1} n_1 + \frac{\partial v_2}{\partial x_2} n_2 \right] w_2 d\Gamma + \frac{\mu}{\epsilon^l} \int_{\Gamma} f w_2 n_2 d\Gamma, \quad \forall w_2 \in H_0^1(\Omega) \quad (5.25)
\end{aligned}$$

where (n_1, n_2) is the outward unit normal vector and Γ is the boundary of the domain Ω .

Let T_h be a triangulation of domain Ω and

$$V_h = \{v \in H^1(\Omega) : v|_K \text{ is quadratic}, \forall K \in T_h\} \quad (5.26)$$

$$H_h = \{q \in L_0^2(\Omega) : q|_K \text{ is linear}, \forall K \in T_h\}. \quad (5.27)$$

be finite-dimensional subspaces of $H^1(\Omega)$ and $L_0^2(\Omega)$, respectively. In finite element method we approximate the solutions $(v_i, p) \in V_h \times H_h$ by letting

$$v_i(\mathbf{x}) = \sum_{m=1}^M \psi_m(\mathbf{x}) v_i^m = \Psi^T \mathbf{V}_i, \quad (5.28)$$

$$p(\mathbf{x}) = \sum_{l=1}^L \phi_l(\mathbf{x}) p_l = \Phi^T \mathbf{P}. \quad (5.29)$$

where ψ_m and ϕ_l are called basis functions while Ψ and Φ are their vector forms; \mathbf{V}_i and \mathbf{P} are vectors of the velocities and pressure, respectively, and the numbers M and L are determined by the interpolation function. For example, for a tetrahedral element, $M = 10$ for quadratic function for v_i and $L = 4$ for linear function for p . Substituting (5.28) and (5.29) into (5.24) and (5.25) and the basis function Ψ into w_1 and w_2 , we have

$$\begin{aligned}
& \mu \left[\int_{\Omega} k_{11}^{-1} \Psi \Psi^T d\Omega \mathbf{V}_1 + \int_{\Omega} k_{12}^{-1} \Psi \Psi^T d\Omega \mathbf{V}_2 \right] + \frac{\mu}{\epsilon^l} \left[\left(\int_{\Omega} \frac{\partial \Psi}{\partial x_1} \frac{\partial \Psi^T}{\partial x_1} d\Omega + \int_{\Omega} \frac{\partial \Psi}{\partial x_2} \frac{\partial \Psi^T}{\partial x_2} d\Omega \right) \mathbf{V}_1 \right] \\
& - \int_{\Omega} \frac{\partial \Psi}{\partial x_1} \Phi^T d\Omega \mathbf{P} = \mu \epsilon^l \left[\left(\int_{\Omega} \left(k_{11}^{-1} v_1^s + k_{12}^{-1} v_2^s \right) \Psi d\Omega \right) \right] - \frac{\mu}{\epsilon^l} \int_{\Omega} f \frac{\partial \Psi}{\partial x_1} d\Omega \\
& - \int_{\Gamma} \Psi \Phi^T n_1 d\Gamma \mathbf{P} + \frac{\mu}{\epsilon^l} \left[\left(\int_{\Gamma} \Psi \frac{\partial \Psi^T}{\partial x_1} n_1 d\Gamma + \int_{\Gamma} \Psi \frac{\partial \Psi^T}{\partial x_2} n_2 d\Gamma \right) \mathbf{V}_1 \right] + \frac{\mu}{\epsilon^l} \int_{\Gamma} f \Psi n_1 d\Gamma, \quad (5.30) \\
& \mu \left[\int_{\Omega} k_{21}^{-1} \Psi \Psi^T d\Omega \mathbf{V}_1 + \int_{\Omega} k_{22}^{-1} \Psi \Psi^T d\Omega \mathbf{V}_2 \right] + \frac{\mu}{\epsilon^l} \left[\left(\int_{\Omega} \frac{\partial \Psi}{\partial x_1} \frac{\partial \Psi^T}{\partial x_1} d\Omega + \int_{\Omega} \frac{\partial \Psi}{\partial x_2} \frac{\partial \Psi^T}{\partial x_2} d\Omega \right) \mathbf{V}_2 \right] \\
& - \int_{\Omega} \frac{\partial \Psi}{\partial x_2} \Phi^T d\Omega \mathbf{P} = \left[\int_{\Omega} \left(-\rho g + \mu \epsilon^l \left(k_{21}^{-1} v_1^s + k_{22}^{-1} v_2^s \right) \right) \Psi d\Omega \right] - \frac{\mu}{\epsilon^l} \int_{\Omega} f \frac{\partial \Psi}{\partial x_2} d\Omega
\end{aligned}$$

$$- \int_{\Gamma} \Psi \Phi^T n_2 d\Gamma \mathbf{P} + \frac{\mu}{\epsilon^l} \left[\left(\int_{\Gamma} \Psi \frac{\partial \Psi^T}{\partial x_1} n_1 d\Gamma + \int_{\Gamma} \Psi \frac{\partial \Psi^T}{\partial x_2} n_2 d\Gamma \right) \mathbf{V}_2 \right] + \frac{\mu}{\epsilon^l} \int_{\Gamma} f \Psi n_2 d\Gamma. \quad (5.31)$$

To form an element matrix for the finite element method in Ω_2 ,

$$\tilde{\mathbf{A}} = \int_{\Omega_2^e} \Psi \Psi^T d\Omega_2^e, \quad \tilde{\mathbf{K}}_{ij} = \int_{\Omega_2^e} \frac{\partial \Psi}{\partial x_i} \frac{\partial \Psi^T}{\partial x_j} d\Omega_2^e \quad \tilde{\mathbf{Q}}_i = \int_{\Omega_2^e} \Phi \frac{\partial \Psi^T}{\partial x_i} d\Omega_2^e, \quad (5.32)$$

$$\begin{aligned} \tilde{\mathbf{F}}_1 = & \mu \epsilon^l \left[\left(\int_{\Omega_2^e} (k_{11}^{-1} v_1^s + k_{12}^{-1} v_2^s) \Psi d\Omega_2^e \right) \right] - \frac{\mu}{\epsilon^l} \int_{\Omega_2^e} f \frac{\partial \Psi}{\partial x_1} d\Omega_2^e \\ & - \int_{\Gamma_2^e} \Psi \Phi^T n_1 d\Gamma_2^e \mathbf{P} + \frac{\mu}{\epsilon^l} \left[\left(\int_{\Gamma_2^e} \Psi \frac{\partial \Psi^T}{\partial x_1} n_1 d\Gamma_2^e + \int_{\Gamma_2^e} \Psi \frac{\partial \Psi^T}{\partial x_2} n_2 d\Gamma_2^e \right) \mathbf{V}_1 \right] \\ & + \frac{\mu}{\epsilon^l} \int_{\Gamma_2^e} f \Psi n_1 d\Gamma_2^e, \end{aligned} \quad (5.33)$$

$$\begin{aligned} \tilde{\mathbf{F}}_2 = & \int_{\Omega_2^e} (-\rho g + \mu \epsilon^l (k_{21}^{-1} v_1^s + k_{22}^{-1} v_2^s)) \Psi d\Omega_2^e - \frac{\mu}{\epsilon^l} \int_{\Omega_2^e} f \frac{\partial \Psi}{\partial x_2} d\Omega_2^e \\ & - \int_{\Gamma_2^e} \Psi \Phi^T n_2 d\Gamma_2^e \mathbf{P} + \frac{\mu}{\epsilon^l} \left[\left(\int_{\Gamma_2^e} \Psi \frac{\partial \Psi^T}{\partial x_1} n_1 d\Gamma_2^e + \int_{\Gamma_2^e} \Psi \frac{\partial \Psi^T}{\partial x_2} n_2 d\Gamma_2^e \right) \mathbf{V}_2 \right] \\ & + \frac{\mu}{\epsilon^l} \int_{\Gamma_2^e} f \Psi n_2 d\Gamma_2^e. \end{aligned} \quad (5.34)$$

where Ω_2^e is the element domain such that $\Omega_2 = \bigcup_e \Omega_2^e$. Then (5.30) and (5.31) become

$$\mu k_{11}^{-1} \tilde{\mathbf{A}} \mathbf{V}_1 + \mu k_{12}^{-1} \tilde{\mathbf{A}} \mathbf{V}_2 + (\mu/\epsilon^l)(\tilde{\mathbf{K}}_{11} + \tilde{\mathbf{K}}_{22}) \mathbf{V}_1 - \tilde{\mathbf{Q}}_1^T \mathbf{P} = \tilde{\mathbf{F}}_1, \quad (5.35)$$

$$\mu k_{21}^{-1} \tilde{\mathbf{A}} \mathbf{V}_1 + \mu k_{22}^{-1} \tilde{\mathbf{A}} \mathbf{V}_2 + (\mu/\epsilon^l)(\tilde{\mathbf{K}}_{11} + \tilde{\mathbf{K}}_{22}) \mathbf{V}_2 - \tilde{\mathbf{Q}}_2^T \mathbf{P} = \tilde{\mathbf{F}}_2, \quad (5.36)$$

where the superscript T denotes the transpose. Applying the same process to the continuity equation (5.19):

$$\frac{\partial v_1}{\partial x_1} + \frac{\partial v_2}{\partial x_2} = -\frac{\epsilon^l}{1-\epsilon} + \epsilon^l \frac{\partial v_1^s}{\partial x_1} + \epsilon^l \frac{\partial v_2^s}{\partial x_2}, \quad (5.37)$$

we have the weak form

$$- \int_{\Omega_2^e} \Phi \frac{\partial \Psi^T}{\partial x_1} d\Omega_2^e \mathbf{V}_1 - \int_{\Omega_2^e} \Phi \frac{\partial \Psi^T}{\partial x_2} d\Omega_2^e \mathbf{V}_2 = - \int_{\Omega_2^e} \left(-\frac{\epsilon^l}{1-\epsilon} + \epsilon^l \frac{\partial v_1^s}{\partial x_1} + \epsilon^l \frac{\partial v_2^s}{\partial x_2} \right) \Phi d\Omega_2^e. \quad (5.38)$$

Let

$$\tilde{\mathbf{F}}_3 = - \int_{\Omega_2^e} \left(-\frac{\epsilon^l}{1-\epsilon} + \epsilon^l \frac{\partial v_1^s}{\partial x_1} + \epsilon^l \frac{\partial v_2^s}{\partial x_2} \right) \Phi d\Omega_2^e. \quad (5.39)$$

Then (5.38) becomes

$$-\tilde{\mathbf{Q}}_1 \mathbf{V}_1 - \tilde{\mathbf{Q}}_2 \mathbf{V}_2 = \tilde{\mathbf{F}}_3. \quad (5.40)$$

Writing the system of equations (5.35), (5.36) and (5.40) in element matrix form, we have

$$\begin{pmatrix} \mu k_{11}^{-1} \tilde{\mathbf{A}} + (\mu/\epsilon^l)(\tilde{\mathbf{K}}_{11} + \tilde{\mathbf{K}}_{22}) & \mu k_{12}^{-1} \tilde{\mathbf{A}} & -\tilde{\mathbf{Q}}_1^T \\ \mu k_{21}^{-1} \tilde{\mathbf{A}} & \mu k_{22}^{-1} \tilde{\mathbf{A}} + (\mu/\epsilon^l)(\tilde{\mathbf{K}}_{11} + \tilde{\mathbf{K}}_{22}) & -\tilde{\mathbf{Q}}_2^T \\ -\tilde{\mathbf{Q}}_1 & -\tilde{\mathbf{Q}}_2 & 0 \end{pmatrix} \begin{pmatrix} \mathbf{V}_1 \\ \mathbf{V}_2 \\ \mathbf{P} \end{pmatrix} = \begin{pmatrix} \tilde{\mathbf{F}}_1 \\ \tilde{\mathbf{F}}_2 \\ \tilde{\mathbf{F}}_3 \end{pmatrix}. \quad (5.41)$$

We now have the matrix form of the discrete system of equations in domain Ω_2 .

We next find the element matrix form for domain Ω_1 . Note that the momentum equations in Ω_1 are the same as those in Ω_2 except there are no velocity terms and the porosity is one.

Applying the same process as that applied to obtain (5.41), we have

$$\begin{aligned} & \frac{\mu}{\epsilon^l} \left[\left(\int_{\Omega_1^e} \frac{\partial \Psi}{\partial x_1} \frac{\partial \Psi^T}{\partial x_1} d\Omega_1^e + \int_{\Omega_1^e} \frac{\partial \Psi}{\partial x_2} \frac{\partial \Psi^T}{\partial x_2} d\Omega_1^e \right) \mathbf{V}_1 \right] - \int_{\Omega_1^e} \frac{\partial \Psi}{\partial x_1} \Phi^T d\Omega_1^e \mathbf{P} \\ &= - \int_{\Gamma_1^e} \Psi \Phi^T n_1 d\Gamma_1^e \mathbf{P} + \frac{\mu}{\epsilon^l} \left[\left(\int_{\Gamma_1^e} \Psi \frac{\partial \Psi^T}{\partial x_1} n_1 d\Gamma_1^e + \int_{\Gamma_1^e} \Psi \frac{\partial \Psi^T}{\partial x_2} n_2 d\Gamma_1^e \right) \mathbf{V}_1 \right], \end{aligned} \quad (5.42)$$

$$\begin{aligned} & \frac{\mu}{\epsilon^l} \left[\left(\int_{\Omega_1^e} \frac{\partial \Psi}{\partial x_1} \frac{\partial \Psi^T}{\partial x_1} d\Omega_1^e + \int_{\Omega_1^e} \frac{\partial \Psi}{\partial x_2} \frac{\partial \Psi^T}{\partial x_2} d\Omega_1^e \right) \mathbf{V}_2 \right] - \int_{\Omega_1^e} \frac{\partial \Psi}{\partial x_2} \Phi^T d\Omega_1^e \mathbf{P} \\ &= - \int_{\Gamma_1^e} \Psi \Phi^T n_2 d\Gamma_1^e \mathbf{P} + \frac{\mu}{\epsilon^l} \left[\left(\int_{\Gamma_1^e} \Psi \frac{\partial \Psi^T}{\partial x_1} n_1 d\Gamma_1^e + \int_{\Gamma_1^e} \Psi \frac{\partial \Psi^T}{\partial x_2} n_2 d\Gamma_1^e \right) \mathbf{V}_2 \right], \end{aligned} \quad (5.43)$$

Let Ω_1^e be the element domain such that $\Omega_1 = \bigcup_e \Omega_1^e$. Writing (5.42), (5.43) and (5.38) in the matrix form, we have

$$\begin{pmatrix} (\mu/\epsilon^l)(\tilde{\mathbf{K}}_{11} + \tilde{\mathbf{K}}_{22}) & 0 & -\tilde{\mathbf{Q}}_1^T \\ 0 & (\mu/\epsilon^l)(\tilde{\mathbf{K}}_{11} + \tilde{\mathbf{K}}_{22}) & -\tilde{\mathbf{Q}}_2^T \\ -\tilde{\mathbf{Q}}_1 & -\tilde{\mathbf{Q}}_2 & 0 \end{pmatrix} \begin{pmatrix} \mathbf{V}_1 \\ \mathbf{V}_2 \\ \mathbf{P} \end{pmatrix} = \begin{pmatrix} \tilde{\mathbf{B}}_1 \\ \tilde{\mathbf{B}}_2 \\ \tilde{\mathbf{F}}_3 \end{pmatrix} \quad (5.44)$$

where

$$\tilde{\mathbf{B}}_1 = - \int_{\Gamma_1^e} \Psi \Phi^T n_1 d\Gamma_1^e \mathbf{P} + \frac{\mu}{\epsilon^l} \left[\left(\int_{\Gamma_1^e} \Psi \frac{\partial \Psi^T}{\partial x_1} n_1 d\Gamma_1^e + \int_{\Gamma_1^e} \Psi \frac{\partial \Psi^T}{\partial x_2} n_2 d\Gamma_1^e \right) \mathbf{V}_1 \right], \quad (5.45)$$

and

$$\tilde{\mathbf{B}}_2 = - \int_{\Gamma_1^e} \Psi \Phi^T n_2 d\Gamma_1^e \mathbf{P} + \frac{\mu}{\epsilon^l} \left[\left(\int_{\Gamma_1^e} \Psi \frac{\partial \Psi^T}{\partial x_1} n_1 d\Gamma_1^e + \int_{\Gamma_1^e} \Psi \frac{\partial \Psi^T}{\partial x_2} n_2 d\Gamma_1^e \right) \mathbf{V}_2 \right]. \quad (5.46)$$

Note that the velocities and pressure in Ω_1 and Ω_2 are not the same but we still use the same notation for simplicity. Since the normal and shear stresses are continuous across the interface $\overline{\Omega_1} \cap \overline{\Omega_2}$ where we can share the nodes between the pure-fluid and porous medium domains, the velocity and pressure terms in the surface integrals $\tilde{\mathbf{B}}_1$ and $\tilde{\mathbf{F}}_1$ are equal in magnitude but have opposite signs which cancel each other in the final discretized equation, [43, 89, 99]. Similarly, the velocity and pressure terms in the surface integrals $\tilde{\mathbf{B}}_2$ and $\tilde{\mathbf{F}}_2$ can be canceled in the final discretized equation. Therefore, by using finite element method, the stress-continuity condition is automatically satisfied and no special procedure is needed to impose such interfacial condition.

5.3 Validation of the Code and Numerical Results

Before we provide the Stokes-Brinkman numerical results for our problem, we validate our results by comparing with an exact solution for which the boundary conditions are simple enough to determine the analytic solution. The boundary condition imposed is that at $x_2 = H_{c1} + H_{c2} = H_c$, see Figure 5.1, the liquid is dragged with a constant velocity u_0 by an impermeable plate. Using the Brinkman equation to model fluid flow in Ω_2 , the general form for the velocity is [58]

$$u(x_2) = \begin{cases} C_c + C_k(x_2 - H_{c2}) & \text{if } x_2 > H_{c2} \\ C e^{(x_2 - H_{c2})/\sqrt{k}} & \text{if } x_2 < H_{c2}. \end{cases} \quad (5.47)$$

where C_c, C_k and C are constants and k is the scalar permeability. Applying the boundary condition

$$u(H_c) = u_0 \quad (5.48)$$

and the continuities of the horizontal component of the velocity and shear stress across the free-fluid/porous-medium interface, i.e.

$$u|_{H_{c2}^-} = u|_{H_{c2}^+} \quad (5.49)$$

$$\mu' \frac{\partial u}{\partial x_2} \Big|_{x_2=H_{c2}^-} = \mu \frac{\partial u}{\partial x_2} \Big|_{x_2=H_{c2}^+}, \quad (5.50)$$

where $+$ and $-$ refer to the free fluid and porous medium respectively and μ' is the effective viscosity which is a parameter matching the shear stress at the free-fluid/porous-medium interface [68], we obtain expressions for the coefficients C_c, C_k and C :

$$C_c = \frac{u_0}{1 + (\mu'/\mu)((H_c - H_{c2})/\sqrt{k})}, \quad (5.51)$$

$$C_k = \frac{\mu'}{\mu} \frac{C_c}{\sqrt{k}}, \quad (5.52)$$

$$C = C_c. \quad (5.53)$$

Eliminating C_c, C_k and C from (5.47) using (5.51)-(5.53), we have

$$u(x_2) = \frac{u_0}{1 + \frac{\mu'}{\mu} \left(\frac{H_c - H_{c2}}{\sqrt{k}} \right)} \begin{cases} 1 + \frac{\mu'}{\mu} \left(\frac{x_2 - H_{c2}}{\sqrt{k}} \right) & \text{if } x_2 > H_{c2} \\ e^{\frac{(x_2 - H_{c2})}{\sqrt{k}}} & \text{if } x_2 < H_{c2}. \end{cases} \quad (5.54)$$

Figure 5.3 shows the velocity profiles of the exact solution and our numerical result when the velocity $u_0 = 1$, the porosity $\epsilon^l = 0.64457$, the effective viscosity $\mu' = \mu/\epsilon^l$, the scalar permeability $k = 9.5660e - 04$ and the height $H_c = 1$ and $H_{c2} = 0.7071$. The number of elements and degrees of freedom are 12,800 and 58,403, respectively, and the L_2 -norm error is 0.4385.

We next employ our numerical permeabilities that are a function of the angles θ from about 26 to 90 degrees to compare the velocity profiles to the exact solutions where the variable H_{c2} is calculated from $H_c \sin \theta$ and k is the component k_{33} of the permeability tensor \mathbf{k} , see Figure 3.3. The results are given in Figure 5.4 for 800 elements and 3803 degrees of freedom for both pressure and velocities while the L_2 -norm errors are shown in Table 5.1 for 11 different angles. For $\theta = 45^\circ$, Figure 5.5 shows the convergence of the velocity profiles of our numerical results to the exact solution when the number of elements is increasing from 200 to 12800. The L_2 -norm errors of the graphs are demonstrated in Table 5.2.

Next, we calculate the fluid velocity profile when the cylinders move as a pendulum. We employ an angular velocity $w_a = d\theta/dt$ and assume that the maximum velocity is at the

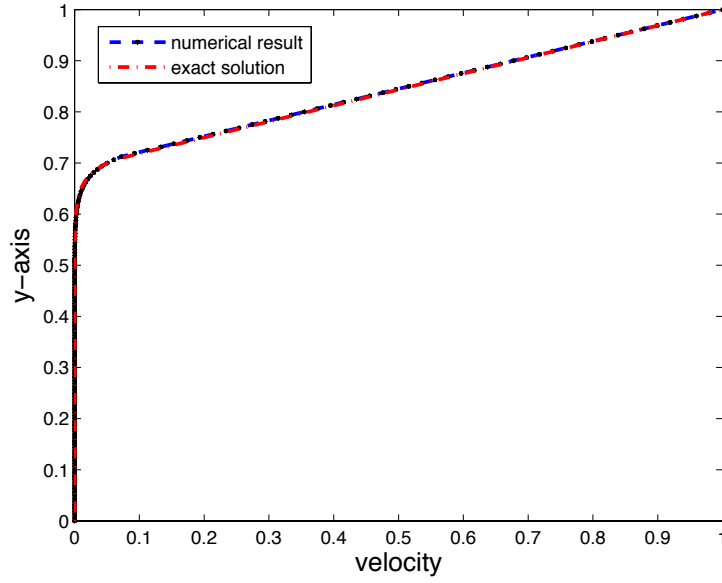


Figure 5.3: Velocity profiles in the x_2 direction or y -axis of the exact solution and our numerical result where $u_0 = 1$; $\mu = 1$; $\epsilon^l = 0.64457$; $H_c = 1$ and $H_{c2} = 0.7071$.

Table 5.1: L_2 -norm error of the velocity for the Stokes-Brinkman equations where θ is the angle between the array of cylinders and the horizontal plane.

angle θ°	L_2 -norm errors
26.5	0.0466
30.9	1.0092
34.9	0.7471
38.6	0.7548
41.9	1.0390
45.0	1.5918
51.3	0.8077
56.3	0.9084
63.4	0.6294
75.9	0.9683
90.0	1.2073

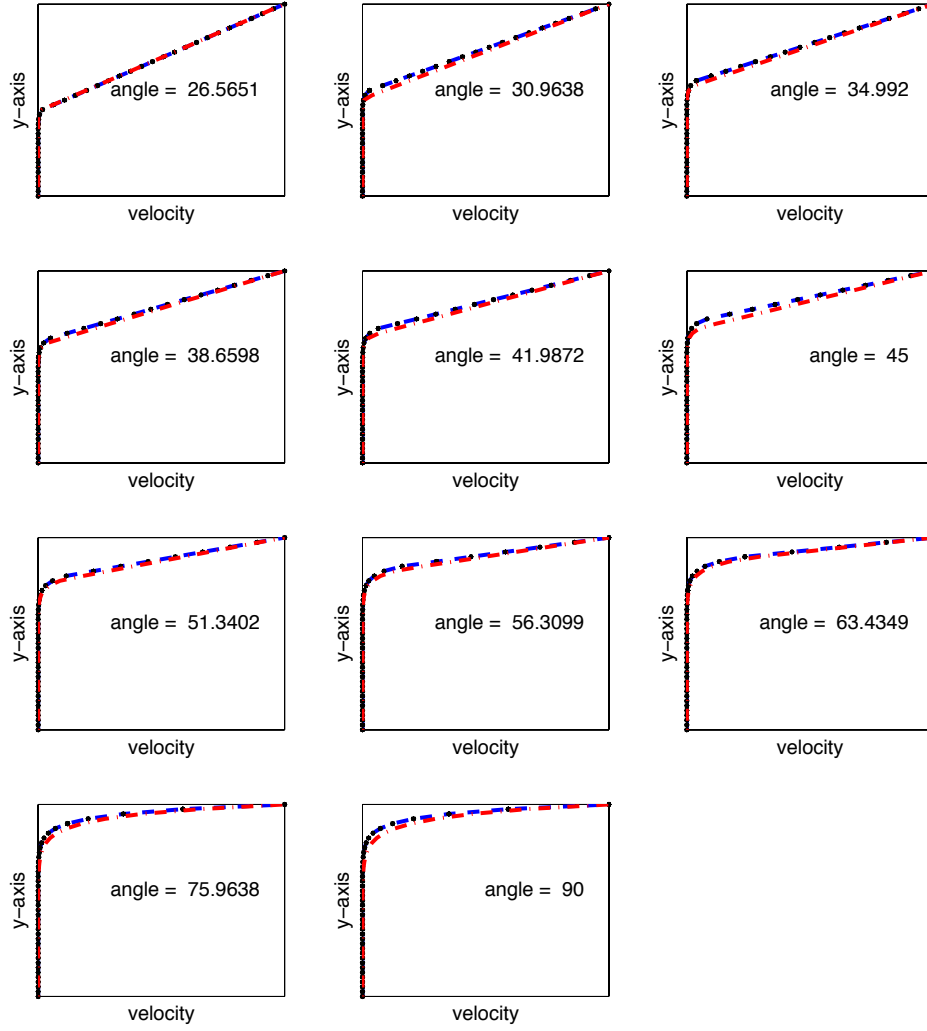


Figure 5.4: Velocity profiles of the numerical and exact solutions using our permeability results with the corresponding angle θ ; $u_0 = 1$; $\mu = 1$; $H_c = 1$.

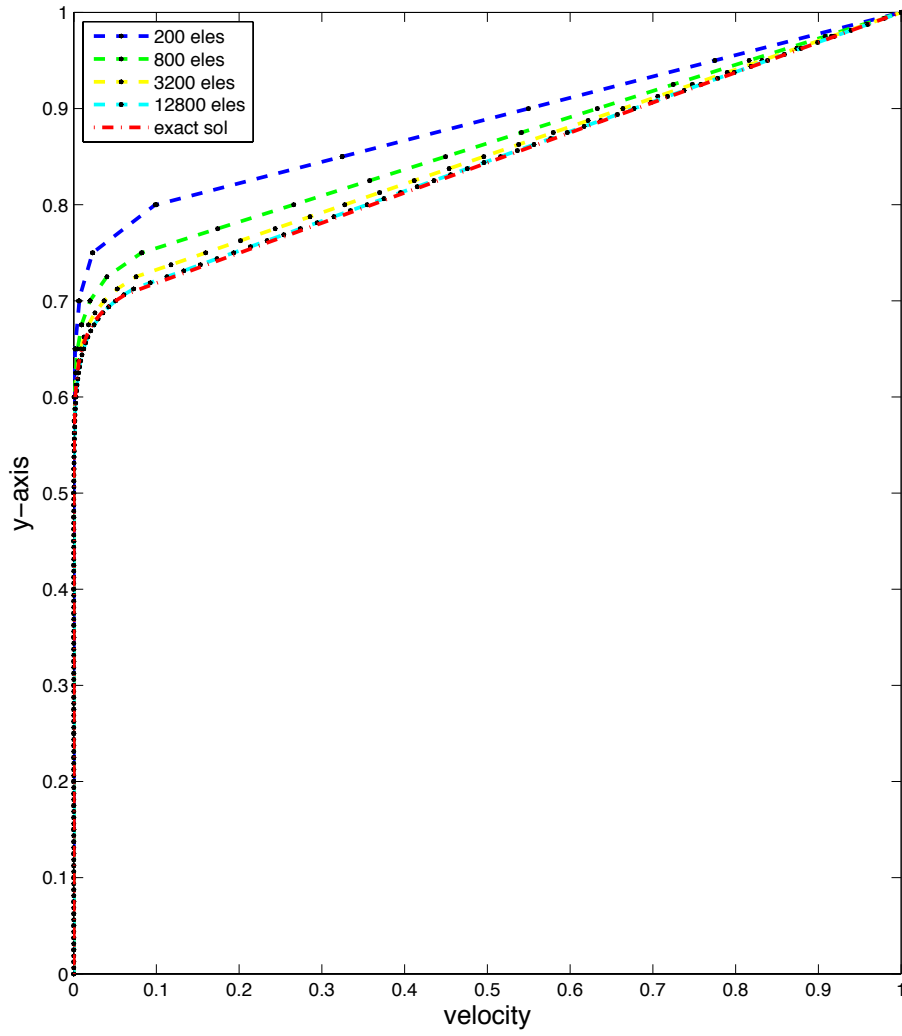


Figure 5.5: Convergence of the velocity profiles of the numerical results to the exact solutions when the angle θ is 45°

Table 5.2: L_2 -norm errors of the numerical and exact solutions of Stokes-Brinkman equations when the numbers of elements are increasing where # dof is the number of degrees of freedom and Δx is the uniform length of each element.

# ele	# dof	Δx	L_2 -norm errors
200	1003	0.1	1.8434
800	3803	0.05	1.5918
3200	14803	0.025	1.1824
12800	58403	0.0125	0.4385

angle $\theta = 90^\circ$. Our initial numerical result, Figure 5.6, is calculated when the shear stress at the free-fluid/porous-medium interface is assumed to be zero. This means no shear force on the free fluid and only the tip of cilia moves the fluid. The lines from the left to right are the increasing angle θ between the array of cylinders and the horizontal plane. As can be seen from Figure 5.6 the velocity in the porous medium (Ω_2) increases as θ increases. The velocity of the Stokes fluid at $\overline{\Omega_1} \cap \overline{\Omega_2}$ is the same as the velocity in the porous medium due to the continuity of normal and shear stresses at the interface.

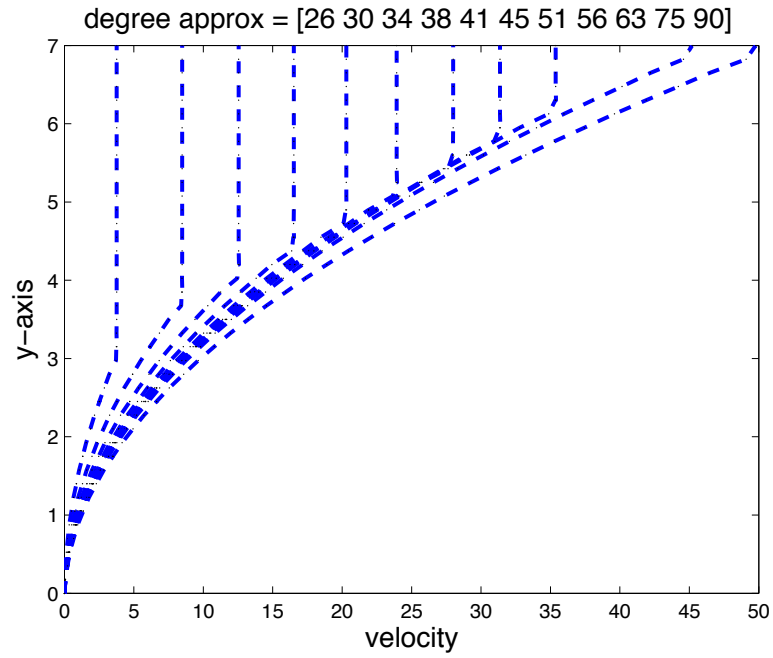


Figure 5.6: Velocity profile in the x_2 direction of the cilia making angles $\theta = 26, 30, \dots, 90^\circ$ with the horizontal plane when the shear stress is zero at the free-fluid/porous-medium interface.

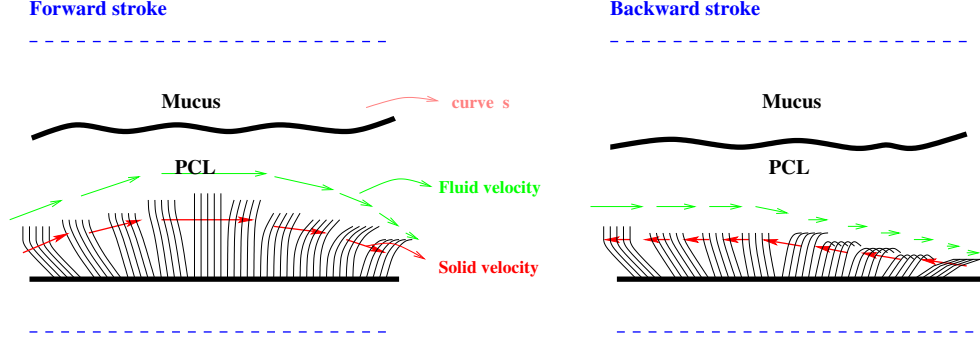


Figure 6.1: The cartoon picture is showing the free boundary having a unknown curve s while the cilia is moving forward and backward making the angle θ with the horizontal plane in the PCL.

6. FREE BOUNDARY TWO-DIMENSIONAL MODEL

The purpose of this Chapter is to propose a model for the free boundary problem in the two-dimensional domain $\Omega = \Omega_1 \cup \Omega_2$. Figure 6.1 illustrates the domain of interest and the free boundary between the PCL and mucous layers, whose height is a priori unknown. The curve s , which is a function of \mathbf{x} and t , is an unknown and changes due to the movement of the cilia.

There exit many approaches for simulating free boundary problems including the immersed boundary method [72, 81], the volume of fluid (VOF) method [50, 76] and the level set method [79]. For example, Hirt and Nichols [50] uses the volume of fluid method to treat complicated free boundary configurations, which is proposed originally by Nichols et al.[76]. The idea of the immersed boundary method is provided in [72] and [81] where it is used to model systems of elastic structures (or membranes) deforming and interacting with fluid flows. In this approach, the fluid is represented in an Eulerian coordinate frame and the structures in a Lagrangian coordinate frame. A disadvantage of this method is that imposing of the boundary conditions is not straightforward compared to the others. For the level set method, the curves at the interface are tracked on a fixed Cartesian grid (Eulerian approach). The method is a great tool for modeling time-varying objects such as a drop of oil floating in water [79]. One of advantages of level set method is two to three dimensions can be coded quickly which is time consuming for the VOF method. However, one of the

considerable advantages of the VOF method is that they conserve mass well while the level set method does not. For steady-state problems, authors in [82, 110] employed new finite element methods to solve free boundary problems. Moreover, Saavedra and Scott [86] presented theoretical error analysis of a finite element method of a free boundary problem for viscous liquid. For the steady-state Laplace equation, Zhang and Babuška [110] solved the free boundary problem in a fixed domain exactly, as well as an exponential rate of convergence. They proved that the sequence of solutions of free boundary problems converges to the solution of the given free boundary problem. In addition, Peterson et al. [82] provides a new iterative method for two-dimensional free-surface problems with arbitrary initial geometries. They used an elastic deformation of the mesh to preserve the continuity. Next, we provide our model and outline the method from [82] to get an idea to be able to apply to our free boundary problem.

6.1 Model Problem and Boundary Conditions

We summarize the model and boundary conditions in this section. We assume that the the free surface at the free-fluid/porous-medium interface is represented by a curve $\mathbf{s}(s, t) = (x(s, t), y(s, t))$ parametrized by arc length s and depended on time t . At the free boundary, curve \mathbf{s} , the kinematic boundary condition at which a material point on the boundary remains on the boundary can be expressed as [82]

$$\mathbf{n} \cdot \mathbf{v} = \mathbf{n} \cdot \frac{\partial \mathbf{s}}{\partial t}, \quad (6.1)$$

where \mathbf{n} is the outward free-surface normal vector and $\mathbf{v} = \epsilon^l \mathbf{v}^l$. The absence of a material derivative in the steady-state momentum equation (5.1) allows the problem to be solved using quasi-steady-state methods. The free-surface location can be updated explicitly using the kinematic boundary condition. Before we mention the numerical method, the primary system of equations of our computational domains Ω_1 and Ω_2 is

$$\mu \mathbf{k}^{-1} \cdot (\epsilon^l \mathbf{v}^l - \epsilon^l \mathbf{v}^s) + \nabla p - \frac{\mu}{\epsilon^l} \nabla \cdot (2\epsilon^l \mathbf{d}^l) = \rho \mathbf{g}, \quad \text{in } \Omega_1 \cup \Omega_2, t > 0 \quad (6.2)$$

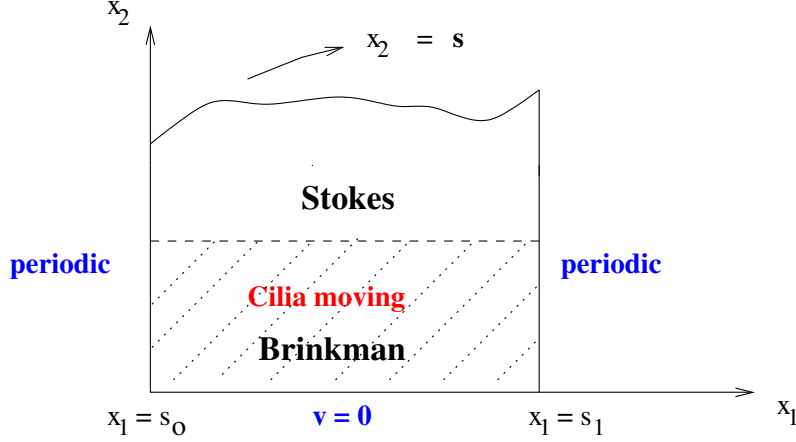


Figure 6.2: A two dimensional Cartesian coordinate system with axis lines x_1 and x_2 and the cartoon picture of the moving cilia creating a free boundary curve s with boundary conditions.

$$\epsilon^l + (1 - \epsilon^l) \nabla \cdot (\epsilon^l (\mathbf{v}^l - \mathbf{v}^s)) = 0, \quad \text{in } \Omega_1 \cup \Omega_2, t > 0 \quad (6.3)$$

$$\mathbf{n} \cdot \mathbf{v} = \mathbf{n} \cdot \frac{\partial \mathbf{s}}{\partial t} \quad \text{at } x_2 = s \quad (6.4)$$

$$\mathbf{v} = 0 \quad \text{at } x_2 = 0, \quad (6.5)$$

$$\mathbf{v} \text{ and } p \text{ are periodic} \quad \text{at } x_1 = s_0 \text{ and } x_1 = s_1. \quad (6.6)$$

6.2 Numerical Implementation

In this section, we summarize the method from [82] to be able to adapt to our free boundary problem. In the absence of extreme curvature, the semi-explicit method is an attractive approach. To solve the free boundary problem via the finite element method, we consider two main steps. First, the flow of the liquid is determined using a fixed mesh. Second, at each iteration, the mesh is modified efficiently with some form of continuous mesh deformation [71, 82]. Both the particular form of continuous deformation and the mesh topology must be determined in advance. In order to update the mesh, the kinematic boundary condition is employed. Frequently, conservation of mass is also taken into consideration. However, in this work, only the kinematic condition will be applied at each iteration. If the change of mass is not conserved within an allowable error, the formula of the conservation of mass will be considered.

The free-surface boundary location is updated using a first-order explicit scheme. The kinematic boundary condition is solved for $\dot{\mathbf{s}}$ using [41] with the time step being selected using the CFL condition

$$\delta t \leq \min\left(\frac{1}{4} \frac{l_{\min}}{\mathbf{v}_{\max}}, \delta_{\max}\right) \quad (6.7)$$

where \mathbf{v}_{\max} is the largest velocity found from the most recent solution; l_{\min} denotes the length of the shortest edge in the mesh and δ_{\max} is a prescribed maximum time step and the constant $1/4$ arises due to the use of the quadratic elements. It is sometimes necessary to employ smaller values of the constant in order to ensure stability.

Once the free surface is located, the interior nodes are repositioned via the continuous deformation model which maintains the original connectivity. If the mesh quality falls below prescribed thresholds, the mesh is regenerated using a standard Delaunay triangulation algorithm and only the locations of the boundary nodes is preserved.

The semi-explicit scheme can be employed when the equations are linear so that the matrices are symmetric and the location of the free-surface nodes need not be considered as variables during the flow solution phase, then reducing the computational cost.

If surface tension is involved, the free-surface boundary conditions depend on the pattern of the free-surface. Because the accuracy of the free-surface boundary conditions depends directly on the accuracy of the free-surface representation, the accuracy of the solution is sensitive to the resolution of the mesh at the boundary. For a two-dimensional domain, if the number of boundary unknowns increases linearly, then the number of interior unknowns must increase quadratically. Because quadratic elements allow us to obtain more accuracy than linear elements, a finer discretization on the boundary than in the interior of the domain may be possible. When the free surface has non-zero surface tension, the gradient of the stress at the free surface is

$$\hat{\mathbf{t}} = -\gamma\kappa\mathbf{n} \quad (6.8)$$

where γ is the surface tension; κ is the curvature and \mathbf{n} is the outward unit normal vector. Next, we clarify how to implement (6.8) into the stiffness matrix. After applying the variational formula to the momentum equation, we have that the divergence of the stress tensor moves to the test function,

$$\int_{\Omega} \nabla w_i \cdot \mathbf{t} d\Omega = - \int_{\partial\Omega} w_i \hat{\mathbf{t}} ds = \int_{\partial\Omega} w_i \gamma \kappa \mathbf{n} ds \quad (6.9)$$

where w_i is the test function and (6.8) is applied at the last equality. The equation (6.9) is the stress boundary conditions which can be brought to the right-hand side of the momentum equation. To explicitly calculate (6.9), we may employ

$$\kappa \mathbf{n} = \frac{d\tau}{ds}, \quad (6.10)$$

where τ is the tangent at the curve \mathbf{s} . Then at a free surface edge $\partial\Omega^e$, we have

$$\int_{\partial\Omega^e} w_i \gamma \kappa \mathbf{n} ds = \int_{\partial\Omega^e} w_i \gamma \frac{d\tau}{ds} ds = w_i \gamma \tau|_{\partial\Omega^e} - \int_{\partial\Omega^e} \gamma \tau \frac{dw_i}{ds} ds, \quad (6.11)$$

where the tangent τ is given by

$$\tau = \sum_{i=1}^3 s_i \frac{dw_i}{ds}, \quad (6.12)$$

where i ranges over the three basis functions active on any particular edge and the variables $s_i, i = 1, 2, 3$, are the positions of the relevant boundary nodes. The above procedure is summarized as follows:

1. Choose an initial free boundary location and set up the nodes.
2. Solve for the velocity and pressure fields.
3. If evolution is completed, then stop.
4. Update the free boundary using the velocity field.
5. If boundary nodes need to be adjusted,
 - Merge boundary edges.

- Split boundary edges.
 - Adjust boundary edges.
 - Remesh the domain.
 - Interpolate the previous solutions onto new mesh if necessary.
 - Go to 2.
6. Solve the elastic problem and relocate interior nodes.
7. Go to 2.

The procedures of merging, splitting and adjusting can be found in [82].

In this chapter, we summarize a possible approach to solve the free boundary problem. An attractive of this strategy is because our free boundary problem involves with the absence of extreme curvature. Moreover, one of advantages of this approach is time-saving because the new adjustment problem depends only on the selection of an initial boundary mesh.

7. CONCLUSION

In this thesis we modeled the periciliary layer, PCL, of lungs. The PCL contains cilia, hair-like organelles that reside on the surface of the epithelium and whose purpose is to sweep debris away from lungs, and the low viscous liquid in which the cilia reside, PCL fluid. The PCL fluid is modeled as an incompressible fluid undergoing Stokes flow, and the cilia is modeled as a periodic array of cylinders that rotate about their base with height varying as a function of the angle. We developed a mathematical model of the movement of the PCL fluid due to the movement of the cilia.

The portion of the PCL which contains the cilia was treated as a porous medium. The permeability of the porous medium was determined by using homogenization to determine a system of equation which were then numerically solved using a finite element method. This approach allowed us to find an expression for the permeability in terms of the geometry of the array of cylinder that is numerically inexpensive. The results were validated by comparison with results available in the literature with good agreement. In addition, the calculated permeability was shown to be a symmetric and positive definite matrix [90], as it theoretically should be, and for different sizes of periodic cells, the calculated permeability matrices were numerically corresponding as was expected.

As is consistent with the physical meaning of permeability (a measure of the ease with which fluid can move through the porous medium), the permeability calculations indicated the diagonal components of the permeability decrease as the angle between the cylinders and the base decrease, see Figure 3.3, and for fixed angles, they decrease for increasing radii, see Figure 3.2. Further, we can see from the results that the permeability tends to zero if the porosity tends to zero. These results can be extended to general cases by varying the angles and radii as in Figures 3.8, 3.9, 3.10. Moreover, we provided explicit functions of the components of the permeability tensor as a function of the ratio r/d and the angle θ , see Tables 3.4 and 3.5.

Because the Kozeny-Carman equation is among the more popular equations used to determine the scalar permeability as a function of porosity, we compared the Kozeny-Carman permeability results with one third the trace of our numerical permeability tensor. Because periodic array of angled cylinders produce anisotropic permeability tensors, it would not have been expected that using the Kozeny-Carman equation would give comparable results. However we found the opposite to be true - they were in excellent agreement. However, because of the anisotropic nature of the problem, the Kozeny-Carman equations cannot be used for our problem.

To model the PCL, we used the permeability tensor in a system of equations that model the PCL at the macroscale. This model is composed of the Brinkman equation, which can be derived using Hybrid Mixture Theory (HMT), in the part of the PCL containing the cilia, Ω_2 , and the Stokes equation in the part of the PCL above the cilia, Ω_1 . The Stokes-Brinkman equations with stress-continuity conditions at the porous-medium and free-fluid interface were used as the mathematical model to determine the velocity and pressure fields of the fluid in the PCL. This allowed us to match the stress field between the two domains.

We also showed the existence and uniqueness of the Stokes-Brinkman equations when the permeability coefficient is a second-order tensor. Numerically, the two-dimensional mixed finite element method was applied to the regions Ω_1 and Ω_2 . The code was validated by comparing the result with an exact solution where the top of the free fluid is dragged with a constant velocity. Numerical results are provided for the case of stress continuity at the free-fluid/porous medium interface and the velocity of a pendulum is applied for the velocity of the cilia. Finally, we also proposed a method for the solving the problem as a free boundary problem using the semi-explicit method of [82].

Our problem is motivated by a biological interest and the mathematical model is driven by biological insight. The model developed could be used to develop medication for lung diseases. Some lung diseases cause conditions in which some functions of the lungs are adversely affected because the body produces abnormally thick and sticky mucus which can

block the airways and where cilia have a hard time removing the thick mucus. Examples of such diseases include Cystic Fibrosis (CF), Chronic Bronchitis (CB) and Primary Ciliary Dyskinesia (PCD). For the genetic-lung-disorder PCD disease, the cilia are abnormal or do not move. Better understanding of how the fluid phase in the PCL are propelled by cilia and how the fluid properties affect the movement can lend to more effective treatments. For example, physicians are using salt added to the PCL fluid to make it easier to expel thick mucus out of lungs. The treatment indicates the property of PCL fluid is important and its interaction with cilia needs to be better understood. Having an appropriate model can lead to more effective medication.

Future work includes extending the PCL model to model three-dimensions and incorporating between the PCL and mucus.

APPENDIX A. NOMENCLATURE

variables	definitions	units	equations
a	diameter of cylinders, $2r$	$[a] = L$	Figure 1.3
a_a	arithmetic average fiber diameter of cylinder	$[a_a] = L$	(3.7)
a_s	surface average fiber diameter of cylinder	$[a_s] = L$	(3.7)
a_i	$i = 1, \dots, 15$, coefficients of polynomials	$[a_i] = 1$	Table 3.4
$a(\cdot, \cdot)$	bilinear functional		(4.101)
A	a elliptic shape		Figure 3.12
$\langle A, \cdot \rangle$	a linear operator		Definition (4.8)
\mathbf{A}	a block matrix in the stiffness matrix		(3.39)
$\tilde{\mathbf{A}}$	a block matrix in the stiffness matrix		(5.32)
$\langle B, \cdot \rangle$	a linear operator		Definition (4.8)
$\langle B', \cdot \rangle$	the dual operator of B		Definition (4.8)
$b(\cdot, \cdot)$	bilinear functional		(4.102)
$c_1(\cdot)$	linear functional		(4.103)
$c_2(\cdot)$	linear functional		(4.104)
C	a constant parameter	$[C] = \frac{L}{T}$	(3.5)
C_v	unit conversion factor		(3.7)
C_d	drag coefficient	$[C_d] = 1$	(3.3)
C_c	a positive constant	$[C_c] = 1$	(4.131)
C_k	a constant	$[C_k] = 1$	(3.45)
d	distance between cilia in a straight direction	$[d] = L$	Figure 1.3
d_1	distance between cilia in diagonal direction	$[d_1] = L$	Figure 1.3

variables	definitions	units	equations
\mathbf{d}^l	rate of deformation	$[\mathbf{d}^l] = \frac{1}{T}$	(4.2)
\mathbf{D}	a block matrix in the stiffness matrix		(3.39)
\mathbf{D}_j	a block matrix in the stiffness matrix		(3.35)
D_w^α	a weak derivative		Definition (4.2)
D^α/Dt	material time derivative of α phase		(4.27)
\mathbf{e}^i	the unit vector in the direction of y_i axis	$[\mathbf{e}^i] = 1$	(2.31)
\hat{e}_β^α	interactive quantity at the interface $\alpha\beta$	$[\hat{e}_\beta^\alpha] = \frac{1}{T}$	(4.19)
\mathbf{E}_{jj}	a block matrix in the stiffness matrix		(3.36)
\mathbf{E}	$= \mathbf{E}_{11} + \mathbf{E}_{22} + \mathbf{E}_{33}$		(3.37)
f	a source term		(4.100b)
\mathbf{f}	a source term		(4.100a)
\mathbf{f}^s	$= (f_1^s, f_2^s, f_3^s)$, source term in Stoke equation	$[\mathbf{f}^s] = \frac{M}{L^2 T^2}$	(2.2)
\mathbf{F}^d	drag force on each object	$[\mathbf{F}^d] = \frac{M}{L T^2}$	(3.1)
F^d	total drag force	$[F^d] = \frac{M}{T^2}$	(3.5)
\mathbf{F}_{ij}	a block matrix in the stiffness matrix		(3.36)
\mathbf{F}	a block matrix in the stiffness matrix		(3.39)
$\tilde{\mathbf{F}}_1$	a source term in element matrix		(5.33)
$\tilde{\mathbf{F}}_2$	a source term in element matrix		(5.34)
$\tilde{\mathbf{F}}_3$	a source term in element matrix		(5.39)
g	gravity	$[g] = \frac{L}{T^2}$	(2.38)
\mathbf{g}	$= (0, 0, -g)$ gravity vector	$[\mathbf{g}] = \frac{L}{T^2}$	(4.1)
\mathbf{g}^α	mass-averaged gravity of α phase	$[\mathbf{g}^\alpha] = \frac{L}{T^2}$	(4.28)
h	piezometric head	$[h] = L$	(2.38)
h_θ	height of ellipsoidal cylinder	$[h_\theta] = L$	Figure 3.12
$H(\Omega)$	a Hilbert space		(2.19)

variables	definitions	units	equations
H_c	$H_c = H_{c1} + H_{c2}$	$[H_c] = L$	Figure 1.2
H_{c1}	height of domain Ω_1	$[H_{c1}] = L$	Figure 1.2
H_{c2}	height of domain Ω_2	$[H_{c2}] = L$	Figure 1.2
H_h	finite-dimensional subspace of $L_0^2(\Omega)$		(5.27)
$H_0^1(\Omega)$	a Sobolev subspace of $H^1(\Omega)$		(4.90)
$H_s^1(\Omega)$	a Sobolev subspace of $H^1(\Omega)$		(4.91)
$H^{-1}(\Omega)$	dual space of $H_0^1(\Omega)$		(4.92)
$H^{1/2}(\partial\Omega)$	a Sobolev-Slobodeckij space		below (4.95)
k	a scalar permeability	$[k] = L^2$	(3.10)
\mathbf{k}	$= \widetilde{\mathbf{u}^i}$, permeability tensor	$[\mathbf{k}] = L^2$	(2.36)
$k1$	a scalar permeability	$[k1] = L^2$	(3.61)
\mathbf{k}^{-1}	inverse of permeability tensor	$[\mathbf{k}^{-1}] = \frac{1}{L^2}$	(4.2)
k^*	dimensionless scalar permeability	$[k^*] = 1$	below (3.11)
\mathbf{k}^*	dimensionless permeability	$[\mathbf{k}^*] = 1$	(2.43)
k_{RM}	nondimensional scalar permeability (Rocha & Cruz)	$[k_{RM}] = 1$	Table 3.2
k_s	nondimensional permeability of sphere	$[k_s] = 1$	Table 3.2
k_1	a constant depending on geometry	$[k_1] = 1$	(3.43)
K	a constant		Theorem (4.5)
K'	a constant		Theorem (4.5)
\mathbf{K}	hydraulic conductivity	$[\mathbf{K}] = \frac{L}{T}$	(2.38)
$\tilde{\mathbf{K}}_{ij}$	a block matrix in the stiffness matrix		(5.32)
l	thickness of a cell	$[l] = L$	(3.7)
l_{\min}	length of the shortest edge	$[l_{\min} = L]$	(6.7)
L	length of a ellipsoidal cylinder	$[L] = L$	Figure 3.12

variables	definitions	units	equations
L_c	length of domain Ω	$[L_c] = L$	Figure 1.2
$L_0^2(\Omega)$	a Sobolev subspace of $L^2(\Omega)$		(4.89)
$L_{loc}^1(\Omega)$	the set of locally integrable functions		below (4.106)
\mathbf{n}	outward unit normal vector	$[\mathbf{n}] = 1$	(3.1)
\mathbf{n}_α	outward unit normal vector to δV_α	$[\mathbf{n}_\alpha] = 1$	(4.11)
p	pressure	$[p] = \frac{M}{L \cdot T^2}$	(2.2)
p^i	asymptotic expansion of pressure p	$[p^i] = \frac{M}{L \cdot T^2}$	(2.3)
\mathbf{P}	vector of $p_l, l = 1, 2, \dots, L$		(5.29)
\mathbf{v}_i	vector of $v_i^m, m = 1, 2, \dots, M$		(5.28)
\mathbf{q}	Darcy's velocity	$[\mathbf{q}] = \frac{L}{T}$	(2.36)
q^i	solution of system of equations (2.30-2.32)	$[q^i] = L$	(2.30-2.32)
q^*	dimensionless variable q^i	$[q^*] = 1$	(2.40)-(2.42)
\mathbf{Q}	vector of $q_j, j = 1, 2, \dots, n$		(3.28)
$\tilde{\mathbf{Q}}_i$	a block matrix in the stiffness matrix		(5.32)
r	radius of a cylinder	$[r] = L$	Figure 1.3
r_1	a radius of an ellipse		Figure 3.12
r_p	radius of a sphere	$[r_p] = L$	(3.3)
Re	$= aU\rho/\mu$, Reynolds number	$[Re] = 1$	below (3.5)
\mathbf{s}	a function on boundary $\partial\Omega$		below (4.95)
S	area of particular surface per unit volume	$[S] = \frac{1}{L}$	(3.43)
S_A	surface area of solid staying in fluid	$[S_A] = L^2$	(3.46)
\mathbf{t}	stress tensor	$[\mathbf{t}] = \frac{M}{L \cdot T^2}$	(3.1)
\mathbf{t}^α	stress tensor of α phase	$[\mathbf{t}] = \frac{M}{L \cdot T^2}$	(4.29)
$\hat{\mathbf{t}}$	gradient of the stress	$[\hat{\mathbf{t}}] = \frac{M}{L^2 \cdot T^2}$	(6.8)
$\hat{\mathbf{T}}_\beta^\alpha$	acceleration term at the interface $\alpha\beta$	$[\hat{\mathbf{T}}_\beta^\alpha] = \frac{L}{T^2}$	(4.30)

variables	definitions	units	equations
u	exact solution of Stokes-Brinkman	$[u] = \frac{L}{T}$	(5.47)
u_0	constant velocity at the top of the PCL	$[u_0] = \frac{L}{T}$	(5.48)
\mathbf{u}^i	solution of system of equations (2.30)-(2.32)	$[\mathbf{u}^i] = L^2$	(2.30)-(2.32)
\mathbf{u}^*	dimensionless variable \mathbf{u}^i	$[\mathbf{u}^*] = 1$	(2.40)-(2.42)
u^p	velocity of the porous flow	$[u^p] = \frac{L}{T}$	(5.6)
u^v	velocity of the viscous flow	$[u^v] = \frac{L}{T}$	(5.6)
u_{slip}^v	slip velocity	$[u_{slip}^v] = \frac{L}{T}$	(5.6)
$\widetilde{\mathbf{u}}^i$	$= \mathbf{k}$, permeability tensor	$[\widetilde{\mathbf{u}}^i] = L^2$	(2.33)
\mathbf{u}_j	vector of $u_j^m, m = 1, 2, \dots, M$		(3.27)
U	upstream velocity of fluid	$[U] = \frac{L}{T}$	below (3.5)
\mathbf{U}	a block matrix in the stiffness matrix		(3.39)
\mathbf{v}	$= (v_1, v_2, v_3)$, fluid velocity of Stokes equation	$[\mathbf{v}] = \frac{L}{T}$	(2.1)
	also used in the momentum equation	$[\mathbf{v}] = \frac{L}{T}$	(4.21)
	also used $\mathbf{v} = \epsilon^l \mathbf{v}^l$ in Brinkman equation	$[\mathbf{v}] = \frac{L}{T}$	(4.98)
\mathbf{v}^i	$i = 1, 2, 3 \dots$		
	asymptotic expansion of Stokes velocity \mathbf{v}	$[\mathbf{v}^i] = \frac{L}{T}$	(2.3)
\mathbf{v}^l	mass-velocity of liquid phase	$[\mathbf{v}^l] = \frac{L}{T}$	(4.2)
\mathbf{v}^s	mass-velocity of solid phase	$[\mathbf{v}^s] = \frac{L}{T}$	(4.2)
\mathbf{v}^α	mass-averaged velocity of phase α	$[\mathbf{v}^\alpha] = \frac{L}{T}$	(4.18)
$\widetilde{\mathbf{v}}^0$	$= \mathbf{q}$, Darcy's velocity	$[\widetilde{\mathbf{v}}^0] = \frac{L}{T}$	(2.33)
$\widetilde{\mathbf{v}}^1$	average of \mathbf{v}^1 over domain Ω	$[\widetilde{\mathbf{v}}^1] = \frac{L}{T}$	(2.33)
v_a	average velocity of fluid in a cell	$[v_a] = \frac{L}{T}$	(3.6)
v_s	superficial velocity of fluid in a cell	$[v_s] = \frac{L}{T}$	(3.4)
\mathbf{v}_s	a velocity which $\mathbf{v}_s _{\partial\Omega} = \mathbf{s}$		(4.114)
\mathbf{v}_0	$\nabla \cdot \mathbf{v}_0 = f - \nabla \cdot \mathbf{v}_s$		(4.160)

variables	definitions	units	equations
$\hat{\mathbf{v}}$	$\hat{\mathbf{v}} = \mathbf{v}_s + \mathbf{v}_0$		(4.161)
\mathbf{v}_D	superficial-velocity vector or Darcy's velocity	$[\mathbf{v}_s] = \frac{L}{T}$	(4.1)
\mathbf{v}_{\max}	largest velocity	$[\mathbf{v}_{\max}] = \frac{L}{T}$	(6.7)
V	a Sobolev subspace of $H^1(\Omega)$		(4.93)
V^\perp	orthogonal of V in $H_0^1(\Omega)$		(4.94)
V^0	polar set of V		(4.95)
V_h	finite-dimensional subspace of $H^1(\Omega)$		(5.26)
\mathbf{V}_i	vector of $v_i^m, m = 1, 2, \dots, M$		(5.28)
V_s	volume of cylinders in a cell	$[V_s] = L^3$	(3.54)
V_t	total volume of a cell	$[V_t] = L^3$	(3.46)
$\mathbf{w}_{\alpha\beta}$	velocity of interface $\alpha\beta$	$[\mathbf{w}_{\alpha\beta}] = \frac{L}{T}$	(4.11)
\mathbf{x}	$= (x_1, x_2, x_3)$, macroscopic variable	$[\mathbf{x}] = L$	Figure 2.2
\mathbf{y}	$= (y_1, y_2, y_3)$, microscopic variable	$[\mathbf{y}] = L$	Figure 2.2
\mathbf{y}^*	dimensionless variable \mathbf{y}	$[\mathbf{y}^*] = 1$	(2.40)-(2.42)
z	z-axis in Cartesian coordinate	$[z] = L$	(2.38)
α	a nonzero parameter	$[\alpha] = 1$	Figure 2.3
α_m	material dependent parameter	$[\alpha_m] = 1$	(5.6)
β	a nonzero parameter	$[\beta] = 1$	Figure 2.3
δ_{ij}	identity matrix	$[\delta_{ij}] = 1$	(3.2)
δt	time step	$[\delta t] = T$	(6.7)
δ_{\max}	maximum time step	$[\delta_{\max}] = T$	(6.7)
$\delta A_{\alpha\beta}$	portion of the interface $\alpha\beta$ within δV	$[\delta A_{\alpha\beta}] = L^2$	(4.12)
δk	relative error of k_s with respect to k_{RM}	$[\delta k] = 1$	Table 3.2
δV	representative elementary volume	$[\delta V] = L^3$	(4.22)
δV_α	portion of α -phase	$[\delta V_\alpha] = L^3$	(4.9)

variables	definitions	units	equations
δV_β	portion of β -phase	$[\delta V_\beta] = L^3$	(4.9)
ϵ	$0 < \epsilon \ll 1$, a parameter	$[\epsilon] = 1$	Figure 2.1
ϵ^l	porosity	$[\epsilon^l] = 1$	below (3.6)
ϵ^s	solid volume fraction	$[\epsilon^s] = 1$	(3.7)
γ	the surface tension	$[\gamma] = \frac{M}{T^2}$	(6.8)
Γ	$\Gamma_F \cup \Gamma_S$	$[\Gamma] = L^2$	Figure 1.3
Γ_F	fluid boundary	$[\Gamma_F] = L^2$	Figure 1.3
Γ_S	solid boundary	$[\Gamma_S] = L^2$	Figure 1.3
κ	the curvature	$[\kappa] = \frac{1}{L}$	(6.8)
μ	dynamic viscosity	$[\mu] = \frac{M}{L \cdot T}$	(2.2)
Ω	periciliary layer (PCL)	$[\Omega] = L^2$	Figure 1.2
Ω_1	domain between the tip of cilia and mucus	$[\Omega_1] = L^2$	Figure 1.2
Ω_2	domain containing cilia	$[\Omega_2] = L^2$	Figure 1.2
Ω_e	an element domain		before (3.27)
Ω_F	fluid domain	$[\Omega_F] = L^3$	Figure 1.3
Ω_S	solid domain	$[\Omega_S] = L^3$	Figure 1.3
ϕ_i	quadratic basis functions		(3.27)
Φ	vector of the quadratic basis function		(3.27)
ψ_i	linear basis function		(3.28)
Ψ	vector of the linear basis functions		(3.28)
ρ	density of fluid	$[\rho] = \frac{M}{L^3}$	(2.38)
ρ^α	mass-averaged density of α phase	$[\rho^\alpha] = \frac{M}{L^3}$	(4.17)
τ	the tangent at the curve	$[\tau] = 1$	(6.10)
θ	angle between cilia and horizontal plane	$[\theta] = 1$	Figure 1.2

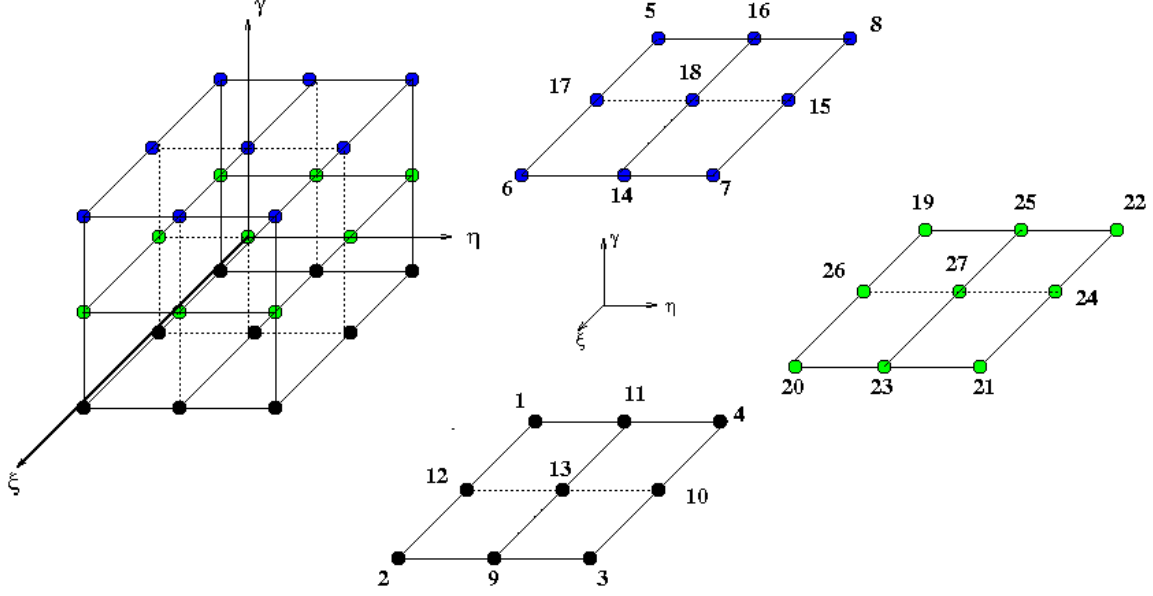


Figure B.1: Nodal numbering for the 27-variable-number-of-nodes element where the origin is at the center of the brick.

APPENDIX B. BASIS FUNCTIONS

Since some basis functions are not provided explicitly in books, in this Appendix, we provide basis functions of two different elements: Brick and tetrahedral elements which are used in this work. The basis functions of the three-dimensional Brick element or triquadratic 27-node, see Figure B.1 where the triquadratic coordinates are ξ, η and γ , can be derived from quadratic one-dimensional element, see Figure B.2. Each shape function has a unit value on one node and zero on the rest. The basis functions of the quadratic element are [52]:

$$N_1(\xi) = \frac{(\xi - \xi_2)(\xi - \xi_3)}{(\xi_1 - \xi_2)(\xi_1 - \xi_3)} = \frac{1}{2}\xi(\xi - 1), \quad (\text{B.1})$$

$$N_2(\xi) = \frac{(\xi - \xi_1)(\xi - \xi_3)}{(\xi_2 - \xi_1)(\xi_2 - \xi_3)} = 1 - \xi^2, \quad (\text{B.2})$$

$$N_3(\xi) = \frac{(\xi - \xi_1)(\xi - \xi_2)}{(\xi_3 - \xi_1)(\xi_3 - \xi_2)} = \frac{1}{2}\xi(\xi + 1). \quad (\text{B.3})$$

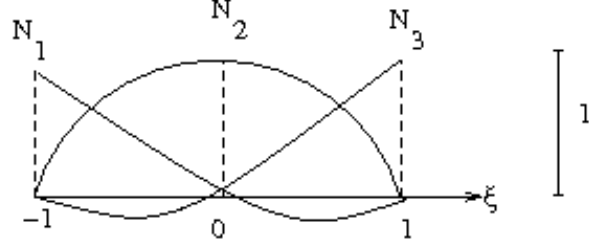


Figure B.2: Nodal numbering for the 3-variable-number-of-nodes element

Since the coordinate of the basis function ψ_1 in Figure B.1 is $(-1, -1, -1)$, the basis functions of the three-dimensional Brick element at that node is

$$\psi_1(\xi, \eta, \gamma) = N_1(\xi)N_1(\eta)N_1(\gamma) = \frac{1}{8}\xi\eta\gamma(\xi - 1)(\eta - 1)(\gamma - 1). \quad (\text{B.4})$$

Similarly, we have

$$\psi_2(\xi, \eta, \gamma) = N_3(\xi)N_1(\eta)N_1(\gamma) = \frac{1}{8}\xi\eta\gamma(\xi + 1)(\eta - 1)(\gamma - 1), \quad (\text{B.5})$$

$$\psi_3(\xi, \eta, \gamma) = N_3(\xi)N_3(\eta)N_1(\gamma) = \frac{1}{8}\xi\eta\gamma(\xi + 1)(\eta + 1)(\gamma - 1), \quad (\text{B.6})$$

$$\psi_4(\xi, \eta, \gamma) = N_1(\xi)N_3(\eta)N_1(\gamma) = \frac{1}{8}\xi\eta\gamma(\xi - 1)(\eta + 1)(\gamma - 1), \quad (\text{B.7})$$

$$\psi_5(\xi, \eta, \gamma) = N_1(\xi)N_1(\eta)N_3(\gamma) = \frac{1}{8}\xi\eta\gamma(\xi - 1)(\eta - 1)(\gamma + 1), \quad (\text{B.8})$$

$$\psi_6(\xi, \eta, \gamma) = N_3(\xi)N_1(\eta)N_3(\gamma) = \frac{1}{8}\xi\eta\gamma(\xi + 1)(\eta - 1)(\gamma + 1), \quad (\text{B.9})$$

$$\psi_7(\xi, \eta, \gamma) = N_3(\xi)N_3(\eta)N_3(\gamma) = \frac{1}{8}\xi\eta\gamma(\xi + 1)(\eta + 1)(\gamma + 1), \quad (\text{B.10})$$

$$\psi_8(\xi, \eta, \gamma) = N_1(\xi)N_3(\eta)N_3(\gamma) = \frac{1}{8}\xi\eta\gamma(\xi - 1)(\eta + 1)(\gamma + 1), \quad (\text{B.11})$$

$$\psi_9(\xi, \eta, \gamma) = N_3(\xi)N_2(\eta)N_1(\gamma) = \frac{1}{4}\xi\gamma(\xi + 1)(1 - \eta^2)(\gamma - 1), \quad (\text{B.12})$$

$$\psi_{10}(\xi, \eta, \gamma) = N_2(\xi)N_3(\eta)N_1(\gamma) = \frac{1}{4}\eta\gamma(1 - \xi^2)(\eta + 1)(\gamma - 1), \quad (\text{B.13})$$

$$\psi_{11}(\xi, \eta, \gamma) = N_1(\xi)N_2(\eta)N_1(\gamma) = \frac{1}{4}\xi\gamma(\xi - 1)(1 - \eta^2)(\gamma - 1), \quad (\text{B.14})$$

$$\psi_{12}(\xi, \eta, \gamma) = N_2(\xi)N_1(\eta)N_1(\gamma) = \frac{1}{4}\eta\gamma(1 - \xi^2)(\eta - 1)(\gamma - 1), \quad (\text{B.15})$$

$$\psi_{13}(\xi, \eta, \gamma) = N_2(\xi)N_2(\eta)N_1(\gamma) = \frac{1}{2}\gamma(1 - \xi^2)(1 - \eta^2)(\gamma - 1), \quad (\text{B.16})$$

$$\psi_{14}(\xi, \eta, \gamma) = N_3(\xi)N_2(\eta)N_3(\gamma) = \frac{1}{4}\xi\gamma(\xi + 1)(1 - \eta^2)(\gamma + 1), \quad (\text{B.17})$$

$$\psi_{15}(\xi, \eta, \gamma) = N_2(\xi)N_3(\eta)N_3(\gamma) = \frac{1}{4}\eta\gamma(1 - \xi^2)(\eta + 1)(\gamma + 1), \quad (\text{B.18})$$

$$\psi_{16}(\xi, \eta, \gamma) = N_1(\xi)N_2(\eta)N_3(\gamma) = \frac{1}{4}\xi\gamma(\xi - 1)(1 - \eta^2)(\gamma + 1), \quad (\text{B.19})$$

$$\psi_{17}(\xi, \eta, \gamma) = N_2(\xi)N_1(\eta)N_3(\gamma) = \frac{1}{4}\eta\gamma(1 - \xi^2)(\eta - 1)(\gamma + 1), \quad (\text{B.20})$$

$$\psi_{18}(\xi, \eta, \gamma) = N_2(\xi)N_2(\eta)N_3(\gamma) = \frac{1}{2}\gamma(1 - \xi^2)(1 - \eta^2)(\gamma + 1), \quad (\text{B.21})$$

$$\psi_{19}(\xi, \eta, \gamma) = N_1(\xi)N_1(\eta)N_2(\gamma) = \frac{1}{4}\xi\eta(\xi - 1)(\eta - 1)(1 - \gamma^2), \quad (\text{B.22})$$

$$\psi_{20}(\xi, \eta, \gamma) = N_3(\xi)N_1(\eta)N_2(\gamma) = \frac{1}{4}\xi\eta(\xi + 1)(\eta - 1)(1 - \gamma^2), \quad (\text{B.23})$$

$$\psi_{21}(\xi, \eta, \gamma) = N_3(\xi)N_3(\eta)N_2(\gamma) = \frac{1}{4}\xi\eta(\xi + 1)(\eta + 1)(1 - \gamma^2), \quad (\text{B.24})$$

$$\psi_{22}(\xi, \eta, \gamma) = N_1(\xi)N_3(\eta)N_2(\gamma) = \frac{1}{4}\xi\eta(\xi - 1)(\eta + 1)(1 - \gamma^2), \quad (\text{B.25})$$

$$\psi_{23}(\xi, \eta, \gamma) = N_3(\xi)N_2(\eta)N_2(\gamma) = \frac{1}{2}\xi(\xi + 1)(1 - \eta^2)(1 - \gamma^2), \quad (\text{B.26})$$

$$\psi_{24}(\xi, \eta, \gamma) = N_2(\xi)N_3(\eta)N_2(\gamma) = \frac{1}{2}\eta(1 - \xi^2)(\eta + 1)(1 - \gamma^2), \quad (\text{B.27})$$

$$\psi_{25}(\xi, \eta, \gamma) = N_1(\xi)N_2(\eta)N_2(\gamma) = \frac{1}{2}\xi(\xi - 1)(1 - \eta^2)(1 - \gamma^2), \quad (\text{B.28})$$

$$\psi_{26}(\xi, \eta, \gamma) = N_2(\xi)N_1(\eta)N_2(\gamma) = \frac{1}{2}\eta(1 - \xi^2)(\eta - 1)(1 - \gamma^2), \quad (\text{B.29})$$

$$\psi_{27}(\xi, \eta, \gamma) = N_2(\xi)N_2(\eta)N_2(\gamma) = (1 - \xi^2)(1 - \eta^2)(1 - \gamma^2). \quad (\text{B.30})$$

Next we also provide the basis functions of 4-node tetrahedron and 10-node quadratic tetrahedron. For the linear tetrahedron element, the basis functions are

$$N_1(r, s, t) = r, \quad (\text{B.31})$$

$$N_2(r, s, t) = s, \quad (\text{B.32})$$

$$N_3(r, s, t) = t, \quad (\text{B.33})$$

$$N_4(r, s, t) = 1 - r - s - t. \quad (\text{B.34})$$

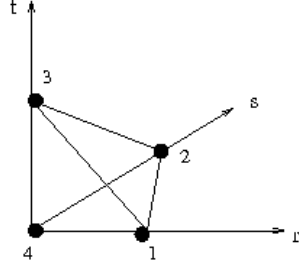


Figure B.3: Nodal numbering for the 4-variable-number-of-nodes tetrahedron element.

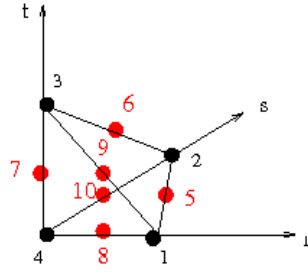


Figure B.4: Nodal numbering for the 10-variable-number-of-nodes quadratic tetrahedron element.

For the quadratic tetrahedron element, the basis functions are

$$N_1(r, s, t) = 2r^2 - r, \quad (\text{B.35})$$

$$N_2(r, s, t) = 2s^2 - s, \quad (\text{B.36})$$

$$N_3(r, s, t) = 2t^2 - t, \quad (\text{B.37})$$

$$N_4(r, s, t) = 2(1 - r - s - t)^2 - (1 - r - s - t), \quad (\text{B.38})$$

$$N_5(r, s, t) = 4rs, \quad (\text{B.39})$$

$$N_6(r, s, t) = 4st, \quad (\text{B.40})$$

$$N_7(r, s, t) = 4(t - rt - st - t^2), \quad (\text{B.41})$$

$$N_8(r, s, t) = 4(r - r^2 - rs - rt), \quad (\text{B.42})$$

$$N_9(r, s, t) = 4rt, \quad (\text{B.43})$$

$$N_{10}(r, s, t) = 4(s - rs - s^2 - st). \quad (\text{B.44})$$

REFERENCES

- [1] J. E. Aarnes, V. Kippe, K. Lie, and A. B. Rustad. Modelling of multiscale structures in flow simulations for petroleum reservoirs. In G. Hasle, K. Lie, and E. Quak, editors, *Geometric Modelling, Numerical Simulation, and Optimization*, pages 307–360. Springer, 2007.
- [2] F. J. Alcocer and P. Singh. Permeability of Periodic Arrays of Cylinders for Viscoelastic Flows. *Physics of Fluids*, 14(7):2578–2581, 2002.
- [3] T. Arbogast and D. S. Brunson. A Computational Method for Approximating a Darcy-Stokes System Governing a Vuggy Porous Medium. *Computational Geosciences*, 11(3):207–218, 2007.
- [4] C. Bahriawati. Three Matlab Implementations of The Lowest-Order Raviart-Thomas MFEM with a Posteriori Error Control. *Computational Methods in Applied Mathematics*, 5(4):333–361, 2005.
- [5] C. Barton and S. Raynor. Analytical Investigation of Cilia Induced Mucus Flow. *Bulletin of Mathematical Biophysics*, 29:419–428, 1967.
- [6] J. Bear. *Dynamics of Fluids in Porous Media*. Dover, 1972.
- [7] J. Bear and A. H. D. Cheng. *Modeling Groundwater Flow and Contaminant Transport*. Springer, 2010.
- [8] G. S. Beavers and D. D. Joseph. Boundary Conditions at a Naturally Permeable Wall. *The Journal of Fluid Mechanics*, 30:197–207, 1967.
- [9] L. S. Bennethum. Flow and deformation: Understanding the assumptions and thermodynamics, updated. Preprint submitted to Elsevier Science, 2006.
- [10] L. S. Bennethum. Multiscale, Hybrid Mixture Theory for Swelling Systems with Interfaces. Note, August 2007.
- [11] L. S. Bennethum. Notes for Introduction to Continuum Mechanics. Continuum Mechanics Class Lecture, February 2011.
- [12] L. S. Bennethum and J. H. Cushman. Multiphase, Hybrid Mixture Theory for Swelling Systems—I: Balance Laws. *International Journal of Engineering Science*, 34(2):125–145, 1996.
- [13] A. Bensoussan, J. L. Lions, and G. Papanicolaou. *Asymptotic Analysis for Periodic Structures*. North-Holland Publishing Company, 1978.

- [14] O. P. Bergelin, G. A. Brown, H. L. Hull, and F. W. Sullivan. Heat Transfer and Fluid Friction During Viscous Flow Across Banks of Tubes–III: A Study of Tube Spacing and Tube size. *Transactions of the ASME Journal*, pages 881–888, August 1950.
- [15] J. G. Berryman and S. C. Blair. Kozeny–Carman Relations and Image Processing Methods for Estimating Darcy’s Constant. *Journal of Applied Physics*, 62:2221–2228, 1987.
- [16] J. Blake. A Model for the Micro-Structure in Ciliated Organisms. *Journal of Fluid Mechanics*, 55:1–23, 1972.
- [17] J. Blake. Mucus Flows. *Mathematical Biosciences*, 17:301–313, 1973.
- [18] J. Blake. Hydrodynamic Calculations on the Movements of Cilia and Flagella I. Paramecium. *Journal of Theoretical Biology*, 45:183–203, 1974.
- [19] J. Blake. On the Movement of Mucus in the Lung. *Journal of Biomechanics*, 8:179–190, 1975.
- [20] J. R. Blake. An Active Porous Medium Model for Ciliary Propulsion. *Journal of Theoretical Biology*, 64:697–701, 1977.
- [21] D. Braess. *Finite Elements Theory, Fast Solvers, and Applications in Solid Mechanics*. Cambridge, 2005.
- [22] D. Braess. *Finite Elements Theory, Fast Solvers, and Applications in Elasticity Theory*. Cambridge University Press, 2007.
- [23] S. C. Brenner and L. R. Scott. *The Mathematical Theory of Finite Element Methods*. Springer-Verlag, 1994.
- [24] F. Brezzi and M. Fortin. *Mixed and Hybrid Finite Element Methods*. Springer-Verlag, 1991.
- [25] H. C. Brinkman. A Calculation of the Viscous Force Exerted by a Flowing Fluid on a Dense Swarm of Particles. *Applied Scientific Research*, A1:27–34, 1947a.
- [26] J. C. Jr. Brown. Determination of the Exposed Specific Surface of Pulp Fibers from Air Permeability Measurements. *TAPPI*, 33:130–137, 1950.
- [27] F. L. Buchholz. Model of Liquid Permeability in Swollen Composites of Superabsorbent Polymer and Fiber. *Journal of Applied Polymer Science*, 102:4075–4084, 2006.
- [28] P. C. Carman. Fluid Flow through Granular Beds. *Transactions of the Institution of Chemical Engineers*, 15:150–166, 1937.
- [29] P. C. Carman. The Determination of the Specific Surface of Powders, I. *Society of Chemical Industry (Trans. and Communications)*, 57:225–234, 1938.

- [30] M. Chandesris and D. Jamet. Boundary Conditions at a Fluid-Porous Interface: An a Priori Estimation of the Stress Jump Coefficients. *International Journal of Heat and Mass Transfer*, 50:3422–3436, 2007.
- [31] M. Chandesris and D. Jamet. Jump Conditions at a Surface-Excess Quantities at a Fluid/Porous Interface: A Multi-Scale Approachh. *Transport in Porous Media*, 78:419–438, 2009.
- [32] C. Y. Chen. Filtration of Aerosols by Fibrous Media. *Chemical Reviews*, 55:595–623, 1955.
- [33] N. Chen, M. Gunzburger, and X. Wang. Asymptotic Analysis of the Differences between the Stokes-Darcy System with Different Interface Conditions and the Stoke-Brinkman System. *Journal of Mathematical Analysis and Applications*, 368:658–676, 2010.
- [34] D. Cioranescu and P. Donato. *An Introduction to Homogenization*.
- [35] W. D. Comper and O. Zamparo. Hydraulic Conductivity of Polymer Matrices. *Biophysical Chemistry*, 34:127–135, 1989.
- [36] J. H. Cushman, L. S. Bennethum, and B. X. Hu. A Primer on Upscaling Tools for Porous Media. *Advances in Water Resources*, 25:1043–1067, 2002.
- [37] H. Darcy. Les Fontaines Publiques de la Ville de Dijon. *Dalmont Paris*, page 647, 1856.
- [38] L. Dormieux, D. Kondo, and Franz-Josef Ulm. *Microporomechanics*. John Wiley and Sons, Ltd, 2006.
- [39] S. S. Dukhin, R. Zimmermann, Jérôme F. L. Duval, and C. Werner. On the Applicability of the Brinkman Equation in Soft Surface Electrokinetics. *Journal of Colloid and Interface Science*, 350:1–4, 2010.
- [40] E. G. Dyakonov and S McCormick. *Optimization in Solving Elliptic Problems*.
- [41] M. S. Engleman, R. L. Sani, and P. M. Gresho. The Implementation of Normal and/or Tangential Boundary Conditions in Finite Element Codes for Incompressible Fluid Flow. *International Journal for Numerical Methods in Fluids*, 2:225–238, 1982.
- [42] G. H. Frommer and C. R. Steele. Permeability of Fluid Flow through Hair Cell Cilia. *Journal of the Acoustical Society of America*, 65(3):759–764, 1979.
- [43] D. K. Gartling, C. E. Hickox, and R. C. Givler. Simulation of Coupled Viscous and Porous Flow Problems. *International Journal of Computational Fluid Dynamics*, 7:23–48, 1996.
- [44] V Girault and P. Raviart. *Finite Element Methods for Navier-Stokes Equations Theory and Algorithms*.

- [45] S. Gueron and K. Levit-Gurevich. Energetic Considerations of Ciliary Beating and the Advantage of Metachronal Coordination. *Proceedings of the National Academy of Sciences*, 96(22):12240–12245, 1999.
- [46] S. Haber and R. Mauri. Boundary Conditions for Darcy’s Flow through Porous Media. *International Journal of Multiphase Flow*, 9(5):561–574, 1983.
- [47] N. S. Hanspal, A. N. Waghode, V. Nassehi, and R. J. Wakeman. Numerical Analysis of Coupled Stokes/Darcy Flows in Industrial Filtrations. *Transport in Porous Media*, 64(1):73–101, 2006.
- [48] J. Happel. Viscous Flow Relative to Arrays of Cylinders. *AIChE*, 5:174–177, 1959.
- [49] H. Hasimoto. On the Periodic Fundamental Solutions of the Stokes Equations and Their Application to Viscous Flow Past a Cubic Array of Spheres. *Journal of Fluid Mechanics*, 5:317–328, 1959.
- [50] C. W. Hirt and B. D. Nichols. Volume of Fluid (VOF) Method for the Dynamics of Free Boundaries. *Journal of Computational Physics*, 39:201–225, 1981.
- [51] U. Hornung. *Homogenization and Porous Media*. Springer-Verlag New York, Inc., 1997.
- [52] T. J. R. Hughes. *The Finite Element Method: Linear Static and Dynamic Finite Element Analysis*. Prentice-Hall, Inc., 1987.
- [53] A. S. Ibrall. Permeability of Glass Wool and Other Highly Porous Media. *Journal of research of the National Bureau of Standards*, 45:398–406, 1950.
- [54] R. Ingram. Finite Element Approximation of Nonsolenoidal, Viscous Flows around Porous and Solid Obstacles. *The SIAM Journal on Numerical Analysis*, 49(2):491–520, 2011.
- [55] G. W. Jackson and D. F. James. The Permeability of Fibrous Porous Media. *The Canadian Journal of Chemical Engineering*, 64:364–374, 1986.
- [56] D. F. James and A. M. J. Davis. Flow at the Interface of a Model Fibrous Porous Medium. *The Journal of Fluid Mechanics*, 426:47–72, 2001.
- [57] V. A. Kirsh. Stokes Flow in Periodic Systems of Parallel Cylinders with Porous Permeable Shells. *Colloid Journal*, 68(2):173–181, 2006.
- [58] J. Koplik, H. Levine, and A. Zee. Viscosity Renormalization in the Brinkman Equation. *Physics of Fluids*, 26(10):2864–2870, 1983.
- [59] S. Kuwabara. The Forces Experienced by Randomly Distributed Parallel Circular Cylinders or Spheres in a Viscous Flow at Small Reynolds Numbers. *Journal of the Physical Society of Japan*, 14:527–532, 1959.

- [60] Y. W. Kwon and H. Bang. *The Finite Element Method using MATLAB*. CRC Press LLC, 1997.
- [61] H. Lamb. *Hydrodynamics*. Cambridge University Press, London, 6th edition, 1932.
- [62] W. J. Layton, F. Schieweck, and I Yotov. Coupling Fluid Flow with Porous Media Flow. *The SIAM Journal on Numerical Analysis*, 40(6):2195–2218, 2003.
- [63] W. L. Lee, P. G. Jayathilake, Z. Tan, Le D. V., H. P. Lee, and B. C. Khoo. Muco-Ciliary Transport: Effect of Mucus Viscosity, Cilia Beat Frequency and Cilia Density. *Computer & Fluids*, 49:214–221, 2011.
- [64] N. Liron. Fluid Transport by Cilia between Parallel Plates. *The Journal of Fluid Mechanics*, 86:705–726, 1978.
- [65] N. Liron and M. Rozenon. Muco-Ciliary Transport. *Journal of Submicroscopic Cytology*, 15:317–321, 1983.
- [66] N. Martys, D. P. Bentz, and E. J. Garboczi. Computer Simulation Study of the Effective Viscosity in Brinkman’s Equation. *Physics of Fluids*, 6:1434–1439, 1994.
- [67] N. S. Martys. Improved Approximation of the Brinkman Equation using a Lattice Boltzmann Method . *Fluid of Fluids*, 13(6):1807–1810, 2001.
- [68] N. S. Martys and J. G. Hagedorn. Multiscale Modeling of Fluid Transport in Heterogeneous Materials using Discrete Boltzmann Methods. *Materials and Structures*, 35:650–659, 2002.
- [69] H. Matsui, S. H. Randell, S. W. Peretti, C. W. Davis, and R. C. Boucher. Coordinated Clearance of Periciliary Liquid and Mucus from Airway Surfaces. *The Journal of Clinical Investigation*, 102:1125–1131, 1998.
- [70] C. E. Miller. Flow Induced by Mechanical Analogues of Mucociliary Systems. *Annals of the New York Academy of Sciences*, 130:880–890, 1996.
- [71] W. A. Miller, J. W. Ross, and G. C. Weatherly. Dynamic Computer Simulation of Viscous Flow Sintering Kinetics. *Journal of Applied Physics*, 52:3884–3888, 1981.
- [72] R. Mittal and G. Iaccarino. Immersed Boundary Methods. *Annual Review of Fluid Mechanics*, 37:239–261, 2005.
- [73] M Morandotti. Self-propelled micro-swimmers in a brinkman fluid. Submitted to the Journal of Biological Dynamics, 2010.
- [74] M. A. Murad, L. S. Bennethum, and J. H. Cushman. A Multi-Scale Theory of Swelling Porous Media: I. Application to One-Dimensional Consolidation. *Transport in Porous Media*, 19:93–122, 1995.

- [75] G. Neale and W. Nader. Practical Significance of Brinkman's Extension of Darcy's Law: Coupled Parallel Flows within a Channel and a Bounding Porous Medium. *The Canadian Journal of Chemical Engineering*, 52:475–478, August 1974.
- [76] B. D. Nichols, C. W. Hirt, and R. S. Hotchkiss. SOLA-VOF: A Solution Algorithm for Transient Fluid Flow with Multiple Free Boundaries. Los Alamos National Laboratory, August 1980.
- [77] Fluidics and Biocomplexity Group, Department of Engineering, University of Oxford. The Microfluidics of Cilia Motion home page. <http://www.eng.ox.ac.uk/fbg/cilia.html>, 2010.
- [78] C. W. Oseen. *Hydrodynamic*. Akademische Verlag, Leipzig, 1985.
- [79] S. Osher and R. Fedkiw. *Level Set Methods and Dynamic Implicit Surfaces*. Springer-Verlag New York, Inc., 2003.
- [80] J. E. Pask, B. M. Klein, P. A. Sterne, and C. Y. Fong. Finite-Element Methods in Electronic-Structure. *Computer Physics Communications*, 135:1–34, 2001.
- [81] C. S. Peskin. The Immersed Boundary Method . *Acta Numerica*, pages 479–517, 2002.
- [82] R. C. Peterson, P. K. Jimack, and M. A. Kelmanson. The Solution of Two-Dimensional Free-Surface Problems Using Automatic Mesh Generation. *International Journal for Numerical Methods in Fluids*, 31:937–960, 1999.
- [83] A. Rabinovitch and R. Rabinovitch. A Simple Model of Light Transmission through Metachronally Moving Cilia . *Journal of Applied Physics*, 67(2):1108–1112, 1990.
- [84] J. N. Reddy and D.K. Gartling. *The Finite Element Method in Heat Transfer and Fluid Dynamics*. CRC Press, Inc., 1994.
- [85] R. P. A. Rocha and M. E. Cruz. Calculation of the Permeability and Apparent Permeability of Three-Dimensional Porous Media. *Transport in Porous Media*, 2009.
- [86] P. Saavedra and L. R. Scott. Variational Formulation of a Model Free-Boundary Problem. *Mathematics of Computation*, 57(196):451–475, October 1991.
- [87] J. Sadé, N. Eliezer, A. Silberberg, and A. C. Nevo. The Role of Mucus in Transport by Cilia. *American Review of Respiratory Disease*, 102:48–52, 1970.
- [88] P. G. Saffman. On the Boundary Condition at the Surface of a Porous Medium. *Studies in Applied Mathematics*, L(2):93–101, June 1971.
- [89] A. G. Salinger, R. Aris, and J. J. Derby. Finite Element Formulations for Large-Scale, Coupled Flows in Adjacent Porous and Open Fluid Domains. *International Journal for Numerical Methods in Fluids*, 18:1185–1209, 1994.
- [90] E. Sanchez-Palencia and A. Zaoui. *Homogenization Techniques for Composite Media*. Springer-Verlag, 1985.

- [91] A. S. Sangani and A. Acrivos. Slow Flow Past Periodic Arrays of Cylinders with Application to Heat Transfer . *International Journal of Multiphase Flow*, 8(3):193–206, 1982.
- [92] J. Schöberl. Netgen, 2001. Automatic mesh generator.
- [93] M. A. Sleight, Blake J. R., and N. Liron. The Propulsion of Mucus by Cilia. *The American Review of Respiratory Disease*, 137:726–741, 1988.
- [94] D. J. Smith, E. A. Gaffney, and J. R. Blake. A Viscoelastic Traction Layer Model of Muco-Ciliary Transport. *Bulletin of Mathematical Biology*, 69:289–327, 2007.
- [95] D. J. Smith, E. A. Gaffney, and J. R. Blake. Modelling Mucociliary Clearance. *Respiratory Physiology Neurobiology*, 163:178–188, 2008.
- [96] L. Spielman and S. L. Goren. Model for Predicting Pressure Drop and Filtration Efficiency in Fibrous Media. *Environmental Science & Technology*, 2:279–287, 1968.
- [97] N. Sukumar and J. E. Pask. Classical and Enriched Finite Element Formulations for Bloch-Periodic Boundary Conditions. *International Journal for Numerical Methods in Engineering*, 77:1121–1138, 2009.
- [98] R. R. Sullivan. Specific Surface Measurements on Compact Bundles of Parallel Fibers. *Journal of Applied Physics*, 13:725–730, 1942.
- [99] H. Tan and K. M. Pillai. Finite Element Implementation of Stress-Jump and Stress-Continuity Conditions at Porous-Medium, Clear-Fluid Interface. *Computers & Fluids*, 38:1118–1131, 2009.
- [100] R. Temam. *Navier-Stokes Equations Theory and Numerical Analysis*. AMS Chelsea Publishing, 2001.
- [101] D. J. Thornton, K. Rousseau, and M. A. McGuckin. Structure and Function of the Polymeric Mucins in Airways Mucus. *Annual Review of Physiology*, 70:459–486, 2008.
- [102] J. A. Voynow and B. K. Rubin. Mucins, Mucus, and Sputum. *CHEST*, 135(2):505–512, 2009.
- [103] T. F. Weinstein. *Three-Phase Hybrid Mixture Theory for Swelling Drug Delivery Systems*. PhD thesis, University of Colorado Denver, 2005.
- [104] T. F. Weinstein and L. S. Bennethum. On the Derivation of the Transport Equation for Swelling Porous Materials with Finite Deformation. *International Journal of Engineering Science*, 2006.
- [105] J. A. Wheat. The Air Flow Resistance of Glass Fiber Filter Paper. *Canadian Journal of Chemical Engineering*, 41:67–72, 1963.

- [106] S. Whitaker. Momentum Transfer at the Boundary between a Porous Medium and a Homogeneous Fluid—I. Theoretical Development. *International Journal of Heat and Mass Transfer*, 38(14):2635–2646, 1995.
- [107] M. L. White. The Permeability of an Acrylamide Polymer Gel. *The Journal of Physical Chemistry*, 64:1563–1565, 1960.
- [108] E. J. Wiggins, W. B. Campbell, and O. Maass. Determination of the Specific Surface of Fibrous Materials. *The Canadian Journal of Research*, 17 Sec. B:318–324, 1939.
- [109] K. J. Wojciechowski. *Analysis and Numerical Solution of Nonlinear Volterra Partial Integro-differential Equations Modeling Swelling Porous Materials*. PhD thesis, University of Colorado Denver, 2011.
- [110] Z. Zhang and I. Bubuska. A Numerical Method for Steady State Free Boundary Problems. *SIAM Journal on Numerical Analysis*, 33(6):2184–2214, 1996.
- [111] A. A. Zick and G. M. Homsy. Stokes Flow Through Periodic Arrays of Spheres. *Journal of Fluid Mechanics*, 115:13–26, 1982.